Complex Hydrides for Hydrogen Storage:
A First-Principles Study

Ebrahim Hazrati

Complex Hydrides for Hydrogen Storage: A First-Principles Study

Proefschrift

ter verkrijging van de graad van doctor
aan de Radboud Universiteit Nijmegen
op gezag van de rector magnificus prof. mr. S.C.J.J. Kortmann,
volgens besluit van het college van decanen
in het openbaar te verdedigen op
dinsdag 18 juni 2013 om 13:00 uur precies.

door

Ebrahim Hazrati

geboren op 23 augustus 1983
te Gandoman
Iran

Promotor:	Prof. dr. R. A. de Groot
Copromotoren:	Dr. G. A. de Wijs
	Dr. G. Brocks (UT)
Manuscriptcommissie:	Prof. dr. A. P. M. Kentgens (Chairman)
	Prof. dr. Gerrit C. Groenenboom
	Dr. P. E. de Jongh (UU)

Ebrahim Hazrati, Complex Hydrides for Hydrogen Storage: A First-Principles Study
PhD Thesis, Radboud University Nijmegen, The Netherlands
With summary in Dutch
Cover: $(LiBH_4)_{54}$ cluster
ISBN: 978-94-6191-701-0
Printed by Ipskamp Drukkers BV, Enschede

The work presented in this thesis is part of the Sustainable Hydrogen program of "Advanced Catalytic Technologies for Sustainability (ACTS)" and the "Stichting voor Fundamenteel Onderzoek der Materie (FOM)", both financially supported by the "Nederlandse Organisatie voor Wetenschappelijk Onderzoek (NWO)".

Contents

Chapter 1

Introduction

1.1 Energy Resources

We can seperate the energy resources that are available to us into two categories: (a) non-renewable energy resources and (b) renewable energy resources. Fossil fuels (coal, oil and natural gas) are an example of non-renewable sources of energy. Fossil fuels are finite resources. Once fossil fuels are finished, it will take millions of years before they form again. There are clear indications that it takes only a few decades before the current known oil and gas reserves will be exhausted.[1]

Another major disadvantage of using fossil fuels to produce energy is the emission of carbon dioxide (CO_2). Carbon dioxide is a greenhouse gas and is believed to be the biggest contributor to climate change.[2] Burning fossil fuels will increase the concentration of carbon dioxide in the atmosphere. The current concentration of carbon dioxide in the atmosphere is about 36% higher compared to its concentration in pre-industrial time (before 1700).[3] This increase in carbon dioxide concentration is mainly due to burning of oil, coal and gas, and deforestation.

We need energy resources which will not run out and have a much lower environmental impact. Renewable energies come from renewable resources such as:

- Solar

  Solar energy technologies produce electricity from the energy of the sun. Photovoltaic (PV) materials and devices convert sunlight into electrical energy. PV cells are commonly known as solar cells. By far the most common bulk material for solar cells is crystalline silicon.

- Wind

  Wind energy technologies use the energy in wind for practical purposes such as generating electricity (wind turbines), pumping water (wind pumps), and grinding grain (windmills).

- Water[a]

  Innovative technologies generate energy from waves, currents and tides. Currently, hydropower is the largest source of renewable electricity in the United States.

- Biomass

  Biomass is biological material from living, or recently living organisms. There are many types of biomass, such as plants, residue from agriculture and forestry, and the organic component of municipal and industrial wastes, that can now be used to produce fuels, chemicals, and power.

- Geothermal

  Geothermal technologies use the heat from the Earth. Geothermal resources include the heat retained in shallow ground, hot water and rock found a few miles beneath the Earth's surface, and extremely high-temperature molten rock located deep in the Earth. Geothermal energy provides electricity and efficient heating and cooling.

1.2 Why hydrogen?

Hydrogen is an energy carrier[b] that can be produced from diverse resources, both renewable and non-renewable. It can then be used in fuel cells or burned in internal combustion engines. Figure 1.1 shows that big car manufacturers consider fuel cell electric vehicles (FCEVs) complimentary to their other advanced vehicle technologies such as plug-in electric vehicles (PEVs). One of the advantages of fuel cells is that they can be scaled up to support larger vehicles, including heavy-duty platforms like transit buses. Another attractive feature of hydrogen is that it can be used as a storage medium for electricity generated from intermittent, renewable resources such as solar, wind, wave and tidal power. It thereby provides a solution to one of the major issues of sustainable energy, namely the problem of intermittency of supply.[4] Hydrogen does not occur naturally as a gas on earth. It is always combined with other elements. Water, for example, is a combination of hydrogen and oxygen. As long as hydrogen is produced from non-fossil-fuel feed stock, it is a genuinely sustainable or renewable fuel. In order to make hydrogen a viable energy carrier, there are three major technological barriers that must be overcome.[4] First, the cost of efficient and

---

[a] Wind and water have been used as renewable energy resources since ancient times and they are gaining renewed interest.

[b] Hydrogen is an energy carrier, not an energy source, i.e. *it stores and delivers energy in a usable form, and it must be produced from compounds that contain it.*

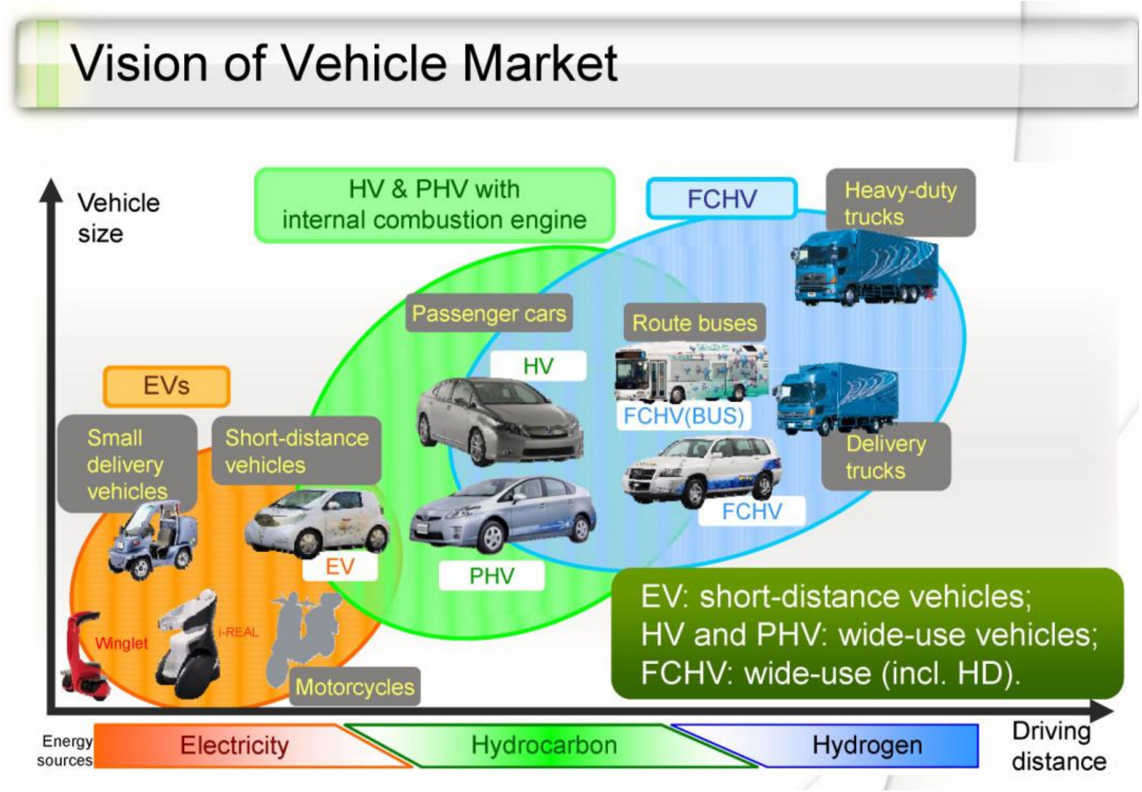

Figure 1.1: GM and Toyota Vehicle Technology Maps [*GM Fuel Cell Technology Status, GM presentation at CEC Workshop for the 2010-2011 Investment Plan on Sept. 29, 2009.*]

sustainable hydrogen production and delivery must be significantly reduced. Second, new generations of hydrogen storage systems for both vehicular and stationary applications must be developed. Finally, the cost of fuel cell and other hydrogen-based systems must be reduced.

1.3 Hydrogen Storage

Storage of hydrogen is one the most technically challenging barriers to the widespread commercialization of hydrogen-fueled light-duty vehicles. Hydrogen storage challenges are:

- Weight and Volume
- Efficiency
- Durability
- Refueling Time
- Cost

A list of requirements that has been set by the US department of energy (DOE) for a storage system for mobile applications are shown in Figure 1.2. Hydrogen can be stored in a variety of ways. In the following the most common ways of storing hydrogen are disscused.[5–7]

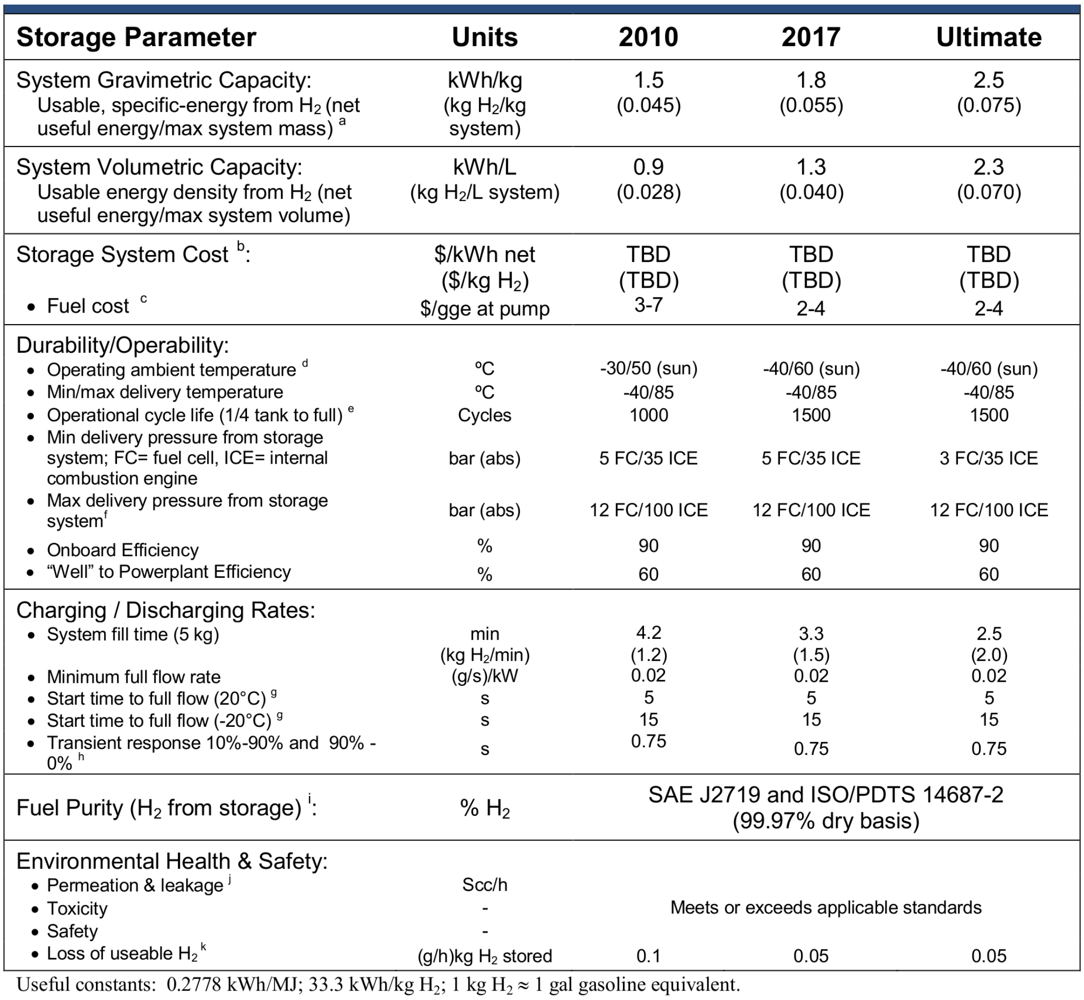

Storage Parameter	Units	2010	2017	Ultimate
System Gravimetric Capacity: Usable, specific-energy from H_2 (net useful energy/max system mass) [a]	kWh/kg (kg H_2/kg system)	1.5 (0.045)	1.8 (0.055)	2.5 (0.075)
System Volumetric Capacity: Usable energy density from H_2 (net useful energy/max system volume)	kWh/L (kg H_2/L system)	0.9 (0.028)	1.3 (0.040)	2.3 (0.070)
Storage System Cost [b]:	\$/kWh net (\$/kg H_2)	TBD (TBD)	TBD (TBD)	TBD (TBD)
• Fuel cost [c]	\$/gge at pump	3-7	2-4	2-4
Durability/Operability:				
• Operating ambient temperature [d]	ºC	-30/50 (sun)	-40/60 (sun)	-40/60 (sun)
• Min/max delivery temperature	ºC	-40/85	-40/85	-40/85
• Operational cycle life (1/4 tank to full) [e]	Cycles	1000	1500	1500
• Min delivery pressure from storage system; FC= fuel cell, ICE= internal combustion engine	bar (abs)	5 FC/35 ICE	5 FC/35 ICE	3 FC/35 ICE
• Max delivery pressure from storage system[f]	bar (abs)	12 FC/100 ICE	12 FC/100 ICE	12 FC/100 ICE
• Onboard Efficiency	%	90	90	90
• “Well” to Powerplant Efficiency	%	60	60	60
Charging / Discharging Rates:				
• System fill time (5 kg)	min (kg H_2/min)	4.2 (1.2)	3.3 (1.5)	2.5 (2.0)
• Minimum full flow rate	(g/s)/kW	0.02	0.02	0.02
• Start time to full flow (20°C) [g]	s	5	5	5
• Start time to full flow (-20°C) [g]	s	15	15	15
• Transient response 10%-90% and 90% - 0% [h]	s	0.75	0.75	0.75
Fuel Purity (H_2 from storage) [i]:	% H_2	SAE J2719 and ISO/PDTS 14687-2 (99.97% dry basis)		
Environmental Health & Safety:				
• Permeation & leakage [j]	Scc/h	Meets or exceeds applicable standards		
• Toxicity	-			
• Safety	-			
• Loss of useable H_2 [k]	(g/h)kg H_2 stored	0.1	0.05	0.05

Useful constants: 0.2778 kWh/MJ; 33.3 kWh/kg H_2; 1 kg H_2 ≈ 1 gal gasoline equivalent.

Figure 1.2: DOE Targets for Onboard Hydrogen Storage Systems for Light-Duty Vehicles (revised in 2009).

1.3.1 Compressed Hydrogen Gas Tanks

Compressed hydrogen gas tanks store H_2 in its gaseous state under pressure. In order to increase the energy density of gaseous hydrogen, it must be stored at very high pressures. Therefore, storage of hydrogen as a gas requires high-pressure tanks (350 to 700 bar). These high pressures require material and design improvements in order to ensure tank integrity. Advances in compression technologies are also required to improve efficiencies and reduce the cost of producing high-pressure hydrogen.

1.3.2 Cryogenic Liquid Hydrogen Tanks

The energy density of hydrogen can be improved by storing hydrogen in a liquid state. The volumetric capacity of liquid hydrogen is 0.070 kg/L, compared to 0.030 kg/L for 700 bar gas tanks. Since the boiling point of hydrogen at one atmosphere pressure is -252.8 °C, storage of hydrogen as a liquid requires cryogenic temperatures. This means the cost of liquefaction, which is high, shoud be added to the other costs such as tank cost. Compressed hydrogen gas tanks and cryogenic liquid hydrogen tanks are impractical due to safety concerns and small volumetric densities.

1.3.3 Materials-Based hydrogen storage

Metal hydrides

Metal hydrides are promising candidates for reversible on-board hydrogen storage and release at low temperatures and pressures. Hydrogen is a highly reactive element and is known to form hydrides with metals and alloys. Therefore, in the presence of hydrogen, the metal matrix is expanded and filled with absorbed hydrogen atoms that are usually located in tetrahedral or octahedral interstitial sites. This provides the possibility of storing hydrogen in a more compact (higher energy density) and safer way compared to compressed hydrogen gas tanks and cryogenic liquid hydrogen tanks. The corresponding de/rehydrogenation reaction is

$$M + \frac{x}{2}\mathrm{H}_2 \leftrightarrow M\mathrm{H}_x \tag{1.1}$$

where M represents the metal. At equilibrium condition, the change in Gibbs free energy is zero, i.e. $\Delta G = \Delta H - T\Delta S = 0$. Assuming equilibrium with hydrogen gas at the pressure of 1 bar and room temperature then gives $\Delta H \sim 39$ kJ/mol. This shows that the reaction enthalpy ΔH of hydride formation is an important quantity and high thermodynamic stability of a hydride hampers its practical application. Other important issues, besides suitable thermodynamic properties, are fast kinetics, large gravimetric and volumetric capacities and reversibility. As an example, the disadvantages of MgH_2 (MgH_2 has a high H_2 capacity of 7.7 wt%) as a hydrogen storage system are (a) high thermodynamic stability which corresponds to unfavorable desorption temperature of 300 °C at 1 bar H_2[8,9] and (b) slow desorption kinetics.[10] Another example is LaNi_5-based alloy which operates at moderate temperature but its hydrogen capacity does not exceed 1.4 wt%.[11,12] So far, no metal hydride system satisfies all the requirements.

Complex metal hydrides

Before 1997, complex hydrides were not considered as candidates for solid hydrogen storage systems for vehicular application. The pioneering work of Bogdanović and Schwickardi changed this situation. They showed that, upon doping with selected titanium compounds, the dehydriding of $NaAlH_4$ could be kinetically enhanced.[13] This breakthrough has led to a worldwide effort to develop doped alanates (group I and II salts of $[AlH_4]^-$) as practical hydrogen storage materials. The efforts quickly expanded to include amides (group I and II salts of $[NH_2]^-$) and borohydrides (group I and II salts of $[NH_4]^-$) systems.

Complex metal hydrides such as lithium amide ($LiNH_2$) and lithium borohydride ($LiBH_4$) have the potential for higher gravimetric hydrogen capacities than simple metal hydrides. In both $LiNH_2$ and $LiBH_4$, hydrogen is covalently bonded to central atoms (N and B) forming complex anions ($[NH_2]^-$ and $[BH_4]^-$) with Li ionized as Li^+.

The pioneering efforts of Chen et al.[14] in 2002 motivated extensive studies on the reversible hydrogen storage properties of lithium amide and lithium hydride mixture. For $LiNH_2$, the reversible reaction

$$\mathrm{LiNH_2 + LiH \leftrightarrow Li_2NH + H_2\,(g)}$$

releases more than 5 wt% of hydrogen from 150 to 350 °C and has a reaction enthalpy of 67 $kJmol^{-1}H_2$.[14–19] On-board applications of the $LiNH_2$ + LiH mixture as a successful solid state reversible hydrogen storage system face problems such as a high operating temperature and slow release kinetics. To solve such problems it is helpful to understand the mechanism of the $LiNH_2$ + LiH reaction, which has to involve mass transport through bulk crystalline materials. The most elementary defects are Li and H point defects. **Chapter 2** presents a first-principles study of the formation energy and diffusivity of such point defects in bulk $LiNH_2$ in order to examine the initial stages of its transformation into Li_2NH. To see whether transition metal compounds influence the hydrogen storage properties of $LiNH_2$ through changing the energetics of defects, the effect of dopants such as Ti, Sc, Ca, and Mg on the formation energy and, consequently, the concentrations of Li and H point defects are examined.

A gravimetric capacity of 18.5 wt% makes $LiBH_4$ one of the most interesting complex hydrides for hydrogen storage.[6,7,20–23] However, $LiBH_4$ is a relatively stable material that decomposes at a high temperature $\gtrsim$ 400 °C. Furthermore, rehydrogenation is only possible at extreme conditions with typical values for temperature and pressure of 600 °C and 350 bar H_2. In addition, de/rehydrogenation kinetics is slow, which is a common problem for the bulk complex hydrides.[6,24–26]

A recently adopted approach that helps to address such problems, is nanoconfinement in porous materials.[27–29] For instance, experimental studies together with theoretical calculations show that nanoconfinement of $NaAlH_4$ in porous carbon improves the H_2 sorption kinetics and somewhat surprisingly, nanoconfinement also alters the decomposition thermodynamics.[30–33] Improving the sorption properties of $LiBH_4$ by nanoconfinement in porous materials has become the focus of much experimental work.[34–45] Faster dehydrogenation kinetics is reported for $LiBH_4$ infiltrated in carbon aerogels, nanoporous carbon, or nanoporous silica, accompanied by a decrease of the dehydrogenation temperature by at least 100 °C. In addition, confinement of $LiBH_4$ in nanoporous carbon leads to a marked improvement of the reversibility of the hydrogen desorption.

These findings can be the result of changed kinetics, as obviously nanoconfinement puts a limit on the particle size, which will reduce the diffusion distance required for mass transport. Alternatively, the thermodynamics of the reactions might be altered. Changes in the thermodynamics of the reactions could be due to changes in the thermodynamics of the nanoclusters, compared to bulk systems, as nanoclusters are less stable than bulk materials. This is the subject of **chapter 3** in this thesis. In addition, the chemical interaction between the reactant/products and the template material can change the thermodynamics of hydrogen sorption reactions. Indeed, recent in situ X-ray Raman spectroscopy of $LiBH_4$ in porous carbon shows that part of the Li intercalates into the porous carbon during dehydrogenation.[46] In **chapter 4** of this thesis the possible changes in the decomposition thermodynamics of $LiBH_4$ nanoclusters caused by the chemical interaction between the reactant/products and the nanoporous template material are described.

1.3.4 Orbital magnetic susceptibility χ

Nuclear Magnetic Resonance (NMR) spectroscopy is a very powerfull technique that can provide detailed information on the topology, dynamics and three-dimensional structure of molecules, liquids, and solid state materials. Structural and dynamic information is obtainable with or without magic angle spinning (MAS) from NMR studies. Understanding of NMR spectra of nano-particle assemblies requires accurate calculation of the orbital magnetic susceptibility χ to account for surface currents. **Chapter 5** of this thesis shows how χ can be obtained from just chemical shift calculations using a repeated slab geometry. The main advantage is numerical robustness compared to a conventional linear response calculation. Moreover χ can be calculated via the orbital magnetization using the converse method for chemical shifts by Thonhauser et al.[47]. The method is illustrated and validated on fcc Ne, $LiBH_4$ and diamond.

1.3.5 Methodology

In this section the methods that have been used in this thesis are briefly addressed.

Density functional theory

First-principles calculations were performed in the framework of density functional theory (DFT)[48,49] using the PBE generalized gradient approximation (GGA)[50] and the projector augmented wave method (PAW)[51,52] as implemented in the Vienna *ab initio* simulation program (VASP).[53,54] A general review on DFT can be found in Ref. 55. Ref. 56 provides a description of the basic theory of the PAW method, as well as most of the details required to make the method work in practice.

Standard DFT fails to describe the non-local van der Waals (vdW) interactions. However, these interactions are important for graphite, where they account for most of the forces that bind the graphene layers together. In order to describe graphite and its Li intercalation compounds (in chapter 4), the recently proposed van der Waals density functional (vdW-DF) of Dion et al.,[57] as implemented in VASP by J. Klimeš et al.[58] using the efficient algorithm of Roman-Perez and Soler[59] is used.

NMR shielding tensor

When we put a sample in a uniform external magnetic field $\mathbf{B}^{\text{ext}}$, an electronic current density $\mathbf{J}^{\text{ind}}(\mathbf{r})$ will be induced. This current produces an induced magnetic field $\mathbf{B}^{\text{ind}}(\mathbf{r})$ resulting in a total magnetic field of $\mathbf{B}^{\text{tot}}(\mathbf{r}) = \mathbf{B}^{\text{ext}} + \mathbf{B}^{\text{ind}}(\mathbf{r})$ at the position ($\mathbf{r}$). The NMR shielding tensor $\overset{\leftrightarrow}{\sigma}$ is defined as

$$\mathbf{B}_i^{\text{ind}} = -\overset{\leftrightarrow}{\sigma}_i \mathbf{B}^{\text{ext}} \tag{1.2}$$

or

$$\sigma_{i,\alpha\beta} = -\frac{\partial B_{i,\alpha}^{\text{ind}}}{\partial B_{\beta}^{\text{ext}}} \quad . \tag{1.3}$$

Here i indicates the position of the nucleus i. So, chemical shielding can be seen as the induced field at a given position due to an uniform external magnetic field.

In a periodic system, $\overset{\leftrightarrow}{\sigma}$ is also periodic and can be written as[60]

$$\overset{\leftrightarrow}{\sigma}(\mathbf{r}) = \sum_{\text{G}} \overset{\leftrightarrow}{\tilde{\sigma}}(\mathbf{G}) e^{i\text{G.r}} \tag{1.4}$$

where $\mathbf{G}$ are the reciprocal lattice vectors. For $\mathbf{G} \neq 0$, $\overset{\leftrightarrow}{\tilde{\sigma}}(\mathbf{G})$ is a bulk property,

$$\overset{\leftrightarrow}{\sigma}(\mathbf{G}) = -4\pi \overset{\leftrightarrow}{\chi}(\mathbf{G}, \mathbf{0}) \tag{1.5}$$

where $\overset{\leftrightarrow}{\chi}(\mathbf{G}, \mathbf{G}')$ is the magnetic susceptibility matrix.[60] However, for $\mathbf{G} = 0$, $\overset{\leftrightarrow}{\sigma}(0)$ is not a bulk property. Its value depends on the shape of the sample, and is determined by macroscopic magnetostatics.

Quantum chemical methods to calculate σ for molecules have a long tradition.[61] Numerical approaches for the calculation of σ and the bulk susceptibility for periodic systems were developed only in the 1990s by Mauri, Louie and co-workers.[60,62–64] These were linear response (LR) methods, that calculate the response for infinite periodic systems as a long wave-length limit. Also, these were all-electron methods, but using pseudo-potential calculations for various light elements were feasible. Later, an alternative approach was developed by Sebastiani and Parrinello,[65] and it was shown that the shielding arising from core electrons can be treated separately.[66] An important breakthrough occurred with the development of the Gauge-Including Projector-Augmented Wave (GIPAW) approach to shielding by Pickard and Mauri.[63,67] This method allows for efficient shielding calculations for nuclei in a large part of the periodic table. It was extended with a treatement of relativistic effects by Yates et al.[68] enabling also shielding calculations for heavy nuclei.

The GIPAW method is an extension of Blóchl's projector-augmented wave (PAW) method.[69] The PAW methods expands the Kohn-Sham states in a plane-wave basis set and then augments this expansion with solutions of the atomic problem (the so-called "partial waves") in the PAW spheres around the atoms. This augmentation allows for a very accurate description of the shape of the states in the vicinity of the the atomic nuclei at low computational cost. This is crucial to obtain accurate shieldings. The partial wave expansion in PAW, unfortunately, destroys the proper transational behaviour of the solid in a magnetic field. This problem is solved by the introduction of field dependent phase shifts of the partial waves (and dual projection functions): this defines the gauge-including (GIPAW) method. The GIPAW method was formulated as an extension of the linear response of Ref. 67. Recently, the LR was also extended to the APW methodology.[70]

Recently, a novel approach to calculate chemical shifts was introduced by Thonhauser et al.,[71] the so-called "converse method". They argued that the chemical shift can also be calculated as the ratio of the induced magnetic moment $\mathbf{m}^{\mathrm{ind}}$ to the external moment $\mathbf{m}_i^{\mathrm{ext}}$ that is placed at nucleous i. The former arises in response to the latter. In formula:

$$\sigma_{i\alpha\beta} = -\frac{m_\beta^{\mathrm{ind}}}{m_{i,\alpha}^{\mathrm{ext}}} = -\Omega \frac{M_\beta^{\mathrm{ind}}}{m_{i,\alpha}^{\mathrm{ext}}} \quad .$$

Here Ω is the super cell volume and $\mathbf{M}^{\mathrm{ind}}$ is the induced magnetization[c]. Another recent breakthrough enables the usage of this method for periodic systems using

---

[c] In a super cell method only applies an infinite array of moments, sufficiently far apart. One moment in each super cell.

finite field calculations, i.e. avoiding LR. Here, one would expect a problem, as the straightforward calculation of the orbital magnetic moment involves integration of vectorproduct of current density and the position vector **r** over the whole solid. The latter vector is, however, ill-defined, in an infinite periodic system. This was solved in the “modern theory of orbital magnetization”,[72] in an approach reminiscent to, but also markedly different from, the so-called “modern theory or Berry phase theory” to polarisation.[73] Starting from an expression in terms of Wannier functions, Ceresoli et al. arrive at:

$$\mathbf{M}^{\mathrm{ind}} = \frac{1}{16c\pi^3}\mathrm{Im}\sum_{n}^{\mathrm{occ}}\int_{\mathrm{BZ}} \langle\partial_{\mathrm{k}} u_{n\mathrm{k}}| \times (H_k + \epsilon_{n\mathrm{k}})\,|\partial_{\mathrm{k}} u_{n\mathrm{k}}\rangle\, d\mathbf{k} \quad .$$

A GIPAW extension of the above was also developed.[74]

The LR GIPAW of Refs. 63 and 67 and the converse GIPAW method of Ref. 74 both provide complete expressions for the cell-periodic part of the shieldings, i.e. the components with $\mathbf{G} \neq 0$ in expression 1.5 above. The $\mathbf{G} = \mathbf{0}$ component is sample shape dependent, as already noted. It can be obtained from the macroscopic susceptiblity of the material for which a good approximate expression is available in GIPAW linear response.

Chapter 2

Intrinsic defects and dopants in $LiNH_2$: A first-principles study

Abstract

The lithium amide ($LiNH_2$) + Lithium hydride (LiH) system is one of the most attractive light-weight materials options for hydrogen storage. Its dehydrogenation involves mass transport in the bulk (amide) crystal through lattice defects. We present a first-principles study of native point defects and dopants in $LiNH_2$ using density functional theory. We find that both Li-related defects (the positive interstitial Li_i^+ and the negative vacancy V_{Li}^-) and H-related defects (H_i^+ and V_H^-) are charged. Li-related defects are most abundant. Having diffusion barriers of 0.3–0.5 eV, they diffuse rapidly at moderate temperatures. V_H^- corresponds to the $[NH]^{2-}$ ion. It is the dominant species available for proton transport with a diffusion barrier of ~ 0.7 eV. The equilibrium concentration of H_i^+, which corresponds to the NH_3 molecule, is negligible in bulk $LiNH_2$. Dopants such as Ti and Sc do not affect the concentration of intrinsic defects, whereas Mg and Ca can alter it by a moderate amount. Ti and Mg are easily incorporated into the $LiNH_2$ lattice, which may affect the crystal morphology on the nano-scale.

E. Hazrati, G. Brocks, B. Buurman, R. A. de Groot and G. A. de Wijs
Phys. Chem. Chem. Phys., 2011, **13**, 6043-6052

2.1 Introduction

The development of hydrogen storage systems is important for realising hydrogen energy systems in the near future. Solid state reversible hydrogen storage systems are of great interest for this purpose.[5] A successful system should have large gravimetric and volumetric storage capacity, suitable thermodynamic properties, and fast hydrogen absorption and desorption kinetics.

Since the seminal paper by Chen *et al.*[14] in 2002, there has been considerable interest in the lithium amide and lithium hydride mixture. The reversible reaction

$$\mathrm{LiNH_2 + LiH \leftrightarrow Li_2NH + H_2\ (g)} \tag{2.1}$$

releases more than 5 wt% of hydrogen from 150 to 350 °C and has a reaction enthalpy of 67 $\mathrm{kJmol^{-1}H_2}$.[14–19] The desorption reaction has been shown to proceed in two steps.[18,75–77] First the amide decomposes to release ammonia (NH_3), which subsequently reacts with the hydride to form hydrogen.

$$\mathrm{2LiNH_2 \rightarrow Li_2NH + NH_3\ (g)} \tag{2.2}$$

and

$$\mathrm{NH_3\ (g)\ + LiH \rightarrow LiNH_2 + H_2\ (g)}\ . \tag{2.3}$$

On-board applications of the $LiNH_2$ + LiH mixture as a successful solid state reversible hydrogen storage system face problems such as a high operating temperature and slow release kinetics. To solve such problems it is helpful to understand the mechanism of the $LiNH_2$ + LiH reaction, which has to involve mass transport through bulk crystalline materials. It is generally believed that the first step (i.e. Eq. 2.2) is the bottleneck.[16,75,76,78,79] One mechanism proposed has ammonia diffusing through a Li_2NH layer.[77] Alternatively, Li^+ and H^+ ions migrate in $LiNH_2$ and Li_2NH, keeping a local charge balance while gradually changing the composition,[80] resulting in ammonia inside the material or at the surface. Li^+ diffusion from LiH to $LiNH_2$ across the interface has also been put forward,[81] although this is hard to reconcile with an ammonia mediated reaction.

The lattices of $LiNH_2$ and Li_2NH are very similar, with the nitrogen atoms forming essentially the same sublattice. Diffusion of species in and out of the materials converts the amide into the imide. Below we will argue that having NH_3 inside the $LiNH_2$ lattice is unfavourable, and its equilibrium concentration is very low. This means that NH_3 is produced at the surface. $LiNH_2$ then changes locally to Li_2NH via a series of intermediate compositions $Li_{1+y}(NH_2)_{1-y}(NH)_y$. These accommodate the Li^+ coming from the amide that has been consumed, and act as a source of NH_3 at the surface. One has a net mass transport of Li^+ into the amide and of H^+ toward the surface. Of course such mass transport can also be realised by vacancies V_{Li}^{-} and V_{H}^{-} diffusing in the opposite directions.

David *et al.*[80] pointed out the close resemblance between the amide and imide lattice and argued that the amide/imide conversion occurs in a non-stoichiometric fashion, i.e., as a gradual change of composition from $LiNH_2$ to Li_2NH. Moreover, for a wide range of compositions the intermediate retains a cubic anti-fluorite structure similar to Li imide. This point of view gets some support from a recent computational study,[82] where it was found that an intermediate compound with composition $Li_{1.5}NH_{1.5}$ is more stable than separation into bulk amide and bulk imide by 0.08 eV.

Conversion of $LiNH_2$ to Li_2NH naturally involves diffusion of Li and H species through the bulk material. In a crystalline material such mass transport can take place only via lattice defects. The most elementary defects are Li and H point defects. Here we present a first-principles study of the formation energy and diffusivity of such point defects in bulk $LiNH_2$ in order to examine the initial stages of its transformation into Li_2NH. In the final stages additional effects on the energetics might play a role, which we do not consider, such as intrinsic disorder in the H positions,[83–89] or in the Li sublattice.[90]

Early transition metal compounds are frequently added in small amounts to a hydrogen storage material such as $LiNH_2$ because of their supposed catalytic action, whereas alkaline earth compounds are often mixed with their alkali counterparts to try and influence the (de)hydrogenation thermodynamics and kinetics.[91–93] To see whether such additives influence the hydrogen storage properties of $LiNH_2$ through changing the energetics of defects, we examine the effect of dopants such as Ti, Sc, Ca, and Mg on the formation energy and, consequently, the concentrations of Li and H point defects. Such dopants have been considered in previous studies,[94–97] but a systematic study of their charge state has, to our knowledge, not been made, and this usually has a large influence on their energetics.

After discussing the computational details in Sec. 2.2, we report our results for Li and H point defects and metal dopants in Secs. 2.3 and 2.4, respectively. The main conclusions are discussed in Sec. 2.5.

2.2 Computational Methods

First-principles calculations are performed in the framework of density functional theory (DFT)[48,49] using the Generalised gradient approximation (GGA) in the version of Perdew, Burke and Ernzerhof[98] and the projector augmented wave method (PAW)[52] as implemented in the Vienna *ab initio* simulation program (VASP).[53,54] A kinetic energy cutoff of 500 eV is used for the plane wave expansion of the Kohn Sham orbitals. For the systems with defect(s), the Brillouin zone (BZ) integrations are performed by using a $2 \times 2 \times 2$ special k-point mesh according to the Monkhorst-Pack scheme.[99] For charged defects, a homogeneous background-charge is assumed in order to prevent divergence of the total energy. The internal atomic positions are relaxed via the conjugate gradient method until the forces on atoms are less than 0.01 eV/Å. For the systems with a dopant, spin polarised calculations are performed.

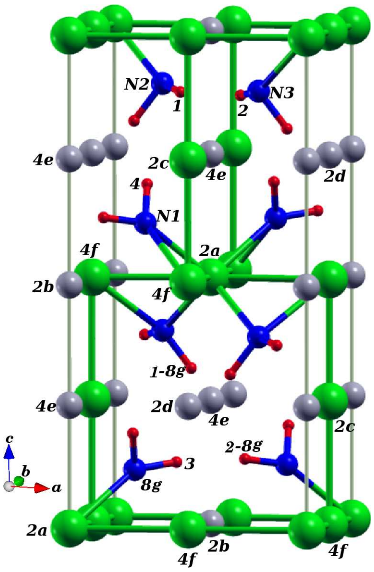

Figure 2.1: The optimised crystal structure of tetragonal $LiNH_2$, with lithium as green spheres, nitrogen as blue spheres, and hydrogen as red spheres. Vacant tetrahedral sites are represented by gray spheres. Relevant sites are labelled by Wyckoff symbols. The unit cell contains eight formula units.

The climbing image nudged elastic band (CI-NEB) method is used to determine the transition state (TS) by constructing a string of images between two adjacent potential energy minima.[100,101] The string of images is relaxed until the forces perpendicular to the minimum energy path are less than 0.03 eV/Å.

$LiNH_2$ has a tetragonal ground state crystal structure belonging to the $I\bar{4}$ space group (No. 82). The optimised lattice constants are a=b=5.013 Å and c=10.342 Å, which are in good agreement with the experimental values (5.034 and 10.255 Å, respectively).[102] The unit cell of $LiNH_2$ contains eight formula units (see Fig. 2.1). The optimised atomic positions are listed in Table 2.1. Li atoms are tetrahedrally coordinated by N atoms and N atoms have a distorted fcc arrangement. All NH_2 moieties are equivalent, but the two hydrogens within one moiety are inequivalent. The N-H bonds point towards the midpoints between two adjacent vacant tetrahedral sites. In all our subsequent calculations we use computationally optimised structures.

The calculations of native point defects and dopants are performed in a $(2\times2\times1)$ supercell containing 128 atoms. The supercell volume and shape are fixed, but the

Table 2.1: Optimised atomic coordinates for $LiNH_2$

atom	Wyckoff position	coordinates
Li(1)	2a	0, 0, 0
Li(2)	4f	0, 0.5, 0.0069
Li(3)	2c	0, 0.5, 0.25
N	8g	0.2294, 0.2465, 0.1154
H(1)	8g	0.2285, 0.1154, 0.1918
H(2)	8g	0.4129, 0.3359, 0.1238

internal atomic positions are fully relaxed. Using periodic boundary conditions on a finite size supercell always gives an interaction between the periodic images, which is unwanted as we are interested in isolated defects. We checked the effect of cell size for the hydrogen interstitial H_i^+. With a $(4 \times 4 \times 2)$ supercell we obtain a 0.07 eV higher formation energy than with the $(2 \times 2 \times 1)$ cell (as calculated with Eq. 2.5 below). This places a tolerable error bar on the formation energies given below.

The energy of an isolated H_2 molecule is calculated in a cubic box of size 10 Å. Phonon frequencies (at Γ only) are calculated using a finite difference method.[103] Typical size of the displacement is 0.01 Å where two opposite displacements per independent degree-of-freedom are applied.

2.3 Native point defects in $LiNH_2$

2.3.1 Formalism

At equilibrium the temperature dependent concentration c of a defect is given by the expression

$$c = N \exp(-E_f/k_B T) \tag{2.4}$$

Here N is the number of sites in the lattice (per unit volume) at which the defect can be incorporated. E_f is the defect formation energy, k_B is Boltzmann's constant, and T is the temperature. The formation energy E_f of a defect X in charge state q is defined as[104]

$$E_f[X^q] = E_{\mathrm{tot}}[X^q] - E_{\mathrm{tot}}[\mathrm{bulk}] - \sum_i n_i \mu_i + q[E_F + E_V + \Delta V] \quad .$$

$E_{\mathrm{tot}}[X^q]$ is the total energy of a supercell with a defect in charge state q and $E_{\mathrm{tot}}[\mathrm{bulk}]$ is the total energy for the equivalent defect-free supercell. We use DFT total energies with, if X involves hydrogen, zero-point (vibrational) energy (ZPE) corrections to approximate free energies. This is a suitable approximation for solids as the pV contribution is negligible at the standard pressure of 1 bar. Moreover, the temperature dependence of the vibrational contributions to the Gibbs free energy is negligible, so we can use $T = 0$ results.[a] To calculate the formation energy we need the change in zero point energies between the system with and without a defect. In practice, only the changes in the high frequency vibrations give a non-negligible contribution. In the present case it turns out that only the hydrogen stretch modes matter, i.e. the difference between the N-H stretch frequency in the solid state, and the H-H stretch frequency in the H_2 molecule.[b] E_F is the Fermi energy with respect to the valence-band maximum in the bulk (E_V). ΔV is a correction term to align the reference potential in the defect-containing supercell with that in the defect-free supercell. We align the electrostatic potential on a N atom in the supercell far away from the defect with the electrostatic potential on the N atom in the defect-free supercell. n_i is the number of atoms of type i that have been added to ($n_i > 0$) or removed from ($n_i < 0$) the supercell to create the defect.

μ_i are the chemical potentials of the defect species. They depend on the experimental conditions. We fix the chemical potential of hydrogen μ_H by

$$\mu_H = \frac{1}{2} E_{tot}(H_2) + \frac{1}{2} \Delta G_{(T)}(H_2) \quad . \tag{2.5}$$

The temperature-dependent Gibbs free energy change

$$\Delta G_{(T)}(H_2) = [H_{(T)}(H_2) - H_{(0)}(H_2)] - T \times [S_{(T)}(H_2) - S_{(0)}(H_2)]$$

of a H_2 molecule in the gas phase is added to the DFT total energy $E_{tot}(H_2)$, which includes the ZPE, of an isolated H_2 molecule. We assume the system to be in equilibrium with hydrogen gas at a certain pressure and temperature. Therefore we calculate $\Delta G_{(T)}(H_2)$ at a pressure of 1 bar and for the temperature range 400-700 K.[105] As we will see below, changing the temperature within this range does not alter the most important defect formation energies.

To fix the chemical potential of Li, we assume an equilibrium between the amide and imide phases, i.e. between $LiNH_2$ and Li_2NH. The chemical potential of Li μ_{Li}

---

[a] We calculate the temperature dependence of the formation energies of the H_i^+ interstitial and the V_H^- vacancy. For the latter the change in formation energy is largest, and amounts to a reduction to 36 meV at 500 K. This is sufficiently small to be neglected

[b] We calculate the zero-point energy from the phonons for the defect-free bulk systems, the hydrogen molecule and a few of the supercells containing defects. We only consider the ZPE for the H_i^+, H_i^-, and V_H^- point defects, as only those have sufficiently low formation energies to play a role. We also consider the ZPE for the complexes involving hydrogen addition or removal and for the dopants with various numbers of H vacancies.

can then be expressed as

$$\mu_{\mathrm{Li}} = E_{\mathrm{tot}}(\mathrm{Li_2NH}) - E_{\mathrm{tot}}(\mathrm{LiNH_2}) + \mu_{\mathrm{H}}. \tag{2.6}$$

Similarly we obtain for μ_{N}:

$$\mu_{\mathrm{N}} = E_{\mathrm{tot}}[\mathrm{LiNH_2}] - \mu_{\mathrm{Li}} - 2\mu_{\mathrm{H}} \quad . \tag{2.7}$$

Here the total energies $E_{\mathrm{tot}}(\mathrm{Li_2NH})$ and $E_{\mathrm{tot}}(\mathrm{LiNH_2})$ include ZPE corrections. For Li_2NH we use the optimized Pbca structure by Mueller and Ceder.[89]

We can check whether our choice of chemical potentials is reasonable. If we assume an equilibrium according to Eq. (2.1), then the hydrogen chemical potential is given by

$$2\mu_{\mathrm{H}} = E_{\mathrm{tot}}(\mathrm{LiNH_2}) + E_{\mathrm{tot}}(\mathrm{LiH}) - E_{\mathrm{tot}}(\mathrm{Li_2NH}). \tag{2.8}$$

Assuming equilibrium with hydrogen gas at a pressure of 1 bar then gives a temperature of 510 K, see Eq. (2.5). This temperature is well inside the range we considered above, and well inside the range of experimental dehydrogenation temperatures.[14–18]

Assuming equilibrium between Li_2NH, $LiNH_2$ and NH_3 gas according to Eq. (2.2) is less logical, as one expects NH_3 to be captured immediately by LiH, according to Eq. (2.3).

2.3.2 Formation energies of Li and H point defects

We study vacancy (V_X^q) and interstitial (X_{i}^q) point defects for both $X = \mathrm{Li}$ and $X = \mathrm{H}$ in three possible charge states ($q = +1, 0, -1$). $\mathrm{V}_{\mathrm{Li}}^-$ corresponds to removal of a Li^+ from $LiNH_2$ resulting in a remaining NH_2 species with a negative charge $q = -1$, $[\mathrm{NH_2}]^-$. Adding an extra Li^+ ion gives an interstitial $\mathrm{Li}_{\mathrm{i}}^+$. Adding a proton corresponds to an interstitial with $X = \mathrm{H}$ and $q = +1$, i.e. $\mathrm{H}_{\mathrm{i}}^+$. Below we will see that an interstitial proton recombines with an $[\mathrm{NH_2}]^-$ group to form a neutral NH_3 molecule at a nitrogen site in the lattice. Therefore, in practice $\mathrm{H}_{\mathrm{i}}^+$ stands for NH_3 in the lattice. Likewise, $\mathrm{V}_{\mathrm{H}}^-$, which corresponds to the removal of a proton, leaves an NH^{2-} ion in the lattice, which means it stands for the transformation of an amide into an imide group. By adding or subtracting electrons one can change the charge state of the various impurities. For instance, adding an electron to $\mathrm{H}_{\mathrm{i}}^+$ results in the neutral system, $\mathrm{H}_{\mathrm{i}}^0$, whereas adding 2 electrons gives the negatively charged $\mathrm{H}_{\mathrm{i}}^-$.

The formation energy of each defect for the most stable configuration is presented in Fig. 2.2 as a function of the position of the Fermi level in the band gap. To our knowledge, no experimental value for the band gap has been reported. Here we use the DFT-GGA band gap. The calculated band gap of $LiNH_2$ is 3.4 eV, which is in good agreement with the reported results of Miwa *et al.*[106] (3.2 eV) and of Yang *et al.*[102] (3.48 eV).

Fig. 2.2 shows that the defects with lowest formation energy are Li_i^+ and V_{Li}^- (for Li) and H_i^+ and V_H^- (for H). The H interstitial is a negative U system; the neutral charge state (H_i^0) is never stable as the formation energies of the positively and negatively charged interstitial cross below that of the neutral state. All other neutral defect species (Li_i^0, V_{Li}^0, and V_H^0) have such high formation energies that one of the charged species is always the most stable in practically the whole band gap region.

Fig. 2.2 also shows that Li-related defects have lower formation energies than H-related defects over the entire Fermi energy range. Thus, based on Eq. 2.4, Li-related defects have much higher concentrations than H-related defects. Therefore, in the absence of extrinsic impurities and dopants, charge neutrality is achieved by incorporation of Li related defects with opposite charges (Li_i^+ and V_{Li}^-) in equal amounts. This pins the Fermi level at 2.55 eV [vertical line in Fig. 2.2], where the formation energies of Li_i^+ and V_{Li}^- are equal: E_f = 0.57 eV. The formation energies of H_i^+, V_H^-, and H_i^- are then 1.41, 0.70, and 1.26 eV, respectively.

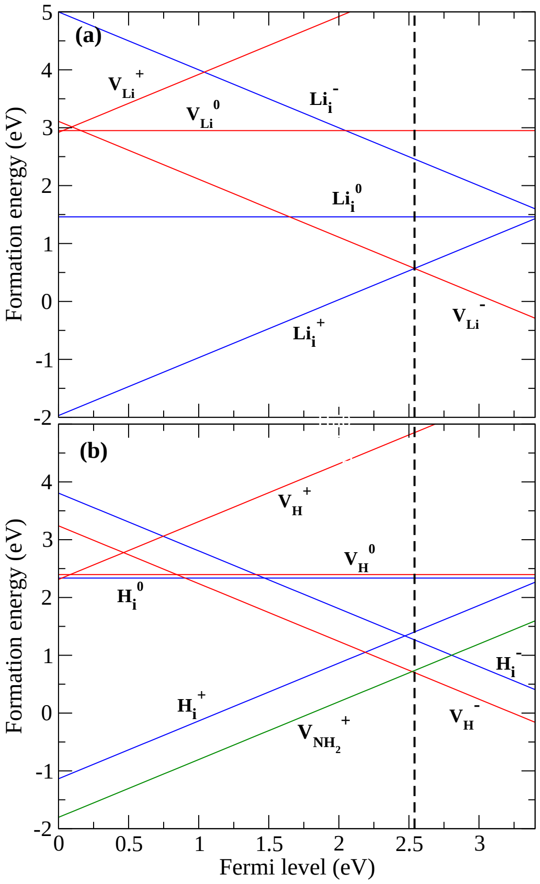

Figure 2.2: Calculated formation energies of Li (a) and H (b) point defects in bulk $LiNH_2$ as a function of the Fermi level. The vertical line gives the Fermi level position resulting from charge neutrality at $T = 400$ K. Also shown in (b) is the formation energy of the $V_{NH_2}^+$.

Table 2.2: Calculated formation energies E_f and migration energy barriers E_m for Li and H related defects. The site labels correspond to those in Fig. 2.1. The activation energies for self-diffusion are given by $E_a = E_f + E_m$. The jump of the Li vacancy is from 2c to the nearest 4f position.

Defect	E_f(eV)	E_m(eV)	
Li_i^+	0.57	0.27 ($2d \leftrightarrow 4e$)	0.46 ($4e \rightarrow 2b$)
V_Li^-	0.57	0.21 ($4f \leftrightarrow 2c$)	0.40 ($4f \rightarrow 2a$)
H_i^+	1.41	0.45 & 0.64 (N1 $\leftrightarrow$ N2)	0.68 (N2 $\leftrightarrow$ N3)
V_H^-	0.70	0.63 ($2 \leftrightarrow 1$)	0.71 ($3 \leftrightarrow 1$)

As the properties of the solid phases are not very temperature dependent, the potential influence of temperature on the formation energies, Eq. (2.5), would mainly originate from the hydrogen gas, cf. Eq. (2.5). Increasing the temperature shifts all the H-related curves in Fig. 2.2 to the left by an identical amount. The chemical potential of Li is however directly linked to that of H via Eq. (2.6). This means that all Li-related curves are also shifted by the same amount if we increase the temperature. In other words, only the Fermi level changes its position with temperature, but the defect formation energies are temperature independent. For example, increasing the temperature from 400 K to 700 K shifts the Fermi level to the left by 0.23 eV.

2.3.3 Structure of point defects and their diffusion barriers

Here we address the mobility of the native point defects in bulk $LiNH_2$. We describe the structural relaxations, list the sites where they can reside, and report the barriers for them to hop to neighbouring sites, as calculated with the CI-NEB. The main results are summarised in Table 2.2.

Li_i^+: Li_i^+ resides in the vacant tetrahedral ($4e$, $2d$, and $2b$ in Fig. 2.1) or octahedral (vacant 8g equivalent to nitrogen 8g in Fig. 2.1) sites. Li_i^+ at a $4e$ and $2d$ site has the same energy. Also, the $2b$ and 8g sites are nearly degenerate. However, the latter are higher in energy by 0.14 eV. Li_i^+ at a tetrahedral vacant site changes the direction of the four N-H bonds which point towards the midpoints between the Li_i^+ and adjacent tetrahedral vacant sites. The four H atoms nearest to Li_i^+ relax by as much as 0.76 Å.

For Li_i^+ the lowest migration energy barrier (0.27 eV) occurs for the path $2d \leftrightarrow 4e$ (in the [100] or [010] direction) in Fig. 2.1. During this interstitial displacement, Li_i^+ moves from a $2d$ ($4e$) site to a $4e$ ($2d$) site passing through a nearby vacant octahedral site. The migration energy barrier for the path $4e \rightarrow 2b$ ($2b \rightarrow 4e$) along the [001] direction in Fig. 2.1 is 0.46 (0.32) eV. In short, a Li_i^+ preferentially resides in $4e$ or

2*d* sites, as these are the lowest in energy. In order to diffuse throughout the entire crystal, the highest point it must encounter is the TS in-between 4*e* and 2*b*, so the effective activation energy for diffusion over large distances is 0.46 eV.

V_{Li}^-: As mentioned in Sec. 2.2, in the $LiNH_2$ crystal there are three crystallographically inequivalent Li sites (2*a*, 4*f*, and 2*c* in Fig. 2.1) and, consequently, three possible Li vacancy sites. A V_{Li}^- (removal of Li^+) at (from) a 4*f* site has the same energy as a V_{Li}^- at a 2*c* site, but a V_{Li}^- at a 2*a* site is higher in energy by 0.14 eV. This is due to the fact that the Li(2*a*)-N bond length (2.07 Å) is shorter than the Li(4*f*)-N (2.05 and 2.23 Å) and Li(2*c*)-N (2.21 Å) bond lengths. In comparison with Li_i^+, the atomic relaxations are smaller in the case of V_{Li}^- although the four nearest H atoms relax towards the V_{Li}^- by as much as 0.64 Å. We find migration energy barriers of 0.21 and 0.40 (0.26) eV, respectively, for the paths $4f \leftrightarrow 2c$ in the [001] direction and $4f \rightarrow 2a$ ($2a \rightarrow 4f$) in the [100] or [010] direction (see Fig. 2.1 and Table 2.2).

V_H^-: As shown in Fig. 2.1, in the $LiNH_2$ crystal structure there are two crystallographically inequivalent H sites [H(1-8g) and H(2-8g)]. But, after removal of H(1), i.e. H(1-8g), H(2) relaxes to the position of H(1) to increase its distance from the nearest H(2) (for hydrogens that are associated with different N atoms, *d*[H(1)-H(2)]= 2.17 Å is longer than *d*[H(2)-H(2)]=1.86 Å). Upon removal of positively charged hydrogen from the NH_2 group (creating V_H^- in the system), the four Li atoms nearest to the N relax inward by as much as 0.20 Å. The migration energy barriers are 0.63 ($1 \leftrightarrow 2$), 0.71 ($1 \leftrightarrow 3$) and 0.91 eV ($4 \rightarrow 1$ of the proton).

H_i^+: A proton interstitial (H_i^+) in the $LiNH_2$ lattice combines with a $[NH_2]^-$ unit to form a NH_3. The nearest Li atoms are 2.21 and 2.32 Å (0.17 and 0.30 Å change in positions) far away from the N atom (in a defect-free supercell each N atom has four neighbouring Li atoms at distances of 2.05, 2.07, 2.21 and 2.23 Å). In this case, two other Li atoms move away from the N atom in NH_3 by 0.65 and 0.71 Å and end up at distances of 2.88 and 3.10 Å. For H_i^+, the energy barriers are 0.45, 0.64 and 0.68 eV, for jumps N1 ↔ N2 (twice) and N2 ↔ N3 in Fig. 2.1, respectively. The barrier 0.45 eV is for a jump from N2 to the N1 site that is in the neighbouring unit cell in the [010] direction. Other jump paths from N2 into N3 are also possible, probably involving some hindrance of Li^+ ion(s) that the proton would have to pass.

Figure 2.3 shows the path that the interstitial proton could take to move from one N2 unit to the N2 in a neighbouring cell. Starting in local minimum (a), the "excess" proton moves via the transition state (b) of 0.45 eV into the local minimum at (c). Starting from (c) another proton leaves, *via* the transition state (d) of 0.64 eV and ends up in local minimum (e). This process is an exchange-like process: The H_i^+ moves (approximately) into a site where another proton is already sitting. This other proton has to be moved aside, which results in a rearrangement of all protons on the NH_2^- unit, compare (c) and (d). Effectively in the whole process an NH_3 has been exchanged with a NH_2^- over a lattice vector **b**. So this path, of which the highest barrier is 0.64 eV, allows a proton to be displaced over arbitrarily large distances throughout the material.

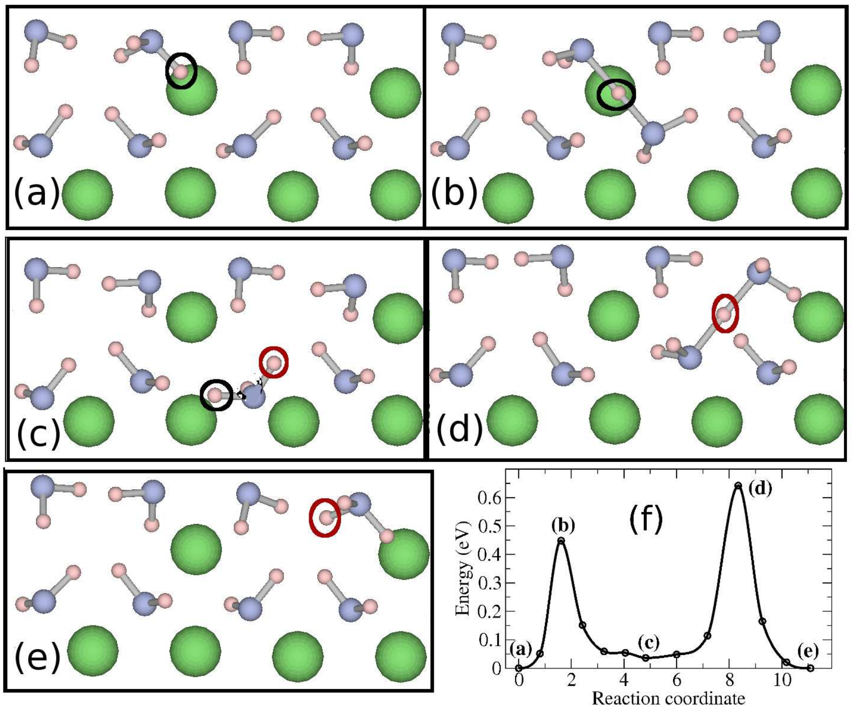

Figure 2.3: Possible migration path for proton interstitials in $LiNH_2$. Lithium, nitrogen and hydrogen atoms are shown in green, blue and pink respectively. First a proton jumps (black circle) *via* the transition state (b) from local minimum (a) to (c). Then another proton (red circle) jumps from (c) to (e) *via* the transition state (d). Only the NH_2^- units in a single (100) plane are shown. The energy along the reaction path is shown in (f).

Table 2.2 summarises our results for the Li and H related defects. The defect formation energies E_f can be used to calculate the intrinsic concentration of Li and H related defects via Eq. (2.4). Fig. 2.4 shows those concentrations for the temperature range 373-773 K. The concentrations of Li_i^+ and V_{Li}^- have to be equal because of charge neutrality. They range from 1.5×10^{15} cm^{-3} at 400 K to 1.8×10^{18} cm^{-3} at 700 K. The hydrogen interstitial H_i^+ has a much higher formation energy. Its concentration is therefore negligible. Even at 700 K it is a factor of $\sim 10^5$ lower than that of the Li impurities. The formation energy of the hydrogen vacancy V_H^- is just a little higher than that of the Li defects and at 700 K its concentration is not even an order of magnitude less.

The absolute concentration of intrinsic defects at all temperatures is quite low. Although once created the mobility of defects is quite high due to the low migration barriers E_m, the activation energies for self-diffusion, given by $E_a = E_f + E_m$, are quite high. It means that mass transport inside crystalline $LiNH_2$ is quite slow, which is consistent with the sluggish dehydrogenation kinetics observed experimentally.

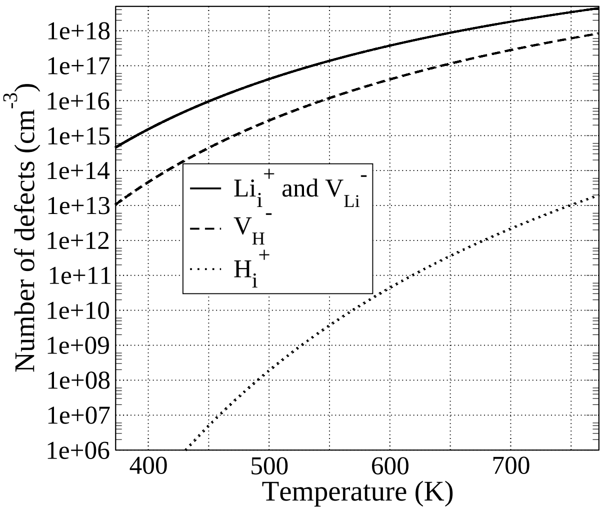

Figure 2.4: Intrinsic defect (Li_i^+, V_{Li}^-, H_i^+, and V_H^-) concentrations in bulk $LiNH_2$ over the temperature range 373-773 K.

2.3.4 Larger defects and defect complexes

In the previous sections point defects were considered that provide the natural link between the amide and imide phases. Here we study a larger defect species, and the most abundant defect complexes.

First we consider removal of an entire NH_2^- group from $LiNH_2$. This is natural, as H and N are covalently bonded. A positive vacancy results: $V_{NH_2}^+$. Upon removal of the NH_2^- group the four nearest neighbour Li atoms relax outward in order to strengthen the bonding with other N atoms. The $V_{NH_2}^+$ formation energy is plotted in Fig. 2.2. It is 0.18 eV higher than the energy of Li_i^+. Therefore, under the chosen equilibrium conditions, it is at least an order of magnitude less abundant than the dominant positive defect species (compare Fig. 2.4). It is also less mobile. The migration energy barrier for diffusion over large distances is 0.92 eV.

Defects interact with one another and can form complexes. Below we study these, for oppositely charged defects that can form pairs. The simplest pairs are Frenkel pairs, where an ion has been moved to an interstitial position, leaving behind a vacancy. In lithium amide such pairs are [V_H^-+H_i^+] and [V_{Li}^-+Li_i^+]. The former has a formation energy of 1.66 eV, which is smaller than the sum (2.11 eV) of the formation energies of the two isolated, i.e. non-interacting defects. These energies are quite high, suggesting these occur in very small numbers. The lithium Frenkel pair has a formation energy of 0.72 eV, where the sum of the formation energies of the isolated defects is 1.14 eV. The complex is not in strong competition with its dissociated constituents, who both have similar formation energies (Table 2.2).

We consider the occurrence of "Schottky-like" pairs, i.e. pairs having two charge-compensating vacancies such as [V_{Li}^{+}+V_{H}^{-}] or [V_{H}^{+}+V_{Li}^{-}], unlikely, as the positive vacancy has a very high formation energy (Fig. 2.2). We checked this with a total energy calculation for the [V_{Li}^{+}+V_{H}^{-}] complex. Instead, here we consider the [V_{H}^{-}+Li_{i}^{+}], [V_{Li}^{-}+H_{i}^{+}], and V_{NH}^{0} complexes. The formation energy of [V_{H}^{-}+Li_{i}^{+}] is 0.54 eV, which is slightly (0.03 eV) lower than the formation energy of Li_{i}^{+} (0.57 eV). Therefore it is likely that these species occur in similar concentrations. One may wonder about the mobility of the complex, as it involves jumps of two species that have to remain in each others neighbourhood (the dissociation cost is 0.73 eV). The formation energy of [V_{Li}^{-}+H_{i}^{+}] is quite high, 1.30 eV.

V_{NH}^{0} is a complex of $V_{NH_2}^{+}$ and H_{i}^{-}, i.e. removal of an entire NH_2^{-} group from the lattice and addition of a H_{i}^{-} at the vacant H position. Therefore, in comparison with $V_{NH_2}^{+}$, the atomic relaxations are smaller in the case of V_{NH}^{0}. The formation energy of this complex is very low, 0.03 (0.49) eV at 400 (700) K. This comes as no big surprise, as one negative ion substitutes for the other, keeping the favourable Madelung contribution to the total energy. The binding energy, i.e. the energy released when $V_{NH_2}^{+}$ and H_{i}^{-} merge into V_{NH}^{0}, is 1.97 eV. So there is a strong effective attraction between $V_{NH_2}^{+}$ and H_{i}^{-}. This does not imply that all H_{i}^{-} are captured by $V_{NH_2}^{+}$. The concentration is in principle still determined by Eqs. 2.4 and 2.5. Because the formation energy of V_{NH}^{0} is so low, however, it is quite likely that such defects are present in the amide in large quantities. V_{NH}^{0} is not mobile on the amide lattice though, we calculated a migration energy barrier for its diffusion of 2.39 eV. So in the first step of the dehydrogenation process (2.1) they are not likely to play a role. In the second step (2.2), where amide is re-grown from LiH and NH_3, it could be built in during the growth process. During this process both LiH and lithium amide are present. A Li-H ion pair might be incorporated into bulk LiH or as a V_{NH}^{0} in bulk amide. In this competition we calculate the former to be more energetically advantageous by 0.19 eV. Hence this species cannot block $Li(NH_2)$ regrowth, but the regrown $Li(NH_2)$ probably contains many frozen-in V_{NH}^{0} defects.

Other complexes that we have considered are V_{LiH}, V_{NH}^{+} ([$V_{NH_2}^{+}$+H_{i}^{0}]), and V_{NH}^{2+} ([$V_{NH_2}^{+}$+H_{i}^{+}]). These have a very high formation energies.

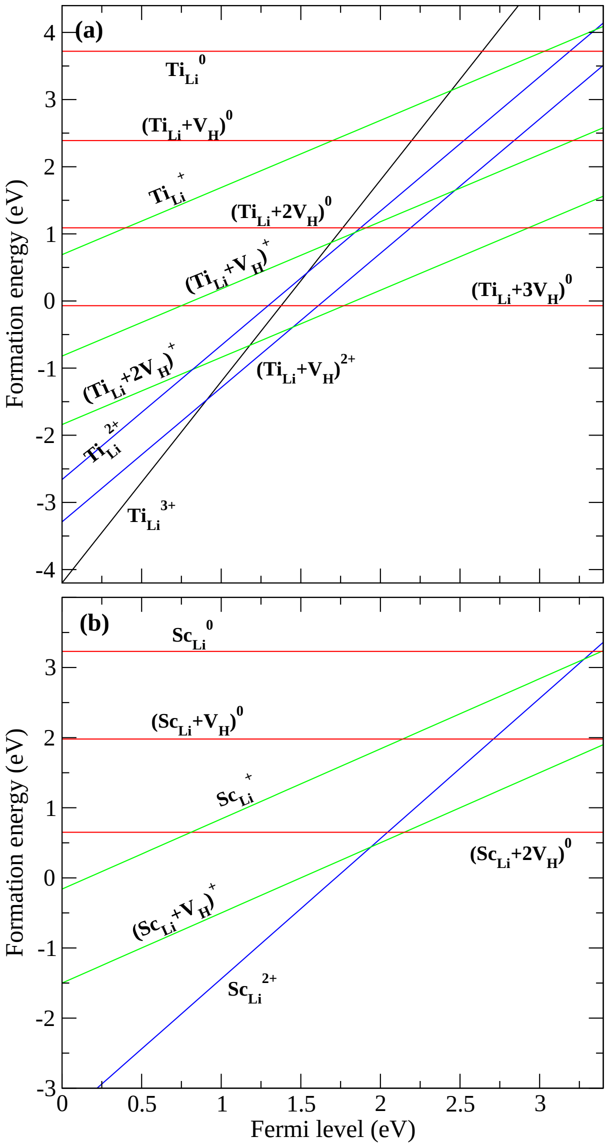

Figure 2.5: Calculated formation energies for (a) Ti and (b) Sc dopants on the Li site in LiNH$_2$.

2.4 The effect of dopants on native defect concentrations in LiNH$_2$

In this section we study the incorporation of dopant atoms such as Mg, Ca, Sc, and Ti into the lithium amide lattice. We study Ti doping because Ti compounds are often used as additives, see, e.g., Matsumoto *et al.*[91] Adding alkaline earth compounds to alkali ones is also an often used approach to try and influence the (de)hydrogenation properties. The formation energies of dopant impurities are calculated using Eq. 2.5. For the chemical potentials μ_{Li} and μ_{H} we adopt the same choice as in the previous

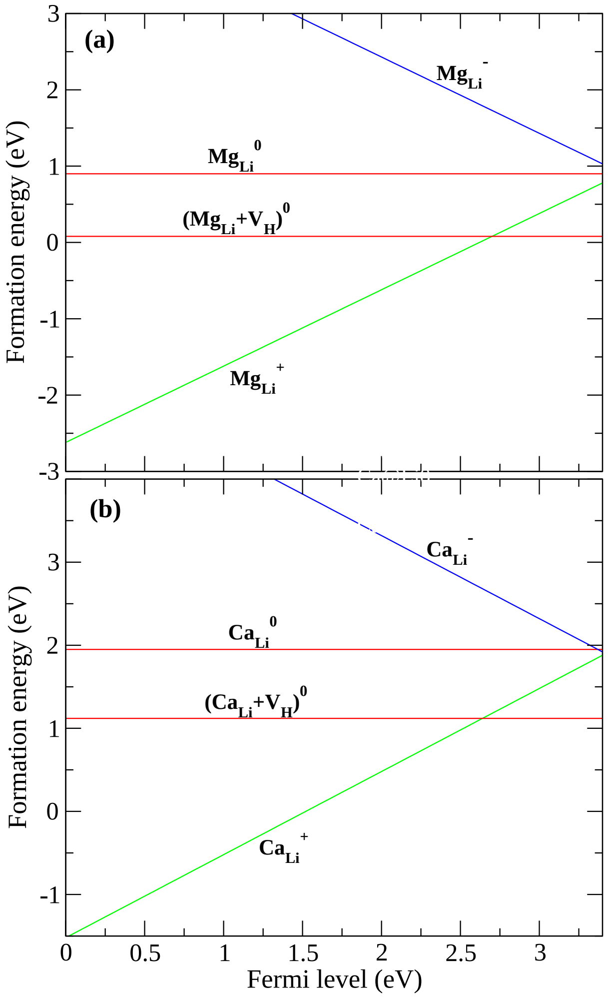

Figure 2.6: Calculated formation energies for (a) Mg and (b) Ca dopants on the Li site in $LiNH_2$.

section. The chemical potentials of the dopants are fixed by imposing equilibrium with their hydrides. For instance, for Ti we have

$$\mu_{\mathrm{Ti}} + 2\mu_{\mathrm{H}} = E_{\mathrm{tot}}[\mathrm{TiH_2}] \quad .$$

As a dopant atom can, in principle, be incorporated as an interstitial, a substitute for a Li atom or a substitute for a N atom, we also need μ_{N} from Eq. 2.7. ZPE corrections are included in $E_{\mathrm{tot}}[\mathrm{TiH_2}]$.

Our calculations show that, irrespective of the charge state q (q= -2, -1, 0, +1, +2, +3), it is by far most favourable for Ti to substitute a Li ion at a 2c position, cf. Fig. 2.1, $\mathrm{Ti}_{\mathrm{Li}}^{q}$. Substituting a N atom ($\mathrm{Ti}_{\mathrm{N}}^{q}$) or forming an interstitial ($\mathrm{Ti}_{\mathrm{i}}^{q}$) are unfavourable. We assume that this is general, i.e. that also Sc, Mg, and Ca preferentially substitute Li at 2c.[c]

---

[c] We checked, for various charge states, that Sc at a Li site is indeed more favorable than interstitial

The dopant impurity at the Li site is tetrahedrally coordinated by $[NH_2]^-$ units. We have carried out calculations with protons removed from a variable number of these $[NH_2]^-$. This enables these anions to catch an additional electron, thus oxidising the dopant atom, and formally becoming $[NH]^{2-}$, i.e. a V_H^-. We characterise the impurity complexes by the number of hydrogen atoms removed and their net charge. For instance, a $(Ti_{Li} + 2V_H)^+$ complex lacks two hydrogens and has a net total charge of +1. Chemically this complex is then a Ti^{4+} ion coordinated by two $[NH_2]^-$ and two $[NH]^{2-}$ ions. At the Ti_{Li} site the excess charge compared to Li^+ is +3. For the two $[NH]^{2-}$ ions the excess charge compared to $[NH_2]^-$ is -1. So the net charge of this complex is +1.

The formation energies of the Sc, Ti, Mg and Ca dopants and dopant complexes are shown in Figs. 2.5 and 2.6. The formation energies are always lowest for dopants in their highest oxidation state. With increasing Fermi energy E_F it becomes more favourable to expel more and more protons and accommodate the remaining electrons not at the Fermi level, but as $[NH]^{2-}$ ions. For instance, scandium is always present as Sc^{3+}, but for $E_F < 1.94$ eV all $[NH_2]^-$ ions are intact and we have Sc_{Li}^{2+}, for $1.94 < E_F < 2.15$ eV one $[NH]^{2-}$ ion is present and we have a $(Sc_{Li} + V_H)^+$. For $E_F > 2.15$ eV we have two $[NH]^{2-}$ ions, i.e. $(Sc_{Li} + 2V_H)$.

Such a behaviour was also described by Zhang *et al.*[94] for neutral Mg_{Li} in the lattice of $LiNH_2$. They calculated a formation energy for this substitution that is 0.6 eV larger than our value. This discrepancy can be ascribed to the different supercell size (our cell is four times larger) and to a different substitution site. Note that there are three inequivalent Li atoms in the unit cell of $LiNH_2$, see Fig. 2.1. If we use a smaller cell and change the substitution site, i.e. replace Li(2)(4*f*) with Mg instead of Li(3)(2*c*) in Fig. 2.1 the formation energy increases by 0.4 eV.

In Fig. 2.7, we combine the results for the formation energies of both intrinsic (H and Li) and extrinsic (Ti, Sc, Mg and Ca) defects from Figs. 2.2, 2.5, and 2.6. For the extrinsic defects only the most stable state is shown. The Fermi level in absence of dopants is indicated by the black vertical dashed line at 2.55 eV. First we note that the transition metal impurities, Ti and Sc, are not by themselves electrically active. They cannot exist in a charged state because no charge compensating intrinsic defects are available in the Fermi energy range where the most stable Ti and Sc complexes are positively charged. Therefore, if no other extrinsic impurities are present, they will remain in a neutral state and the Fermi level will be pinned at 2.55 eV by the intrinsic defects.

For the Ca and Mg complexes the situation is different. Their $\epsilon(+/0)$, i.e. charge transition levels, are some tenths of an eV above 2.55 eV. Controlling their concentration can, in principle, tune the Fermi energy over this range. If Ca or Mg impurities are

---

Sc.

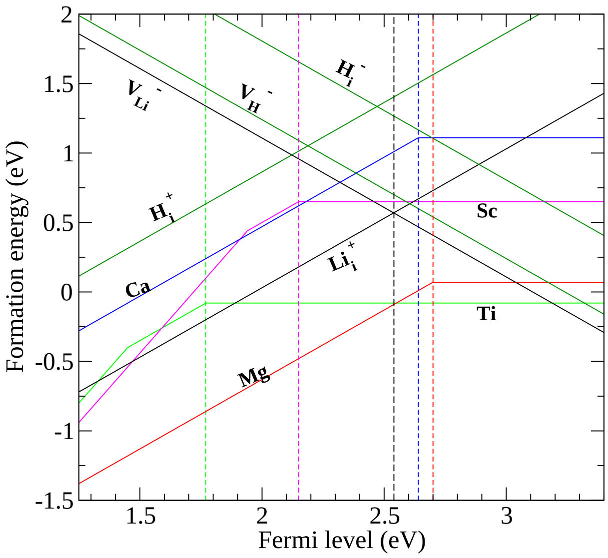

Figure 2.7: Calculated formation energies of both intrinsic (H and Li) and extrinsic (Ti, Sc, Ca, and Mg) defects in $LiNH_2$. The black dashed line denotes the Fermi level position resulting from charge neutrality in un-doped $LiNH_2$. Green, dark purple, blue, and red dotted lines denote the (0/+) transition levels, respectively, for Ti, Sc, Ca, and Mg. By increasing (decreasing) the temperature the whole plot moves to the left (right). Therefore the (0/+) transition levels remain unchanged relative to the intrinsic Fermi level position.

present in very large numbers, i.e. if their concentration is much larger than any of the intrinsic defect concentrations, these impurities pin the Fermi energy at their respective charge transition energies $\epsilon(+/0)$. The concentrations of V_{Li}^- and V_H^- are then increased according to Eq. 2.4, as an appropriate fraction of positive alkaline-earth species would take care of the charge compensation. For an increasing concentration of Mg impurities, the Fermi energy could increase by up to 0.15 eV, reducing $E_f[V_{Li}^-]$ and $E_f[V_H^-]$ to 0.42 and 0.55 eV, respectively and at the same time increase $E_f[Li_i^+]$ and $E_f[H_i^+]$ to 0.72 and 1.56 eV, respectively. This would increase the concentration of V_H^- by a few orders of magnitude.

The small formation energy of Mg impurities, cf. Figs. 2.6 and 2.7, indicates that Mg is easily incorporated in the $LiNH_2$ lattice and that the scenario sketched above is quite likely in the case of Mg. The formation energy of Ca impurities however is much higher than that of V_{Li}^-, V_H^- and Li_i^+ at $E_F = 2.55$ eV. This suggests that the concentration of Ca impurities is much smaller than that of the intrinsic impurities, and the Fermi level will not shift.

Of course, all our formation energies depend on the assumptions made for determining the chemical potentials in Eq. 2.5. For instance, if we would fix μ_{Ca} by demanding equilibrium with bulk Ca metal, we would stabilise the Ca impurity by 1.26 eV. However, we do not think that this is a realistic assumption. During a repeated (de)hydrogenation process any bulk Ca would be exposed to H_2 and experience a thermodynamic driving force to form CaH_2. Non-equilibrium conditions might apply, e.g., during ball-milling, but after repeated cycling these initial conditions do no longer necessarily apply.

The beneficial effects of Ti-based additives, such as $TiCl_3$ or nano-particles of TiO_2 or of pure Ti, on the kinetics of the (de)hydrogenation process, have been studied intensively.[16,91,107–109] Isobe *et al.* carried out X-ray absorption near-edge structure (XANES) measurements to characterise Ti added to $LiNH_2$ + LiH composite, after ball-milling the mixture.[109] In a first-principles study of the X-ray spectra, Tsumuraya *et al.* concluded that Ti ions occupy sites that are 4-fold coordinated by nitrogen, i.e. the Li sites in $LiNH_2$.[110] This geometry is consistent with our findings, i.e. our calculations also identify the Li site as the most favourable substitution site for Ti.

Matsumoto *et al.*[91] have demonstrated the somewhat peculiar "catalytic" action of Ti-additives such as $TiCl_3$. For the "catalysed" $LiNH_2$/LiH system they obtain an activation energy for thermal decomposition of 110 kJ/mol, which is quite close to the 128 kJ/mol found by Pinkerton for "un-catalysed" decomposition of pure $LiNH_2$ resulting in NH_3.[111] This similarity suggest that the Ti-species does not act as a usual catalyst, i.e. by reducing an activation barrier, but operates via a different mechanism. Also this is consistent with our results. Ti incorporated in the $LiNH_2$ lattice does not shift the Fermi level. Therefore, it does not change the concentrations of intrinsic defects, and does not affect the mass transport in the bulk material. Of course, on the basis of our calculations we cannot preclude specific catalytic activity of the Ti, e.g. at the amide surface. Interestingly, we observe that the Ti impurities are special in the sense that they have a *negative* formation energy in the whole Fermi energy range, see Fig. 2.7. This means that Ti gets easily incorporated into $LiNH_2$ in large quantities. This can have a large impact on the morphology of nano-scale amide grains, which other impurities such as Sc and Ca, for which incorporation into $LiNH_2$ is thermodynamically unfavourable, cannot have. Indeed, Matsumoto *et al.*[91] argue that Ti-based additives result in a large reactive surface in the amide/imide system, which enhances the kinetics of H_2 desorption.

Experimentally, replacing Li for Mg has been reported to decrease the hydrogen desorption temperature ($\Delta T = 50$ °C).[92,93] However, in these studies quite large amounts ($\sim 10\%$) of Mg have been used, so formation of, e.g., $Mg(NH_2)_2$ is likely. Our study shows that even a relatively low Mg concentration could have a substantial effect. As at the intrinsic Fermi level position in $LiNH_2$ the formation energy of Mg_{Li}^{+} is negative, Mg ions are easily incorporated, which might lead to a similar behaviour as in the case of Ti additives. In addition, the Fermi level is shifted for larger Mg concentrations, which decreases the formation energy of intrinsic defects.

2.5 Discussion & Conclusions

We discuss the possible role of defects in the initial phases of the conversion of $LiNH_2$ to Li_2NH. The equilibrium concentrations of intrinsic defects are quite low, i.e. $\leq 2\times10^{18}$ cm^{-3} for temperatures $T \leq 700$ K. Their relative concentrations depend very much on the type of defect. The Li-related defects Li_i^+ and V_{Li}^- are most abundant and determine the charge balance (Figs. 2.2, 2.4). Of the H-related defects, V_H^- is much more abundant than H_i^+. V_H^- in fact corresponds to a NH^{2-} ion in the amide lattice, whereas H_i^+ corresponds to a NH_3 molecule. Our results implicate that the equilibrium concentration of the latter species is negligible. The barriers for diffusion of intrinsic point defects are in the range 0.3–0.7 eV (Table. 2.2). Although such low barriers implicate that diffusion is relatively fast, the low concentration of intrinsic defects means that mass transport through the bulk mainly takes place via self-diffusion, where first a defect has to be formed before it can diffuse. The activation energies for self-diffusion of the Li-related defects Li_i^+ and V_{Li}^- are in the range 1.0-1.1 eV, whereas those of the H-related defects, V_H^- and H_i^+, are 1.4 and 1.8 eV respectively. This means that mass transport in $LiNH_2$ is quite slow, which is consistent with the relatively high temperatures needed for dehydrogenation.

If mass transport of hydrogen through the bulk has to take place via self-diffusion, then (V_H^-, H_i^+) pairs have to be created as a first step. This corresponds to the process

$$[NH_2]^- + [NH_2]^- \rightarrow [NH]^{2-} + NH_3, \tag{2.9}$$

where the right hand side corresponds to the (V_H^-, H_i^+) pair. A proton is shifted from one NH_2^- to another, resulting in a building block for the imide and an NH_3 incorporated into the lattice. This corresponds to a step in the mechanism for non-stoichiometric conversion from the amide to the imide as proposed in David *et al.*[80] From Table 2.2 one obtains a formation energy of 2.11 eV for the (V_H^-, H_i^+) pair. Note that this is the formation energy of a well-separated pair, which is required for mass transport. The formation energy of the (V_H^-, H_i^+) Frenkel pair is calculated as 1.66 eV.[d] These high formation energies show that the equilibrium concentration of such pairs is negligible.

In conclusion, the creation of ammonia molecules in the amide lattice is very unfavourable. We propose instead that NH_3 is formed only at the surface, where it can go in the gas phase or dissociate further, or at the interface with LiH, where it can react directly with LiH. The process to make the NH_3 is the same as in Eq. (2.9), but now both the NH_3 and the NH^{2-} species are created at the surface. NH_3 immediately

---

[d] The lowest energy cost to move a Li^+ in $LiNH_2$ which creates $[Li_iLiNH_2]^+$ and $[V_{Li}NH_2]^-$ species in the supercell is 0.72 eV and the lowest energy cost to move a proton from $[Li_iLiNH_2]^+$ to $[V_{Li}NH_2]^-$ is 0.88 eV. This makes that $\Delta E = 1.6$ eV.

reacts, or, alternatively, it goes into a gas phase. NH^{2-} effectively corresponds to a V_H^- defect. It has a low migration barrier (0.6-0.7 eV, see Table 2.2) and can easily diffuse into the bulk material. In parallel, the Li_i^+ ions that remain at the surface after NH_3 desorption, also diffuse into the material to keep the charge balance. Alternatively, they can recombine with the vacancies V_{Li}^- that are present inside the amide.

Incorporation of dopants in the form of Mg, Ca, Sc and Ti substitutional impurities into the amide lattice offers a little room to tune the concentration of intrinsic defects and hence the mass transport inside the amide material. The energy cost to incorporate Sc and Ca atoms is high. In contrast, the incorporation of Ti and Mg atoms is typically exothermic and should thus be easy. If present in the lattice in sufficient numbers, Mg and Ca species can shift the Fermi energy and thus reduce (increase) the E_f of the negative (positive) intrinsic point defects by 0.1 to 0.2 eV. This would (moderately) affect the defect concentrations, and therefore the mass transport and possibly the overall kinetics. Sc and Ti dopants have no such effect. However, as Ti and also Mg can be easily accommodated in the amide lattice, it is possible that their incorporation affects the morphology of nano-grains and can thus be related to the apparent catalytic effect of Ti-additives.[91]

Acknowledgements

This work is part of the research programs of Advanced Chemical Technologies for Sustainability (ACTS) and the Stichting voor Fundamenteel Onderzoek der Materie (FOM) with financial support from the Nederlandse Organisatie voor Wetenschappelijk Onderzoek (NWO).

Chapter 3

First-principles study of $LiBH_4$ nanoclusters and their hydrogen storage properties

Abstract

Recent experimental studies suggest faster desorption kinetics, improved reversibility, and more favorable thermodynamics for confined $LiBH_4$ nanoparticles as compared to bulk. We study the structures, total energies, and decomposition reactions of $LiBH_4$ nanoparticles using density functional theory calculations. We find that the reaction energies of nanoclusters with a diameter $\gtrsim 2$ nm are very close to that of bulk $LiBH_4$. Only very small clusters with a diameter < 1 nm are significantly destabilized relative to the bulk. The thermodynamics of such small clusters is unfavorable, however, and leads to dehydrogenation temperatures that are higher than that of the bulk. Although small $(LiBH_4)_n$ nanoclusters exhibit a number of different geometries, they show only little variation in the total energy per formula unit. Of all possible decomposition reactions of $(LiBH_4)_n$, the reaction where diborane is released, is unfavorable for most cluster sizes, whereas the hydrogen desorption reaction to $Li_2B_{12}H_{12}$ is most favorable. This suggests that the experimentally observed improvement of the (de)hydrogenation properties of $LiBH_4$ can be attributed to an improvement of the kinetics of the latter reaction.

Ebrahim Hazrati, Geert Brocks, and Gilles A. de Wijs, J. Phys. Chem. C 2012, **116**, 18038-18047

3.1 Introduction

Storage of hydrogen in small volumes at ambient temperature and moderate pressure is a bottleneck for realizing hydrogen energy systems in the near future. Solid state reversible hydrogen storage systems are of great interest for this purpose.[112] A successful system should have large gravimetric and volumetric storage capacities, suitable thermodynamic properties, and fast hydrogen absorption and desorption kinetics. A gravimetric capacity of 18.5 wt% makes $LiBH_4$ one of the most interesting complex hydrides for hydrogen storage.[6,7,20–23] However, $LiBH_4$ is a relatively stable material that decomposes at a high temperature $\gtrsim$ 400 °C. Furthermore, rehydrogenation is only possible at extreme conditions with typical values for temperature and pressure of 600 °C and 350 bar H_2. In addition, de/rehydrogenation kinetics is slow, which is a common problem for the bulk complex hydrides.[6,24–26]

A recently adopted approach that helps to address such problems, is nanoconfinement in porous materials.[27] As solid state reactions involve mass transport into separate solid phases, such reactions should proceed faster for small nanoparticles, as transport distances become shorter. Recent experiments on $NaAlH_4$, for instance, show that the confinement of $NaAlH_4$ in porous carbon indeed improves the H_2 sorption kinetics.[30,31] Somewhat surprisingly, nanoconfinement also alters the decomposition thermodynamics. Decomposition of $NaAlH_4$ to NaH, Al and H_2 normally proceeds via an intermediate step in which Na_3AlH_6 is formed. In the decomposition reaction of $NaAlH_4$ nanoparticles, no evidence of Na_3AlH_6 has been found. This observation is supported by calculations,[32,33] which show that $NaAlH_4$ nanoparticles in vacuum with diameters in the 1-10 nm range preferentially decompose in a single step. Na_3AlH_6 nanoparticles are not formed because of their relatively high surface energy.[32]

Changes in the thermodynamics of nanoparticles, compared to bulk systems, can generally be analyzed in terms of surface energies, which become more important as the particles become smaller.[113] Very small nanoparticles may not resemble bulk at all, and have very different thermodynamic properties. For instance, calculations on MgH_2 nanoclusters show that the hydrogen desorption energy can be reduced significantly for particles with diameters below 1.3 nm.[114]

Improving the sorption properties of $LiBH_4$ by nanoconfinement in porous materials has become the focus of much experimental work.[34–45] Faster dehydrogenation kinetics is reported for $LiBH_4$ infiltrated in carbon aerogels, nanoporous carbon, or nanoporous silica, accompanied by a decrease of the dehydrogenation temperature by at least 100 °C. In addition, confinement of $LiBH_4$ in nanoporous carbon leads to a marked improvement of the reversibility of the hydrogen desorption. As with $NaAlH_4$, the improved properties of nanoconfined $LiBH_4$ can have a kinetic, as well as a thermodynamic origin.

In this work we study the energetics and possible thermodynamic decomposition pathways of $LiBH_4$ nanoclusters by first-principles density functional theory (DFT) calculations. For small clusters with diameters in the 1-2 nm range, we explicitly generate and optimize the geometries of $LiBH_4$ and possible product clusters. Larger clusters are generated starting from bulk structures, calculating the energies of possible surface terminations, and applying the Wulff theorem to construct crystallite equilibrium shapes.[115]

The paper is organized as follows. In Sec. 3.2 we describe the computational procedures used. Sec. 3.3.1 discusses the structures and the energetics of $LiBH_4$ and product clusters. These data are used in secs. 3.3.2 and 3.3.2 to construct possible decomposition pathways for $LiBH_4$ nanoclusters. We summarize the conclusions in Sec. 3.4.

3.2 Computational Methods

First-principles calculations were performed in the framework of density functional theory (DFT)[48,49] using the PBE generalized gradient approximation (GGA)[50] and the projector augmented wave method (PAW)[51,52] as implemented in the Vienna *ab initio* simulation program (VASP).[53,54] For H and Li all-electron PAW data sets were used whereas for B the 1s core state was kept frozen. A kinetic energy cutoff of 500 eV was employed for the plane wave expansion of the Kohn-Sham orbitals. The energies of nanoclusters were calculated in a periodically repeated cubic box which included at least 12 Å of vacuum in each direction to separate the periodic images. Dipole corrections were found to be negligible, even for the polar LiB and $LiBH_4$ clusters. The energies of isolated H_2 and B_2H_6 molecules were calculated in cubic boxes with sizes of 12 Å and 14 Å, respectively.

For structural optimization of the nanoclusters only the Γ point was used to sample the Brillouin zone. The internal atomic positions were optimized with the conjugate gradient method until the forces on atoms were less than 0.01 eV/Å. This is sufficient to obtain converged total energies. However, if accurate vibrational frequencies are required, we have found it necessary to perform additional optimizations on the clusters. The frequencies are needed to obtain reliable free energies.

For some clusters, we used simulated annealing as part of the structure optimization procedure. This was done by first-principles molecular dynamics, using a Nosé thermostat to set the temperature.[116–118] We used a standard velocity Verlet scheme with a time step of 0.4 fs to integrate Newton's equations of motion. For the molecular dynamics calculations, we also used Γ point sampling but a lower kinetic energy cutoff of 240 eV.

The ground state geometries of small clusters, $(X)_n$, X= $LiBH_4$, Li, LiH, LiB and B, with $n \leq 12$, and $Li_2B_nH_n$, were found by relaxation starting from a large number of trial geometries and selecting the structures with lowest total energies. The moderately large cluster $(LiBH_4)_{56}$ was obtained by cutting it from the bulk structure, while exposing the low-energy (100), (010) and (101) surfaces, after which the structure was relaxed. The total energy of this cluster is then within 0.01 eV/f.u. to that obtained by using the (macroscopic) Wulff construction. This suggests that we can use the Wulff approach to predict the energies of larger clusters.

To bridge the gap between small ($n \leq 12$) and large ($n \geq 56$) $(LiBH_4)_n$ clusters, we explored several techniques to generate structures with an intermediate size. For instance, a $(LiBH_4)_{21}$ cluster was constructed by joining two $(LiBH_4)_{12}$ clusters in a face-sharing geometry, i.e., the clusters share one “hexagonal” face with alternating Li^+ and $[BH_4]^-$ units at the vertices, see the next section. The geometries of $(LiBH_4)_{32}$ and $(LiBH_4)_{54}$ clusters were obtained by simulated annealing. The initial configurations were clusters cut from the bulk. The $(LiBH_4)_{32}$ cluster was heated to 388 K in 1.0 ps, kept at 388 K for $\sim$ 0.5 ps and subsequently cooled down to 73 K in $\sim$ 2.7 ps. The larger $(LiBH_4)_{54}$ cluster underwent a more extensive annealing cycle. It was heated to 573 K in $\sim$ 0.4 ps, kept at that temperature for about 2 ps and cooled down in $\sim$ 5 ps. Finally, we optimized these structures using the conjugate gradient method, with 500 eV cutoff.

The Wulff construction requires the energies of macroscopic crystal surfaces. These were calculated from slabs with a thickness of at least 28 Å to ensure convergence. At least 13 Å of vacuum separated the slabs to prevent unwanted interactions between the periodic images. Surface energies were fully converged with respect to the number of *k*-points. All the slabs studied were stoichiometric with similar surfaces on both sides. In-plane lattice parameters were fixed to the optimized bulk parameters and all atoms in the slab were allowed to relax.

Lattice vibrational frequencies were calculated for most solids and some of the clusters using the finite difference methods of Ref. 119. For the solids, supercells containing several primitive unit cells were used, so as to ensure good accuracy of phonon frequencies throughout the Brillouin zone.

3.3 Results

3.3.1 Nanocluster Geometries and Energetics

The optimized geometries of some of the $(LiBH_4)_n$ clusters are shown in Figure 3.1. Full structural details are provided as Supporting Information (SI), Tables S1-S14. In bulk $LiBH_4$ the $[BH_4]^-$ anions are tetrahedrally coordinated by Li^+ cations, and vice versa. The orientation of the $[BH_4]^-$ anion with respect to the Li^+ cation is described

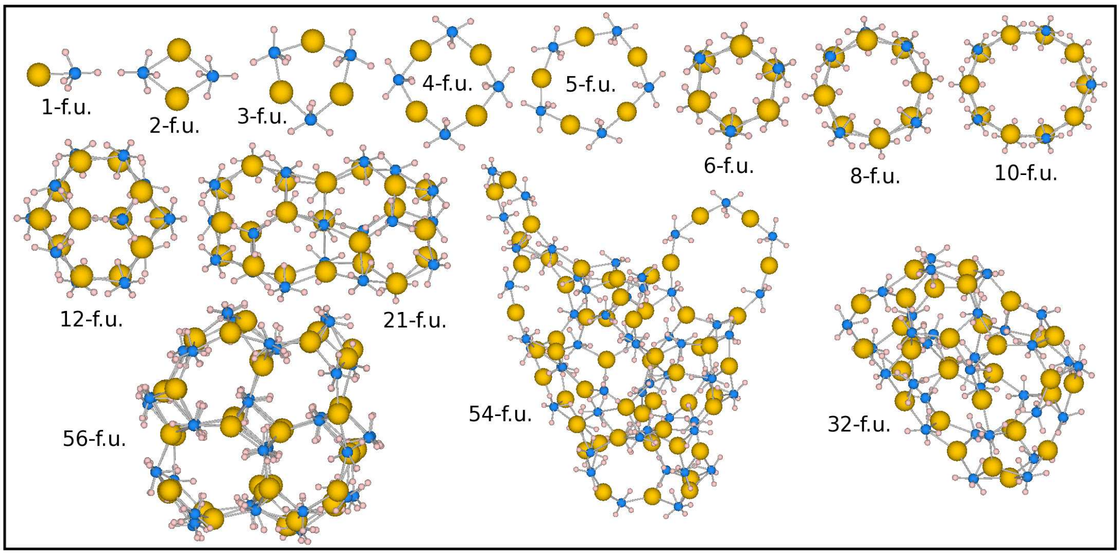

Figure 3.1: The optimized geometries of $(LiBH_4)_n$ clusters, visualized using the VESTA program.[120]

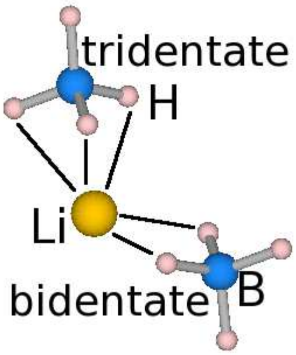

Figure 3.2: Illustration of bidentate and tridentate coordinations of Li^+ with a $[BH_4]^-$ anion.[120]

as bidentate or tridentate, depending on whether two or three hydrogen atoms are pointing toward the Li^+ cation (see Figure 3.2).[121–123] In bulk $LiBH_4$ each Li^+ has three $[BH_4]^-$ anions with bidentate, and one with tridentate orientations in its first coordination shell. In a packed structure, the difference in energy between bidentate and tridentate orientations is small, and the relative orientation of $[BH_4]^-$ anions is guided by the (Coulomb) repulsion between the hydrogens on the different anions. Details can be found in Ref. 121.

The $[BH_4]^-$ anion in the $(LiBH_4)_1$ molecule is oriented in the tridentate configuration. It changes to bidentate in $(LiBH_4)_2$ where the two Li^+ cations form a double bridge between the $[BH_4]^-$ anions. $(LiBH_4)_{3-5}$ clusters have ring structures with tridentate orientation of $[BH_4]^-$ anions. The structures of $(LiBH_4)_{6,8,10}$ clusters consist

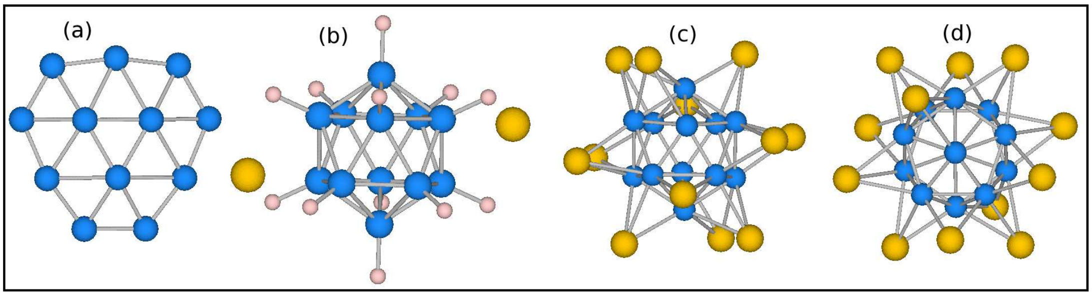

Figure 3.3: The optimized geometries of (a) B_{12}, (b) $Li_2B_{12}H_{12}$ and (c,d) two views of $Li_{12}B_{12}$.[120]

of two of such rings on top of one another. The two circles are positioned such that a $[BH_4]^-$ anion is on top of a Li^+ cation, and vice versa. Each Li^+ is then coordinated by three $[BH_4]^-$ ions in bidentate orientation.

$(LiBH_4)_{12}$ is the first cluster with a true three-dimensional geometry. Its structure is cage-like with eight six-membered rings and six four-membered rings, where each ring consists of alternating Li^+ and $[BH_4]^-$ ions. The $[BH_4]^-$ ions are in bidentate orientation and the Li^+ coordination number is three. The cluster diameter is approximately 9 Å. The $(LiBH_4)_{21}$ cluster is constructed by fusing two $(LiBH_4)_{12}$ clusters along a six-membered ring. Therefore, their ions have the same orientation and coordination number.

As discussed in the previous section, the geometries of $(LiBH_4)_{32}$ and $(LiBH_4)_{54}$ clusters are obtained by simulated annealing. In both structures, the coordination number of most Li^+ cations is three, as in the smaller clusters. Some ions in $(LiBH_4)_{54}$ have coordination numbers two or four. In particular, at the exterior of $(LiBH_4)_{54}$ some ring-like structures appear that resemble the smaller clusters. The particular structures of the $(LiBH_4)_{32}$ and $(LiBH_4)_{54}$ clusters shown in Figure 3.1 might well represent local energy minima instead of the global energy minimum. The effect this has on the total energy per formula unit (f.u.) is minor, however, see below.

The $(LiBH_4)_{56}$ cluster is initially constructed as a cut from the bulk structure, as discussed in the previous section. After optimization, some of the Li^+ cations which were initially located at the surface of the cluster have relaxed into the cluster leaving $[BH_4]^-$ anions exposed at the surface. Although the relaxations are quite substantial for the ions located in the surface region of the cluster, the impact this has on the total energy per f.u. is minor. After optimization, the nanocluster dimensions are 13.7 × 15.2 × 14.0 $Å^3$.

As we are interested in the dehydrogenation of $(LiBH_4)_n$ clusters, we also study the structures of clusters of possible dehydrogenation products. The mass balance and the energetics of the dehydrogenation reaction limit the number of possible products. Still, in particular for clusters containing boron there remain several options. As an example, Figure 3.3 shows the structures of clusters of different composition that contain twelve boron atoms.

One possible reaction path leads to pure boron clusters B_n. All boron clusters considered here have a rather flat geometry, with an occasional buckling or curvature. These structures are consistent with those reported in the literature.[124] They resemble finite cuts from (quasi) planar 2D boron sheets.[125–127]

Considering boranes B_nH_m one notices that the closo-borane anions $[B_nH_n]^{2-}$ are particularly stable.[128] Indeed $[B_nH_n]^{2-}$ ions exhibit HOMO-LUMO gaps of several eVs in our calculations. In the dehydrogenation of $(LiBH_4)_n$ clusters one should therefore consider $Li_2B_nH_n$ clusters as possible products. $Li_2B_nH_n$, $n \geq 5$, clusters have a similar structure as the example $Li_2B_{12}H_{12}$ shown in Figure 3.3(b). The hydrogens are bonded to the boron atoms residing at the vertices of a closed, cage-like structure. The smaller $Li_2B_nH_n$, $n \leq 4$ have the boron atoms bonded in a planar structure with hydrogen atoms bonded to boron atoms at the outside. Consideration of borane species B_nH_m, $m \neq n$, turns out to lead to reaction paths in the dehydrogenation of $(LiBH_4)_n$ clusters that are energetically not competitive, so we will not discuss the structure of those species.

Of the Li substituted boranes Li_mB_n only the hypercloso species, i.e. $m = n$, turn out to yield energetically viable dehydrogenation products. The structure of Li_nB_n is similar to that of the closo-borane $[B_nH_n]^{2-}$ anions, in the sense that the boron atoms form a cage-like structure, see Figure 3.3(c,d) and Table S4 in the SI. However, unlike hydrogen atoms, each of which is covalently bonded to one boron atom, Li atoms are positioned on the faces and edges of the boron cage. As Li is more electropositive than H, it largely donates its valence electron to the electron deficient boron cage, making the Li-B bonding largely ionic. The most favorable positions of the Li^+ ions are then close to the surface of the negatively charged boron cage and the ions are distributed evenly over the surface, such as to minimize Coulomb repulsion.[127]

The total energies of the nanoclusters are listed in Table 3.1. As we are interested in the energy difference between the nanocluster and the corresponding bulk material as a function of the nanocluster size, the zero-point vibrational energies (ZPEs) largely cancel out, so they are not included in Table 3.1. For comparison, the total energies per f.u. of the corresponding bulk materials are also included. At room temperature bulk $LiBH_4$ has an orthorhombic structure belonging to the *Pnma* space group (No. 62). Our optimized lattice constants are a=7.30 Å, b=4.41 Å and c=6.60 Å, in good agreement with the experimental values a=7.178 Å, b=4.436 Å and c=6.803 Å.[134]

The general trend for all the nanoclusters in Table 3.1 is that upon increasing the

Table 3.1: Total Energies in eV for Li_n, $(LiH)_n$, $(LiBH_4)_n$, $(LiB)_n$, B_n, and $Li_2B_nH_n$ Nanoclusters Divided by *n*. Zero-point energies are not included.

n	Li_n	$(LiH)_n$	$(LiBH_4)_n$	$(LiB)_n$	B_n	$Li_2B_nH_n$
1	-0.30	-3.74	-22.69	-1.72		
2	-0.73	-4.79	-23.47	-5.06	-1.71	-9.60
3			-23.71			
4	-0.96	-5.34	-23.80	-6.90	-4.28	-10.44
5			-23.81			
6	-1.13	-5.48	-23.91	-7.34	-4.75	-10.87
8	-1.25	-5.56	-23.98	-7.43	-5.22	-10.73
10	-1.29	-5.60	-23.99	-7.67	-5.47	-10.82
12	-1.32	-5.66	-24.04	-7.71	-5.62	-10.94
21			-24.05			
32			-24.01			
54			-23.99			
56			-24.03			
bulk	-1.91[a]	-6.13[b]	-24.16	-8.91[c]	-6.68[d]	-11.09[e]

[a] bcc-Li.[129];

[b] Cubic Fm$\bar{3}$m (No. 225).[130];

[c] Hexagonal P6_3/mmc (No. 194).[131];

[d] α-rhombohedral boron.[132];

[e] $Li_2B_{12}H_{12}$, cubic Pa$\bar{3}$ (No. 205).[133]

nanocluster size, their stability increases toward the bulk values. The total energy of $(LiBH_4)_n$ clusters converges relatively quickly to the bulk value. For $n = 12$, which corresponds to a cluster diameter of ~ 0.9 nm, the energy difference between cluster and bulk is ~ 0.1 eV/f.u.. These results are in contrast to those found in Ref. 135, where it is reported that $LiBH_4$ nanoclusters with diameters smaller than 1.75 nm are strongly destabilized relative to the bulk. We do not find such strong destabilization, indicating that our cluster geometries are more stable.

Another important observation is that $(LiBH_4)_n$ clusters with $n \geq 12$ have very similar energies, although their structures are very dissimilar, i.e., cage-like structures for $n = 12$ and 21, amorphous-like structures for $n = 32$ and 54 and a bulk-like structure for $n = 56$.

In Figure 3.4, we plot the energy difference between the nanoclusters and their corresponding bulk materials as a function of the nanocluster size up to 12 f.u.. The energies of $Li_2B_nH_n$ clusters in Table 3.1 are not shown, as corresponding bulk materials are not always known. The $Li_2B_nH_n$ energies do not strongly dependent on n. The energy of $(LiBH_4)_n$ clusters converges fastest to the bulk value. The Li_n and $(LiH)_n$ clusters are destabilized with respect to the bulk in a similar way. B_n and $(LiB)_n$ clusters exhibit the strongest destabilization. We will rationalize these trends in terms of surface energies.

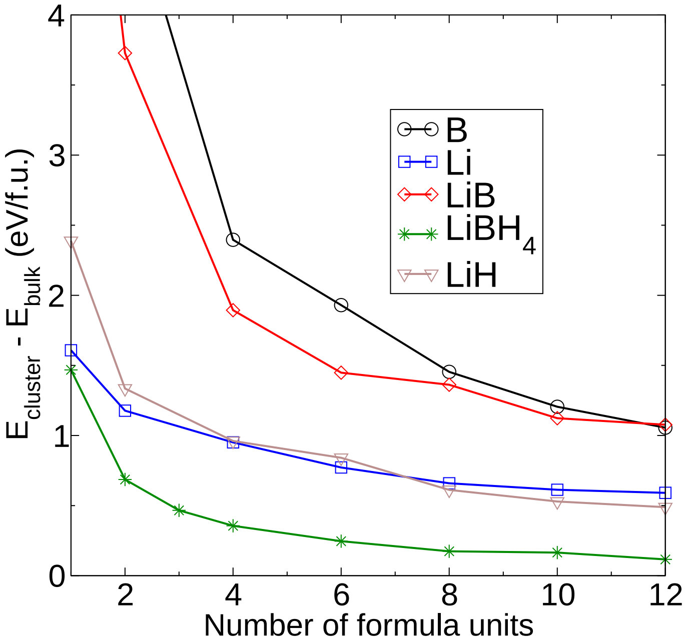

Figure 3.4: The energy difference per f.u. between the nanocluster and the corresponding bulk material as a function of the number of f.u.. The symbols are calculated results; the solid lines guide the eye.

The stability of $LiBH_4$ nanoclusters relative to the bulk is related to the fact

Table 3.2: Calculated Bulk $LiBH_4$ Surface Energies in J/m^2 for Low-Index Surfaces.

	This work	Ref. 135	Ref. 136
Surface			
(010)	0.102	0.110	0.119
(101)	0.115	0.112	0.125
(100)	0.113	0.115	0.116
(011)	0.097	0.212	
(111)	0.165	0.231	
(201)	0.144	0.303	
(001)	0.314	0.336	0.347
(110)	0.214	1.210	

that surface energies are very low for $LiBH_4$. Calculated energies of surfaces of the orthorhombic $LiBH_4$ bulk structure, compared to results reported in the literature, are listed in Table 3.2. All of the surfaces in Table 3.2 are apolar surfaces, classified as “type 1” in Ref. 137. We find that the (100), (010), (101) and (011) surfaces have very similar surface energies in the range 0.10-0.12 J/m^2. These surfaces have equal numbers of $[BH_4]^-$ anions and Li^+ cations in the surface plane and the relaxations of the ions in the surface region are very small.

In comparison to Ref. 135, our calculated (011), (201), and (110) surface energies are considerably lower. Apparently the structures we find for these surfaces are more stable. In particular, the surface energy we find for the (110) surface, 0.2 J/m^2, is roughly twice the value found for the more stable surfaces, e.g. (010) or (100). This is unlike the (110) surface energy of 1.2 J/m^2 found in Ref. 135, which is an order of magnitude higher than that of the (010) and (100) surfaces. We suggest these differences may be explained by different surface terminations. For instance, for a (011) surface with a different termination we obtain a surface energy of 0.259 J/m^2, which is much closer to the value reported in Ref. 135. Of course, the terminations with lowest energy are more likely to occur in practice. Figure 3.5 shows the side views of the (011), (201) and (110) surfaces after relaxation. The lateral dimensions of the (011) and (110) surface unit cells are 7.35×7.92 and 8.56×6.58 Å^2, respectively. The (201) surface has a surface unit cell with lateral dimensions of 4.40×15.08 Å^2.

$(LiH)_n$ clusters are less stable than $(LiBH_4)_n$ clusters compared to their respective bulk states, see Figure 3.4. Both are ionic compounds, but the packing of the ions in LiH is denser than in $LiBH_4$. The nearest neighbor cation-anion distances in LiH and

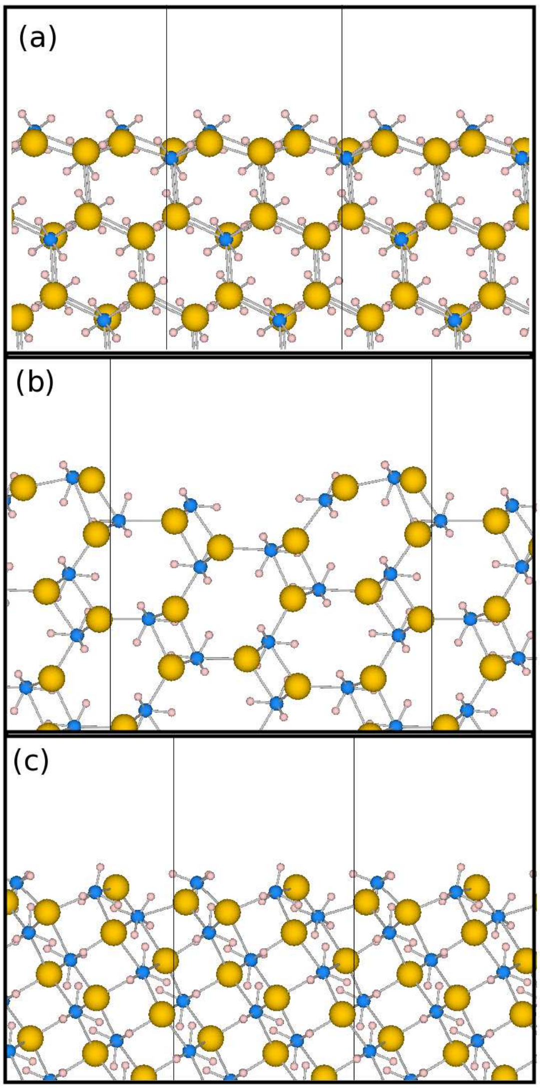

Figure 3.5: Side views of the (a) (011), (b) (201) and (c) (110) surfaces of bulk $LiBH_4$. The thin lines indicate the unit cell.

$LiBH_4$ are 2.0 and 2.5 Å, respectively, and the coordination numbers are 6, respectively 4. One therefore expects the ionic (Madelung) bonding in LiH to be stronger, which likely leads to higher surface energies.[138] Indeed, for the (100) surface, which is the lowest energy surface of (rocksalt) LiH, we calculate a surface energy 0.319 J/m^2. This is roughly three times the energy of the lowest energy surfaces of $LiBH_4$, cf. Table 3.2, explaining the relative stability of $(LiH)_n$ and $(LiBH_4)_n$ clusters.

Li_n clusters are fairly unstable, which results from the relatively large cohesive energy (1.6 eV/atom) of the Li metal,[139] implying high energy penalties for making surfaces. Indeed the energy of the (bcc) (001) Li surface is 0.522 J/m^2, which is large for an alkali metal. The (001) surface energy decreases sharply going down the column of alkali metals in the periodic table. For Na it is 0.261 J/m^2, and for Cs it is a mere 0.095 J/m^2.[140] Note that the surface energy of Li is even higher than that of LiH. This implies that large LiH clusters are relatively more stable than large Li clusters, as can be observed in Figure 3.4.

Bulk boron is a covalently bonded network, so any finite boron fragment or cluster is likely to have a considerable number of unsaturated or strained bonds. Hence the energy of boron clusters is relatively high. The properties of $(LiB)_n$ clusters can not be directly linked to the properties of bulk LiB. $(LiB)_n$ nanoclusters and bulk LiB are very different from both structural and bonding point of view[a].[141]

3.3.2 Decomposition of $(LiBH_4)_n$ Clusters

Small Clusters, $n \leq 12$

In the following, we study the effects of the cluster size on the decomposition pathway of $(LiBH_4)_n$ clusters with n up to 12 formula units. In the next subsection, we study such size effects on larger clusters.

The decomposition reaction of bulk $LiBH_4$ takes place at a high temperature ($T > 400$ °C), and is proposed to proceed as[142,143]

$$\begin{aligned} \mathrm{LiBH_4} &\leftrightarrow \frac{1}{12}\mathrm{Li_2B_{12}H_{12}} + \frac{5}{6}\mathrm{LiH} + \frac{13}{12}\mathrm{H_2(g)}, \qquad (3.1)\\ &\leftrightarrow \mathrm{LiH} + \mathrm{B} + \frac{3}{2}\mathrm{H_2(g)}, \qquad (3.2)\end{aligned}$$

where the first step leads to the formation of $Li_2B_{12}H_{12}$ as an intermediate product. We calculate a reaction energy (at $T = 0$ K) for reaction (3.1) of 0.39 eV/$LiBH_4$, including the contributions of the ZPEs. For the overall reaction (3.2) we find an energy 0.84 eV/$LiBH_4$, including ZPE contributions, confirming that the first reaction step is indeed favorable. The calculated formation energy of $LiBH_4$ with respect to the solids Li and B is 1.64 eV/$LiBH_4$. All these numbers are in good agreement with calculated values reported in the literature.[144–146]

Recently, it has been argued that the first step reaction in fact produces diborane (B_2H_6) as intermediate product, which decomposes in a second step at $T > 250$ °C to B and H_2.[147] It is then proposed that $Li_2B_{12}H_{12}$, and an amorphous $Li_2B_{10}H_{10}$ phase, are formed only in a side-reaction between diborane and the unreacted $LiBH_4$ at lower temperatures. The first reaction step is then

$$\mathrm{LiBH_4} \leftrightarrow \mathrm{LiH} + \frac{1}{2}\mathrm{B_2H_6(g)}. \qquad (3.3)$$

---

[a] The crystal structure of LiB can be described as infinite, linear chains of B atoms in a Li matrix with covalent bonds between B atoms and Lithium as Li^+.

Motivated by these studies, we consider the following possible decomposition reactions for $(\mathrm{LiBH_4})_n$ clusters,

$$(\mathrm{LiBH_4})_n \leftrightarrow \mathrm{Li_2B}_n\mathrm{H}_n + (\mathrm{LiH})_{n-2} + (n+1)\mathrm{H_2(g)}, \quad (n \leq 12) \tag{3.4a}$$

$$(\mathrm{LiBH_4})_n \leftrightarrow \frac{1}{12}(\mathrm{Li_2B_{12}H_{12}})_\mathrm{n} + \frac{5}{6}(\mathrm{LiH})_\mathrm{n} + \frac{13\mathrm{n}}{12}\mathrm{H_2(g)}, \quad (n > 12) \tag{3.4b}$$

and

$$(\mathrm{LiBH_4})_n \leftrightarrow (\mathrm{LiH})_n + \frac{n}{2}\mathrm{B_2H_6(g)}, \tag{3.5}$$

$$(\mathrm{LiBH_4})_n \leftrightarrow (\mathrm{LiH})_n + (\mathrm{B})_n + \frac{3n}{2}\mathrm{H_2(g)}, \tag{3.6}$$

$$(\mathrm{LiBH_4})_n \leftrightarrow (\mathrm{LiB})_n + 2n\,\mathrm{H_2(g)}, \tag{3.7}$$

$$(\mathrm{LiBH_4})_n \leftrightarrow (\mathrm{Li})_n + (\mathrm{B})_n + 2n\,\mathrm{H_2(g)}. \tag{3.8}$$

Several other reactions were tried as well, e.g., reactions leading to final states with different $\mathrm{B}_n\mathrm{H}_m$ molecules. They yielded high reaction energies, however, and are therefore not discussed here. The desorption energies, i.e. the energies of reactions (3.4a)-(3.8), normalized per gas molecule ($\mathrm{H_2}$ or $\mathrm{B_2H_6}$), are shown in Figure 3.6 as a function of cluster size. Reaction (3.4b) will be discussed in Sec. 3.3.2, where clusters with $n > 12$ will be addressed.

Figure 3.6 shows that the desorption energies decrease with increasing the cluster size for all possible reaction paths. The reason for this becomes clear by considering Figure 3.4. The reactant clusters $(\mathrm{LiBH_4})_n$ are much more stable with respect to bulk, than the product clusters $\mathrm{Li_2B}_n\mathrm{H}_n$, $(\mathrm{LiH})_n$, Li_n, $(\mathrm{LiB})_n$ and B_n. More energy has to be supplied to form the products if the reactions are performed on clusters rather than on bulk. So from the perspective of the thermodynamics of dehydrogenation it is not advantageous to use $(\mathrm{LiBH_4})_n$ nanoclusters instead of bulk $\mathrm{LiBH_4}$. Small nanoclusters release hydrogen at higher temperatures compared to large clusters or bulk.

The desorption reactions where $\mathrm{H_2}$ is released, i.e. reactions (3.4a), (3.6), (3.7), and (3.8), can be compared to one another. The reaction with the lowest desorption energy gives the lowest desorption temperature at fixed hydrogen pressure (or the highest hydrogen pressure at a fixed temperature). According to Figure 3.6 reaction (3.4a) is the most favorable, except for the smallest clusters $n \leq 4$. This reaction gives $\mathrm{Li_2B}_n\mathrm{H}_n$ and $(\mathrm{LiH})_{n-2}$ clusters as products. The relative ease of this reaction is in line with the relative high stability of the closo-borane $\mathrm{Li_2B}_n\mathrm{H}_n$ molecules, cf. Figure 3.3(b).[128] The reaction is the cluster equivalent of the bulk reaction (3.1).[142–144,146,147]

In a reaction step following reaction (3.4a), $\mathrm{Li_2B}_n\mathrm{H}_n$ clusters might decompose into LiH and B,

$$\mathrm{Li_2B}_n\mathrm{H}_n + (\mathrm{LiH})_{n-2} \leftrightarrow (\mathrm{LiH})_n + \mathrm{B}_n + \frac{n-2}{2}\mathrm{H_2(g)}. \tag{3.9}$$

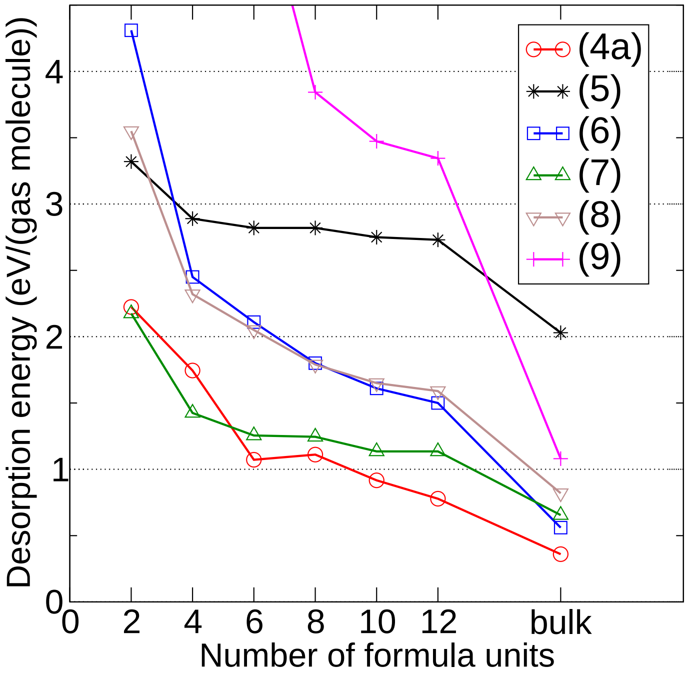

Figure 3.6: Calculated desorption energies with zero-point energy corrections of $LiBH_4$ for bulk and nanoclusters $2 \leq n \leq 12$. Desorption energies are in eV/H_2 [reactions (3.4a), (3.6), (3.7), (3.8), (3.9)] and eV/B_2H_6 [reaction (3.5)]. The bulk limit of reaction (3.4a) is reaction (3.4b), i.e., decomposition into bulk $Li_2B_{12}H_{12}$.

The sequence of reaction steps (3.4a) and (3.9) then corresponds to the overall reaction (3.6). The second step reaction (3.9), which is equivalent to the bulk reaction (3.2), is however energetically very unfavorable, as is shown in Figure 3.6. This means it would take place at a much higher temperature. For $n = 12$ reaction (3.4a) releases approximately 10 wt% hydrogen, whereas reaction (3.9) would release a further 4 wt%.

Reaction (3.7) is competitive with reaction (3.4a) for very small clusters, $n \leq 4$, see Figure 3.6. Reaction (3.7) yields a complete dehydrogenation, with $(LiB)_n$ clusters as product. This reaction becomes relatively less favorable the larger the cluster, and is definitely unfavorable for the bulk. Apparently, very small $(LiB)_n$ clusters adopt structures that are relatively stable. Reactions (3.6) and (3.8) are less favorable for $(LiBH_4)_n$ clusters with $n \leq 12$. For such clusters these two reactions have a comparably high hydrogen desorption energy. This means that reaction (3.6) would only occur at a high temperature, where $(LiH)_n$ clusters would dehydrogenate immediately (for $n \leq 6$). This is not true anymore for the bulk, where reaction (3.6) becomes more advantageous than either reactions (3.7) or (3.8).

To be able to compare the reaction where B_2H_6 is released, to those where hydrogen is released, we consider the change in Gibbs free energy $\Delta G(T)$ of the reactions.

We calculate $G(T)$ of the bulk crystals and of the clusters [b] from the DFT total energies and the vibrational densities of states,[122] where we assume that the clusters are immobilized by confinement in a porous material (so we neglect contributions to the free energy due to translational and rotational degrees of freedom). The free energies of H_2 gas and B_2H_6 gas are taken from the literature, using a gas pressure of 1 bar[c] Figure 3.7 shows $\Delta G/\mathrm{LiBH_4}$ f.u. as a function of temperature for reactions (3.4a)-(3.8), for two sizes of clusters, $n = 4$ and $n = 12$, and for bulk. Reaction equilibrium is achieved at a temperature T_d at which $\Delta G(T_d) = 0$.

The small cluster $(\mathrm{LiBH_4})_4$ decomposes only at a very high temperature $T_d \gtrsim 1000$ K. The two reactions (3.5) and (3.7), which involve desorption of B_2H_6 and H_2, respectively, are then competitive. The decomposition temperature decreases with increasing cluster size. The larger cluster $(\mathrm{LiBH_4})_{12}$ decomposes at $T_d \approx 800$ K. The most favorable reaction path is now presented by reaction (3.4a), where hydrogen is desorbed and $\mathrm{Li_2B_{12}H_{12}}$ clusters are formed. Reaction (3.7) is the second most favorable reaction, but it will not be very important, as it occurs at a much higher temperature. Reaction (3.5) is even less favorable, which means that from a thermodynamic point of view it is unlikely that B_2H_6 gas is formed in the decomposition of larger clusters.

The trend in lowering the decomposition temperature with increased cluster size is continued to the bulk, which decomposes at $T_d \approx 400$ K via the reaction (3.4a). The latter is equivalent to the bulk reaction (3.1). Reaction (3.6) leads to a much higher $T_d \approx 585$ K, and other reactions are even less favorable. Note that reaction (3.5) is the least favorable of all reactions, which implies that from a thermodynamic perspective B_2H_6 gas should not be formed.

Large Clusters

So far, we have considered the decomposition of $(\mathrm{LiBH_4})_n$ with $n \leq 12$ by explicit calculations on these small clusters. In this subsection we employ a simple model to obtain the energies of larger clusters. Using calculated surface energies and the Wulff theorem,[115] we model the equilibrium shape of large nanoclusters.[d] This method has been used previously to predict the shape and energetics of hydride nanoclusters.[113,149]

---

[b] We calculate the zero-point vibrational energies and the temperature dependent vibrational enthalpies and entropies of bulk crystal structures and of $\mathrm{Li_2B_nH_n}$ ($n = 4, 12$), $(\mathrm{LiBH_4})_{12}$ and $(\mathrm{LiB})_{12}$ clusters, explicitly. For Li_n, $(\mathrm{LiH})_n$ and B_n clusters with $n = 4$ and 12, the corresponding bulk values per f.u. are used. The calculated values for $(\mathrm{LiB})_{12}$ and $(\mathrm{LiBH_4})_{12}$ clusters per f.u. are used for $(\mathrm{LiB})_4$ and $(\mathrm{LiBH_4})_4$, respectively.

[c] The free energy is calculated as the sum of the total energy, ZPE and experimental data from the NIST-JANAF Thermochemical Tables[148].

[d] The wulffman program was used: http://www.ctcms.nist.gov/wulffman/index.html

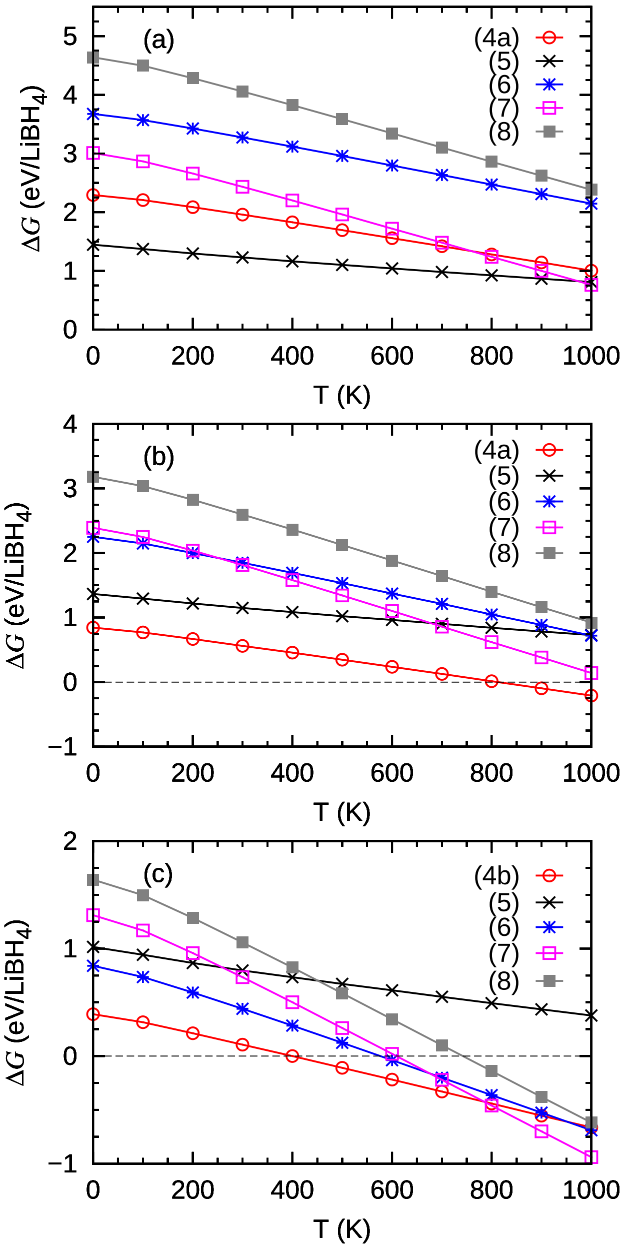

Figure 3.7: $\Delta G/LiBH_4$ f.u. as a function of temperature for reactions (3.4a/3.4b)-(3.8), for $n = 4$ (a), $n = 12$ (b), and bulk (c).

Once the shape of a nanocluster is determined, we calculate its total energy by

$$E_{\text{cluster}}(n) = nE_{\text{bulk}} + \sum_i \gamma_i A_i, \tag{3.10}$$

where γ_i is the surface energy of the ith nanocluster face, and A_i is the area of the corresponding face. E_{bulk} is the bulk total energy per f.u..

Using Eq. (3.10) with the bulk total energy and the surface energies given in Tables 3.1 and 3.2 respectively, we get −24.02 eV/f.u. for the $(LiBH_4)_{56}$ cluster.

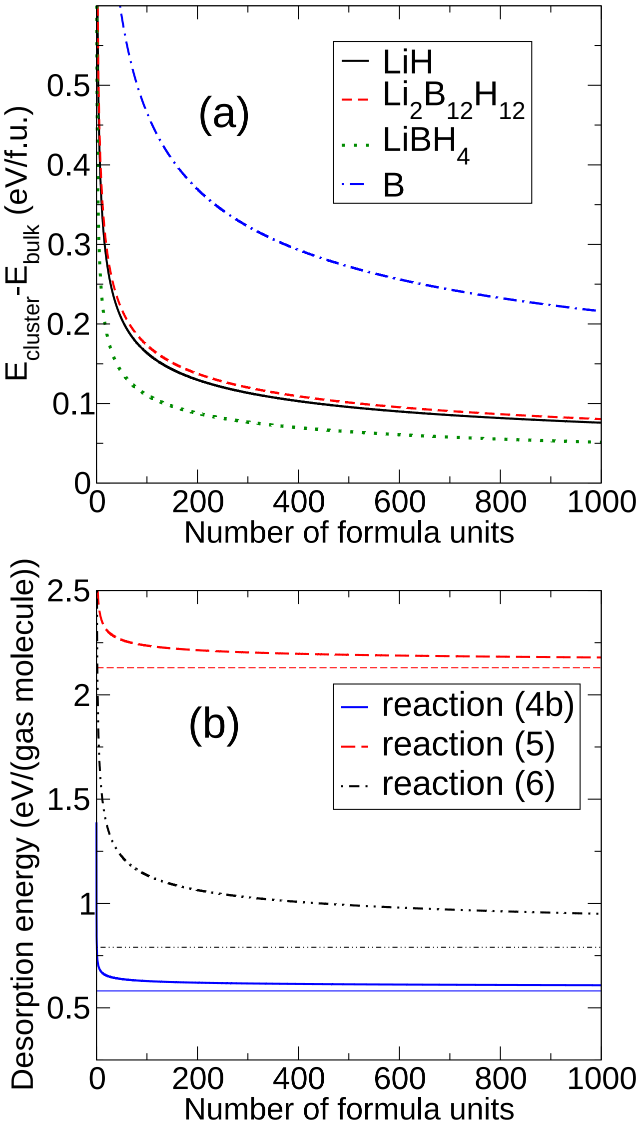

Figure 3.8: The energy difference per f.u. between the nanocluster and the corresponding bulk material (a). Calculated desorption energies for reactions (3.4b), (3.5) and (3.6) (b). Both as a function of the number of f.u..

This is quite close to the value −24.03 eV/f.u. reported in Table 3.1, which has been obtained by direct optimization of the cluster with DFT. It suggests that the Wulff construction is sufficiently accurate for larger clusters. Furthermore, Table 3.1 suggests that clusters of an intermediate size, $12 < n < 56$, have similar energetics.

Bulk $Li_2B_{12}H_{12}$ and LiH have cubic structures.[130,133] In both cases the (001) surfaces have the lowest energy, with calculated $\gamma_{001} = 0.059$ and 0.319 J/m^2 for $Li_2B_{12}H_{12}$ and LiH, respectively. Crystallites of these materials then have a cubic shape. The shapes of the boron nanoclusters are predicted from the DFT surface energies calculated in Ref. 150. We do not consider large LiB clusters because the experimental structure of Ref. 131 gives a hydrogen desorption energy for the bulk reaction (3.7) that is considerably higher than for bulk reaction (3.6), see Figure 3.6 and Figure 3.7(c). Note that recent experimental and theoretical studies[141,151] suggest a boron deficient phase LiB_x (x = 0.8-1.0) for lithium monoboride. As reaction (3.8) gives an even higher desorption energy, we also do not consider large Li clusters.

Cluster energies as a function of the number of formula units n, calculated according to Eq. (3.10), are given in Figure 3.8(a). The stability of a cluster increases with its size, as one may expect. This is also true for the small clusters, Figure 3.4, but note that the energy scale for large clusters is an order of magnitude smaller. Yet the relative stability of clusters of the different compounds is the same for small and for large clusters. $LiBH_4$ nanoclusters are relatively stable with respect to bulk, $Li_2B_{12}H_{12}$ and LiH clusters are somewhat less stable, and B clusters are relatively unstable.

In Figure 3.8(b) we plot the desorption energies for several desorption pathways of reactions (3.4b), (3.5) and (3.6). As $Li_2B_{12}H_{12}$ is a stable phase, we switch from reaction (3.4a) to (3.4b) for larger clusters. The desorption energies of reactions (3.4b) and (3.5) rapidly converge with the number of formula units. Reactions (3.4b) and (3.5) have desorption energies that are within 0.1 eV per gas molecule of their respective bulk values for cluster sizes $n \geq 100$ and $n \geq 240$, respectively. Note that the desorption energy for reaction (3.6) converges much more slowly to the bulk value as a function of the cluster size. This is due to the relatively high energy of B nanoclusters, see Figure 3.8(a). One needs clusters as large as 5000 f.u. to decrease the desorption energy of this reaction to within 0.1 eV/H_2 of the bulk limit.

So far we have considered reaction scenarios where each cluster decomposes independently of all other clusters. Such a scenario would hold for a nanostructured material, where no mass exchange between the nanoclusters takes place. Nanostructuring typically proceeds by embedding the reactive compound in the pores of an unreactive nanostructured template material. These pores are connected, so in principle mass transport between the pores can take place if the mobility of the reaction products is sufficiently high.

In a simple model exploring the possibility of mass transport we assume that the pores are spherical and of a fixed size, and neglect any chemical interaction between the reaction clusters and the template material. As for all compounds large clusters are energetically more favorable, the most favorable situation is then filling each pore with a single compound. The cluster energies as a function of pore size are presented in Figure 3.9(a). Here we assume that a spherical pore is filled with the largest crystallite of a material that fits, with the crystallite shape determined by the Wulff construction. The most striking difference with Figure 3.8(a) is the $Li_2B_{12}H_{12}$ curve. If the stability is determined by volume, then $Li_2B_{12}H_{12}$ clusters are relatively unstable, as a fixed volume contains much fewer formula units than in any of the other compounds.

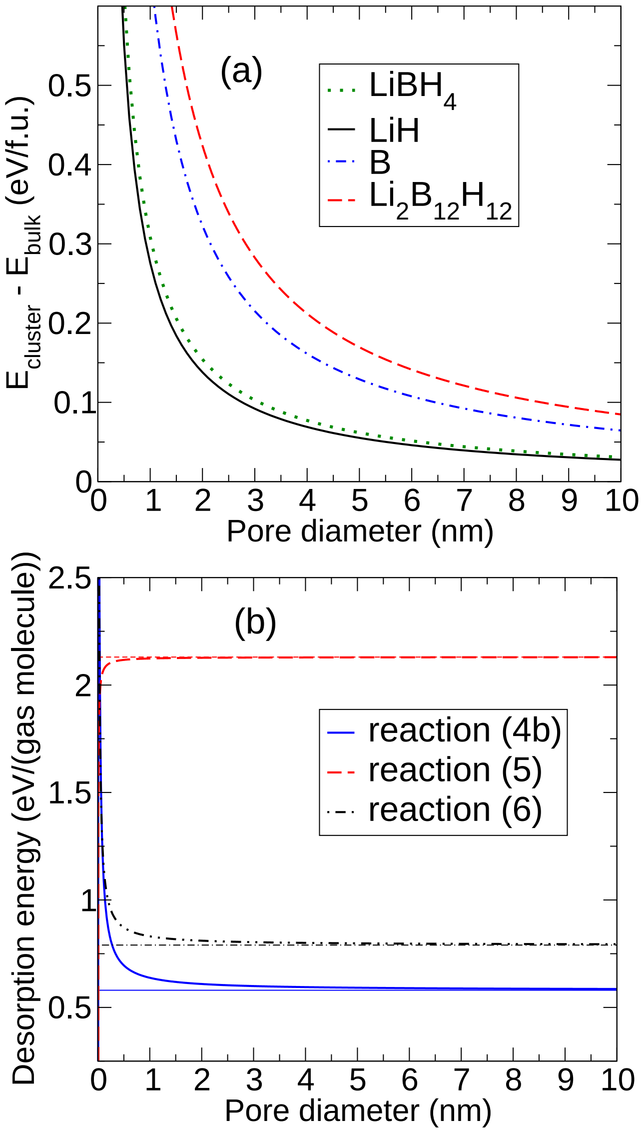

Figure 3.9: The energy difference per f.u. between the nanocluster and the corresponding bulk material (a). Calculated desorption energies for reactions (3.4b), (3.5) and (3.6) (b). Both as a function of the pore diameter.

The desorption energies of reactions (3.4b), (3.5) and (3.6) according to this scenario are plotted in Figure 3.9(b). Before the reaction all pores are filled with $LiBH_4$. After the reaction we assume that each pore is filled with either a $Li_2B_{12}H_{12}$ cluster, a LiH cluster, or a B cluster. It means that during a reaction material moves between the pores such that the end situation is a completely phase separated state. It leaves each pore filled with one material, and a fraction of the pores empty.

For the dehydrogenation reactions (3.4b) and (3.6), this scenario gives a desorption energy that is very close to the bulk value for most pore sizes. Indeed, one needs a pore diameter smaller than 0.43 nm respectively 0.57 nm to destabilize reactions (3.6) and (3.4b) by 0.1 eV/H_2. Of course for such small clusters the Wulff construction is not sufficiently accurate, and one should follow the approach used in the previous subsection. Compared to Figure 3.8(b), the desorption energy of reaction (3.6) is decreased. Mass exchange allows for the formation of larger B clusters, which are relatively more stable. For reaction (3.4b) mass exchange has relatively little effect on the desorption energy.

Reaction (3.5) involves desorption of B_2H_6. The desorption energy converges very rapidly to the bulk value with increasing pore size. Only for very small pores with a diameter $\leq$ 0.5 nm does this reaction become more favorable. This reaction is thermodynamically not favorable for the bulk material, compared to the hydrogen desorption reactions 3.4b) and (3.6), and only for tiny cluster sizes does reaction (3.5) become competitive, see Figure 3.7.

3.4 Discussion and Conclusions

The effects of nanoconfinement on desorption properties of $LiBH_4$ have been investigated intensively in the past few years, aiming for favorably altering the thermodynamics, de/rehydrogenation kinetics and cycling capacity of this material.[34–45] The experimental results for $LiBH_4$ incorporated into porous scaffolds can be summarized as follows. First, the rate of dehydrogenation increases with decreasing pore size.[35,37,45,152] Second, the hydrogen pressure at 300 °C is ten times higher for $LiBH_4$ incorporated into 13 nm graphitic aerogel, as compared to $LiBH_4$ mixed with non-porous graphite.[35] Likewise, compared to the latter the apparent hydrogen desorption temperature of $LiBH_4$ inserted into nanoporous carbon decreases by $\sim$ 100 °C.[45] Third, $LiBH_4$ embedded in pores smaller than 4 nm results in a significant reduction of the emission of B_2H_6 gas.[41,42] Finally, partial rehydrogenation of the end products back to $LiBH_4$ can be achieved, which is not possible for the reaction in bulk.[45]

These findings can be the result of changed kinetics, as obviously nanoconfinement puts a limit on the particle size, which will reduce the diffusion distance required for mass transport. Alternatively, the thermodynamics of the reactions might be altered, as nanoclusters are less stable than bulk materials. In this work, we have addressed the latter issue by studying the stability of $LiBH_4$ nanoclusters, as function of their size, as well as the stability of nanoclusters of possible decomposition products, Li, LiH, LiB, B and $Li_2B_nH_n$. We use DFT calculations to predict the geometry and energetics of small clusters. DFT bulk and surface energies in combination with the Wulff theorem are used to model the equilibrium shapes of larger clusters, and obtain their total energies.

From a thermodynamic point of view, the possible reactions of $LiBH_4$ nanoclusters with a diameter larger than $\sim$ 2 nm are indistinguishable from that of bulk $LiBH_4$. It means that the desorption reaction to $Li_2B_{12}H_{12}$, Eq. (3.1), is most favorable. The direct reaction to LiH and B, Eq. (3.2), is less favorable, and reactions to B_2H_6, LiB, or Li, are unfavorable.

Only for clusters that have a diameter less than $\sim$ 1 nm, i.e. $(LiBH_4)_n$, $n < 12$, is the thermodynamics significantly different from that of the bulk. However, the thermodynamics of these small clusters is unfavorable, as it leads to *higher* hydrogen desorption temperatures compared to the bulk. The reason is that, although $(LiBH_4)_n$ clusters are destabilized with respect to bulk, clusters of possible products $(LiH)_n$, $(LiB)_n$, $(Li)_n$, or $(B)_n$ of reactions (3.6)-(3.8), are even more destabilized. The dehydrogenation reaction to $Li_2B_nH_n$, Eq. (3.4a), remains the most favorable for $n \geq 6$. Only for extremely small cluster size does the decomposition to B_2H_6, Eq. (3.5), become competitive. These results are in line with the results of the theoretical calculations on small $(NaAlH_4)_n$ clusters with $n \leq 8$.[33] The stability of $(NaAlH_4)_n$ clusters increases with decreasing the cluster size.

Our findings show that the improved (de)hydrogenation effects of nanoconfined $LiBH_4$ observed in experiment can not be caused by changes in the thermodynamics of $LiBH_4$ clusters. Such effects can have a kinetic origin. Alternatively, they are caused by a chemical interaction between the reaction products and the template material. Reactions between the decomposition products of $LiBH_4$ and porous SiO_2 have been demonstrated,[38] but similar interactions with porous carbon are unlikely. The interaction between Li and carbon materials is weak, for instance, unless such a material contains unsaturated bonds.[127,153] A dehydrogenation reaction to $Li_2B_{12}H_{12}$, Eq. (3.1), is consistent with the increased hydrogen pressure and the dehydrogenation temperature observed in experiment.[35,37,45]

Our results also suggest that the emission of diborane in the decomposition of bulk $LiBH_4$ is a kinetic effect, as this reaction is thermodynamically unfavorable. It could be kinetically favored in a bulk borohydride material. Mass transport in a crystalline borohydride material can proceed via intrinsic defects that lead in a natural way to a reaction at the surface in which borane is released.[154] The formation of crystalline $Li_2B_{12}H_{12}$, however, may require a more complicated mass transport involving large kinetic barriers. Nanostructuring $LiBH_4$ could decrease these barriers, which would make the reaction leading to the emission of diborane less probable.[41,42]

acknowledgements

The authors thank Petra de Jongh and Peter Ngene for useful discussions on the topic of this paper and Gerrit Groenenboom for valuable technical advice. The work of E.H. is part of the “Sustainable Hydrogen” program of Advanced Chemical Technologies for Sustainability (ACTS), project no. 053.61.019. The work of G.A.d.W. is part of the

“Stichting voor Fundamenteel Onderzoek der Materie (FOM)” with financial support from the “Nederlandse Organisatie voor Wetenschappelijk Onderzoek (NWO)”.

Chapter 4

Carbon support effects on confined $LiBH_4$ nanoparticles: A first-principles study

Abstract

Recent experimental studies suggest that $LiBH_4$ nanoparticles confined in different types of nanoporous carbon materials show faster desorption kinetics, improved reversibility, and more favorable thermodynamics, as compared to bulk. Using density functional theory calculations, we study how the thermodynamics of the decomposition reactions of $LiBH_4$ nanoparticles is affected by the chemical interactions between the reactant and products, and the nanoporous carbon host. We find that the reversible intercalation of Li as one of the reaction products into the graphitic carbon host has a large effect on the reaction enthalpies of small clusters. Explicit calculations show that small $(LiBH_4)_n$, $n \lesssim 12$, clusters decompose at much lower temperatures in the presence of graphite, leading to the formation of intercalated Li. This route becomes unfavorable for larger $(LiBH_4)_n$ clusters, where dehydrogenation leads to the formation of $(LiH)_n$ clusters.

4.1 Introduction

Storage of hydrogen in high gravimetric and volumetric densities at ambient temperature and moderate pressure is a bottleneck for realizing hydrogen energy systems in the near future. An ideal storage system should have large gravimetric and volumetric storage capacity, suitable thermodynamic properties, and fast hydrogen absorption and desorption kinetics.[112] Complex hydrides are of great interest for this purpose.[155] A gravimetric capacity of 18.5 wt% makes $LiBH_4$ one of the most interesting complex hydrides for hydrogen storage.[6,7,20–23] However, $LiBH_4$ is a relatively stable material that decomposes at a high temperature $\gtrsim 400$ °C. Furthermore, rehydrogenation is only possible at extreme conditions with typical values for temperature and pressure of 600 °C and 350 bar H_2. In addition, de/rehydrogenation kinetics is slow, which is a common problem for the bulk complex hydrides.[6,24–26]

A recently adopted approach that helps to address such problems, is nanoconfinement in porous materials.[27–29] For instance, experimental and theoretical studies show that nanoconfinement of $NaAlH_4$ in porous carbon improves the H_2 sorption kinetics and that, somewhat surprisingly, nanoconfinement also alters the decomposition thermodynamics.[30–33] This approach can also be applied to $LiBH_4$. Indeed, improving its sorption properties *via* nanoconfinement in porous materials has become the focus of much experimental work.[34–45] Faster dehydrogenation kinetics has been reported for $LiBH_4$ infiltrated in carbon aerogels, nanoporous carbon, and nanoporous silica, accompanied by a decrease of the dehydrogenation temperature by at least 100 °C. In addition, confinement of $LiBH_4$ in nanoporous carbon leads to a marked improvement of the reversibility of the hydrogen desorption.

These findings could be the result of changed kinetics, as obviously nanoconfinement puts a limit on the particle size, which will reduce the diffusion distance required for mass transport.[154,156] Moreover, both the size of the clusters and their interactions with the host may modify the thermodynamics of the reactions.

In a previous work, we studied the stability of $(LiBH_4)_n$ nanoclusters, as a function of their size, as well as the stability of a range of possible nanocluster decomposition products.[157] Our findings suggest that, from a thermodynamic point of view, the desorption reactions of unsupported $LiBH_4$ nanoclusters with a diameter larger than ~ 2 nm are indistinguishable from those of bulk $LiBH_4$ [i.e. decomposition to $Li_2B_{12}H_{12}$, followed by a second decomposition step to LiH and B]. Only for clusters that have a diameter less than $\sim$ 1 nm, i.e. $(LiBH_4)_n$, $n < 12$, is the thermodynamics of the decomposition reaction significantly different. The thermodynamics of small clusters is, however, unfavorable, and leads to *higher* hydrogen desorption temperatures compared to the bulk. The reason is that, although $(LiBH_4)_n$ clusters are destabilized with respect to bulk, clusters of possible reaction products are even more destabilized. Concluding, our findings have shown that the improved (de)hydrogenation of nano-confined $LiBH_4$ observed in experiment cannot be caused by changes in the thermodynamics of the $LiBH_4$ nanoclusters. Such effects could have a kinetic origin, or could be due to a chemical interaction between the reactant or products and the host material.

Indeed, such chemical interactions have been observed, in, for instance, NaH. A recent experiment has shown that the improved thermodynamic properties of NaH nanoparticles, compared to bulk NaH, are partly due to the close contact with the nanoporous carbon host.[158] In this study an increase in the average graphene interlayer spacing distance from 3.35 Å to 3.54 Å has demonstrated intercalation of Na between the graphene layers.[159] Therefore, reversible intercalation of Na into the nanoporous carbon matrix stabilizes Na relative to its metallic phase, which will lower the dehydrogenation enthalpy.[158]

In the case of nano-confined $LiBH_4$, Li metal is potentially one of the reaction products during dehydrogenation. Intercalation of Li into graphite is well-known. This intercalation material can reversibly store Li to form Li-graphite systems with general formula Li_xC_6 ($0 \leq x \leq 1$). The intercalation/deintercalation process is highly reversible which makes graphitic carbon one of the most commonly used anodes in rechargeable Li-ion batteries.[160,161] If $LiBH_4$ is in close contact with the host nanoporous carbon, then during dehydrogenation of $LiBH_4$, Li might intercalate into the nanoporous carbon. Indeed, recent in situ X-ray Raman spectroscopy of $LiBH_4$ in porous carbon shows that part of the Li intercalates into the porous carbon during dehydrogenation.[46]

In this work we study how the thermodynamics of the decomposition reactions of $LiBH_4$ nanoparticles is affected by the chemical interactions between reactant and product particles with the nanoporous carbon host. We select graphite to represent the carbon host, which often consists of regular and/or non-regular stacks of graphene sheets (see Ref. 29). In particular we study the effect on the $LiBH_4$ decomposition reaction of intercalating Li in graphite as one of the reaction products. Indeed, as we will see below, this results in a different decomposition pathway for small clusters, where intercalated Li accounts an additional stabilization.[a]

This paper is organized as follows. In Sec. 4.2 we describe the computational procedures used. Secs. 4.3.1, 4.3.2 and 4.3.3 discuss the structures and the energetics of bulk graphite, a Li adatom at the graphene and graphite surfaces, and Li-graphite systems, respectively. In Sec. 4.3.4 we calculate the interaction energy between the reactant/products and graphene. These data are used in Secs. 4.3.5 and 4.3.5 to study the decomposition reactions of small and larger $(LiBH_4)_n$ nanoclusters

---

[a] By using graphite we assume that the number of unsaturated reactive carbon sites is small. Such sites might otherwise lead to special, (poly)lithiated species, see Ref. 162

respectively. Sec. 4.4 provides discussion and conclusions.

4.2 Computational Methods

First-principles calculations were performed in the framework of density functional theory (DFT)[48,49] using the PBE generalized gradient approximation (GGA)[50] and the projector augmented wave method (PAW)[51,52] as implemented in the Vienna *ab initio* simulation program (VASP).[53,54] Standard DFT fails to describe the non-local van der Waals (vdW) interactions. However, these interactions are important for graphite, where they account for most of the forces that bind the graphene layers together. In order to describe graphite and its Li intercalation compounds (and only those) we use the recently proposed van der Waals density functional (vdW-DF) of Dion et al.,[57] as implemented in VASP by J. Klimeš et al.[58] using the efficient algorithm of Roman-Perez and Soler.[59]

In vdW-DF method, the exchange-correlation energy takes the form

$$E_{\mathrm{xc}} = E_{\mathrm{x}} + E_{\mathrm{c}} = E_{\mathrm{x}} + [E_{\mathrm{c}}(\mathrm{vdW}) + E_{\mathrm{c}}(\mathrm{rest})] \tag{4.1}$$

where the $E_{\mathrm{c}}(\mathrm{vdW})$ is the energy due to the non-local electron-electron correlations. In the original vdW-DF method of Dion et al., the revPBE functional (Ref. 163) is used to calculate the exchange energy E_{x}. $E_{\mathrm{c}}(\mathrm{rest})$ is calculated within the local density approximation (LDA). We also tried the second version of the van der Waals density functional (vdW-DF2) proposed by Lee et al.,[164] which uses the PW86 exchange functional,[165] along with a modified vdW kernel. Both the original vdW-DF and the vdW-DF2 functionals overestimate the lattice constants and underestimate the formation energies of solids somewhat.[58] The optimized exchange functionals introduced in Refs. 166 and 58, i.e. optB88, optPBE and optB86b, alleviate these problems to a large extent.

For H and Li all-electron PAW data sets were used whereas for B and C the 1s core state was kept frozen. A kinetic energy cutoff of 550 eV was employed for the plane wave expansion of the Kohn-Sham orbitals. The energies of nanoclusters were calculated in a periodically repeated cubic box which included at least 12 Å of vacuum in each direction to separate the periodic images. The energies of isolated H_2 and B_2H_6 molecules were calculated in cubic boxes with sizes of 12 Å and 14 Å, respectively. The internal atomic positions were optimized with the conjugate gradient method until the forces on atoms were less than 0.01 eV/Å. This is sufficient to obtain converged total energies. The ground state geometries of the small clusters are described in detail in Ref. 157.

In the case of *AB* stacked graphite, a Γ-centered 24×24×10 k-point mesh is used. In this case, the energy convergence with respect to the k-point sampling is better than

1 meV/C. We used the same k-point density for the rest of the calculations, except for the isolated nanoclusters for which only the Γ point is used. The Methfessel-Paxton (MP) scheme[167] with a smearing width of 0.2 eV is employed for the occupation of the electronic levels.

For the two basic dehydrogenation reactions of $LiBH_4$, i.e. to $Li_2B_{12}H_{12}$ and LiH, and to B and LiH (see reactions (4.7) and (4.8) below), we obtain an energy of 0.39 eV/$LiBH_4$ and 0.84 eV/$LiBH_4$, respectively (at $T = 0$ K, including zero-point energies). The calculated formation energy of $LiBH_4$ with respect to the Li and B crystals is 1.64 eV/$LiBH_4$. These numbers are in good agreement with calculated values reported in the literature.[144–146,155]

Lattice vibrational frequencies were calculated for some of the isolated clusters[b] using the finite difference methods of Ref. 119. We calculate $G(T)$ of the clusters (in Section 4.3.5) from the DFT total energies and the vibrational densities of states,[122] where we assume that the clusters are immobilized by confinement in a porous material (so we neglect contributions to the free energy due to translational and rotational degrees of freedom). Here, we neglect changes in the Li phonon modes upon intercalation into graphite and use the vibrational densities of state of free-standing clusters. The free energies of H_2 gas and B_2H_6 gas are taken from the literature, using a gas pressure of 1 bar.[c]

4.3 Results

4.3.1 Bulk graphite

First we study bulk graphite with different van der Waals density functionals, and select the most appropriate one for our intercalation study. We calculate the equilibrium lattice constant a, interlayer distance d and interlayer binding energy E_B of graphite. E_B is obtained by subtracting the graphite total energy at its equilibrium interlayer distance d from the graphite total energy at very large interlayer distances, i.e. the limit of uncoupled graphene layers.

Table 4.1 shows the calculated properties of graphite using different types of exchange and correlation functionals. All exchange and correlation functionals obtain a lattice constant a very close to the experimental value. The graphite interlayer distance d, however, is considerably overestimated by plain PBE without vdW forces

---

[b] We calculate the zero-point vibrational energies and the temperature dependent vibrational enthalpies and entropies of $Li_2B_nH_n$ ($n = 4, 12$), $(LiBH_4)_{12}$ and $(LiB)_{12}$ clusters, explicitly. For Li_n, $(LiH)_n$ and B_n clusters with $n = 4$ and 12, the corresponding bulk values per f.u. are used. The calculated values for $(LiB)_{12}$ and $(LiBH_4)_{12}$ clusters per f.u. are used for $(LiB)_4$ and $(LiBH_4)_4$, respectively.

[c] The free energy is calculated as the sum of the total energy, ZPE and experimental data from the NIST-JANAF Thermochemical Tables.[148]

Table 4.1: The equilibrium lattice constant a, interlayer distance d and interlayer binding energy E_B of graphite calculated using different types of exchange and correlation functionals compared to experiment (EXP) and quantum Monte Carlo (QMC).

Exchange	PBE	PBE	optB88	optPBE	optB86b	revPBE	PW86R	QMC[a]	EXP
Correlation	0+PBE	vdW+LDA	vdW+LDA	vdW+LDA	vdW+LDA	vdW+LDA	vdW2+LDA		
a(Å)	2.47	2.47	2.47	2.48	2.47	2.48	2.48		2.46[b]
d(Å)	4.40	3.44	3.36	3.44	3.31	3.59	3.51	3.43	3.34[b]
E_B(meV/C)	1.0	70.8	69.5	63.7	69.9	52.7	52.0	56±5	52±5[c]

[a] Ref. 168

[b] Ref. 169

[c] Ref. 170

(PBE-PBE): 4.40 Å vs. 3.34 Å. Indeed, the lack of non-local correlation is also apparent in a near absence of interlayer binding ($E_B = 1.0$ meV/C). By including the vdW interactions both the interlayer distance and binding energy are reasonably well reproduced. The choice of a specific exchange and correlation functional matters, but not to a large extent. Using the optB88-vdW and optB86b-vdW functionals, the optimized interlayer distances are 3.36 and 3.31 Å, respectively, which are very close to the experimental value (3.34 Å). The PBE-vdW, optPBE-vdW, revPBE-vdW and PW86R-vdW2 functionals predict somewhat larger interlayer distances, i.e. 3.44, 3.44, 3.59 and 3.51 Å respectively. Comparing binding energies, we see that the revPBE-vdW and PW86R-vdW2 functionals have the best performance. The other functionals (PBE-vdW, optB88-vdW, optPBE-vdW and optB86b-vdW) overestimate the experimental binding energy by 21 to 24 %. Comparison to a binding energy obtained from quantum Monte Carlo calculations (QMC),[168] yields essentially the same picture. Our calculated revPBE-vdW and PW86R-vdW2 values for interlayer distance and binding energy are in good agreement with previous results.[171,172]

Below we use the optB88-vdW functional, wherever we want to include the vdW interactions. This gives good interlayer distance for graphite. Moreover, as we will see in section 4.3.3, the optB88-vdW functional successfully predicts the c lattice parameter of the Li-graphite systems (where standard DFT also fails). This functional performs somewhat less well for E_B, so for a few Li-graphite systems we have checked the sensitivity to the functional by also carrying out a few PW86R-vdW2 calculations. This functional performs very well for the graphite interlayer binding energy.

Using the optB88-vdW functional, in agreement with experiment, AB-stacked graphite is more stable than AA-stacked by 10.5 meV/C.[173,174]

4.3.2 Li and B adatoms on single layer graphene and on graphite

In this section we briefly discuss the stability of a single Li adatom and a single B adatom on single-layer graphene and on graphite. We use the optB88-vdW or the PBE-PBE functional, depending on whether vdW interactions are included.

First we establish how thick a slab is needed to approximate a graphite surface. This is done by calculating the energy required for removing a single graphene layer from a multilayer graphite slab. We obtain 65.3, 69.0, 69.9, 69.8 and 70.0 meV/C for two, three, four, five and six layers thick slabs, respectively. This shows that three layers of graphene is enough to represent the graphite surface.

The adatom adsorption energy to the surface is

$$E_{\mathrm{ads}} = E_{\mathrm{adgr}} - E_{\mathrm{gr}} - E_{\mathrm{adbulk}} \tag{4.2}$$

Here E_{adgr} is the total energy of the system with the adatom, E_{adbulk} is the total energy (per atom) of the adatom bulk material, and E_{gr} is the total energy of the system without adatom. Table 4.2 shows the adsorption energies of Li and B adatoms calculated at three different high symmetry sites, i.e. the bridge (B), the hollow (H) and the top (T) site. We calculate the adsorption energy of Li (B) at three (two) different concentrations, and for various slab thicknesses p (only for Li).

Most of the calculated adsorption energies are positive, i.e. the adatom on graphene/graphite is unstable with regard to separation into graphene/graphite and bulk Li (B).

For Li, the most stable adsorption position is the hollow site, which is in agreement with previous studies.[175–178] For B, the bridge site is slightly more stable than the hollow and top sites, which is also in agreement with previous calculations.[179] The van der Waals contribution to the binding energy of single Li and B atoms is moderate, i.e. $\lesssim 0.1$ eV.

The results in Table 4.2 again confirm that 3 layers are sufficient to represent a graphite surface: In the 4×4 surface cell, the H-site adsorption energies are practically identical for the 3, 4, 5, and 6 layers thick slabs.

Table 4.2 also shows that the Li adsorption energy decreases (becomes more stable) as its concentration decreases. In the dilute limit of $p = 3$ and an 8×8 surface supercell it even becomes negative. The dependence of the adsorption energy on the packing density of Li atoms and the number of graphene layers, likely has an electrostatic origin. Li atoms at the surface carry an effective positive charge, as they have donated a substantial amount of electronic charge to the substrate.[178] The positive charges are then screened by compensating negative charges in graphite, in the vicinity of the Li atoms. Obviously the screening in graphite is better than in graphene (and the better the screening, the lower the energy). The interaction between the Li atoms at the surface then corresponds to a Coulomb repulsion between effective

Table 4.2: The adsorption energy E_{ads} of Li and B adatoms calculated at three different high symmetric sites, i.e. B: bridge, H: hollow and T: top. p is the number of graphene layers stacked in the Bernal structure (AB sequence). $m \times n$ shows the number of graphene unit cells used in the supercell model, e.g. 4×4 supercell contains 32 carbon atoms per layer. In the case of the single graphene layer, two calculations are performed for the optB88-vdW and the PBE-PBE functional. E_{ads}^{atom} is the adsorption energy with respect to isolated atom.

Li adatom			E_{ads} (eV)			E_{ads}^{atom} (eV)
p	$m \times n$	vdW	B-site	H-site	T-site	H-site
1	4×4	no	+0.809	+0.452	+0.823	−1.156
1	4×4	yes	+0.652	+0.355	+0.667	−1.223
2	4×4	yes		+0.265		−1.313
3	4×4	yes		+0.240		−1.338
4	4×4	yes		+0.238		−1.340
5	4×4	yes		+0.233		−1.345
6	4×4	yes		+0.235		−1.343
1	6×6	no		+0.329		−1.279
1	6×6	yes		+0.232		−1.346
2	6×6	yes		+0.137		−1.441
3	6×6	yes		+0.091		−1.487
1	8×8	no	+0.577	+0.270	+0.600	−1.338
1	8×8	yes	+0.434	+0.163	+0.454	−1.415
2	8×8	yes		+0.064		−1.514
3	8×8	yes		−0.038		−1.616

B adatom			E_{ads} (eV)			E_{ads}^{atom} (eV)
p	$m \times n$	vdW	B-site	H-site	T-site	B-site
1	4×4	no	+5.431	+5.577	+5.478	−0.997
1	4×4	yes	+5.368	+5.595	+5.386	−1.060
1	8×8	no	+5.396			−1.032
1	8×8	yes	+5.335			−1.093

dipoles (formed by the charges on the Li atoms, and the screening charges in the substrate).

4.3.3 Li-graphite systems

As already mentioned in the introduction, Li metal is potentially one of the reaction products during dehydrogenation of $LiBH_4$. If $LiBH_4$ is in close contact with nanoporous carbon, then, during the dehydrogenation of $LiBH_4$, Li can intercalate into the host nanoporous carbon. Therefore, in this section we study in detail the Li-graphite intercalation systems. Graphite can reversibly store Li to form Li-graphite systems with general formula Li_xC_6 with $0 \leq x \leq 1$.[180–182] For $x = 1.0$, LiC_6, all the graphitic layers are separated by a Li layer. It is called stage I. Stage II occurs for $x = 0.5$, $Li_{0.5}C_6$. Each Li layer is now separated from its neighboring Li layer by two graphitic layers. So, for stage m there are m layers between two neighboring Li layers. Different stages occur as a function of Li content.

The calculated structural and energetic properties of different phases of Li-graphite compounds are listed in Table 4.3. The formation energy E_{form} of an intermediate phase Li_xC_6 is calculated relative to C_6 and LiC_6 as

$$E_{\mathrm{form}}(\mathrm{Li}_x\mathrm{C}_6) = E(\mathrm{Li}_x\mathrm{C}_6) - [(1-x)E(\mathrm{C}_6) + xE(\mathrm{LiC}_6)] \tag{4.3}$$

The intercalation energy E_{interc} is defined as

$$E_{\mathrm{interc}}(\mathrm{Li}_n\mathrm{C}_m) = E(\mathrm{Li}_n\mathrm{C}_m) - nE(\mathrm{Li}_{\mathrm{metal}}) - \frac{m}{4}E(\mathrm{graphite}) \tag{4.4}$$

Here n and m denote the number of Li and C atoms in the Li_xC_6 phase, respectively, and E(graphite) is the total energy of one unit cell of graphite. Alternatively, the intercalation energy may be referenced to the Li atom:

$$E^{\mathrm{atom}}_{\mathrm{interc}}(\mathrm{Li}_n\mathrm{C}_m) = E(\mathrm{Li}_n\mathrm{C}_m) - nE(\mathrm{Li}[^2S_{1/2}]) - \frac{m}{4}E(\mathrm{graphite}) \tag{4.5}$$

We start with the fully lithiated system LiC_6. The calculated interlayer distance is 3.64 Å, which is very close to the experimental value of 3.70 Å.[183] For $Li_{0.5}C_6$ we considered both A-Li-A-A-Li-A and A-Li-A-B-Li-B structures, and found that, in agreement with experiment,[184] the former is favored over the latter, by 13 meV/6C. For $Li_{0.5}C_6$ the average interlayer distance is 3.49 Å (experiment: $\sim$ 3.51 Å),[183,184] whereas the distance between the empty graphite layers is 3.27 Å (experiment: 3.25 Å).[184] Evidently the optB88-vdW functional accurately reproduces the interlayer distance of Li-graphite systems. In Sec. 4.3.1 above we found that optB88-vdW is not optimal for the prediction of the graphite binding energy. Therefore, we recalculated the $Li_{0.5}C_6$ formation energy with the PW86R-vdW2 functional. That gives -29 meV/6C, i.e. very close to the -26 meV/6C obtained with optB88-vdW.

Table 4.3: The optimized interlayer distances for empty d_{empty} and lithiated d_{full} graphite layers and their average d_{ave}. The formation and intercalation energies are calculated according to Eqs. 4.3 and 4.4, respectively. The stable phases are marked with an asterisk (*). All data have been obtained with the optB88-vdW functional.

Compound	x	stage	d_{empty} (Å)	d_{full} (Å)	d_{ave} (Å)	E_{form} (meV/6C)	E_{interc} (eV/Li)	$E^{\text{atom}}_{\text{interc}}$ (eV/Li)
C_6^*	0		3.36		3.36	0	0	0
LiC_{48}	0.125	II	3.46	3.64	3.55	+17	−0.076	−1.654
Li_3C_{108}	0.167	II	3.49	3.65	3.57	+14	−0.146	−1.724
LiC_{36}	0.167	II	3.45	3.64	3.54	+11	−0.130	−1.708
LiC_{24}^*	0.250	II	3.43	3.69	3.56	−10	−0.260	−1.838
LiC_{18}	0.333	III	3.42	3.72	3.52	+15	−0.183	−1.761
Li_4C_{72}	0.333	II	3.34	3.72	3.53	−11	−0.251	−1.829
$Li_3C_{48}^*$	0.375	II	3.33	3.73	3.53	−23	−0.280	−1.858
LiC_{12}^*	0.500	II	3.27	3.71	3.49	−26	−0.270	−1.848
LiC_6^*	1.000	I		3.64	3.64	0	−0.217	−1.795

This gives confidence that the formation energies are independent of the specific functional used. In their study on Li_xC_6, Persson et al.[185] obtained −18.2 meV/6C for the $Li_{0.5}C_6$ formation energy. This is somewhat higher than our number, however, they have added an *ad hoc* vdW binding energy (20 meV/C) for every empty graphite layer to energies obtained with a plain PBE (PBE-PBE). This appears to be a reasonable approximation.

We have considered a few other stage II and stage III compounds Li_xC_6 with x ranging from 0.125 to 0.375 (see Table 4.3). Amongst them, the $Li_{0.25}C_6$, $Li_{0.333}C_6$ and $Li_{0.375}C_6$ phases have negative formation energies relative to C_6 and LiC_6.[d] Allthough the formation energy of $Li_{0.333}C_6$ is negative, it is metastable relative to $Li_{0.25}C_6$ and $Li_{0.375}C_6$. Based on the table, with increasing Li concentration, first a coexistence between pure graphite and $Li_{0.25}C_6$ occurs. When the latter average composition is exceeded, a coexistence region of $Li_{0.25}C_6$ and $Li_{0.375}C_6$ is entered, followed by coexistence of $Li_{0.375}C_6$ and $Li_{0.5}C_6$, and finally followed by coexistence of $Li_{0.5}C_6$ and LiC_6.

For the stable phases in Table 4.3, the calculated intercalation energies are in the range −0.2 to −0.3 eV/Li referenced to Li metal and C graphite (see Eq. 4.4). The

---

[d] The $Li_{0.375}C_6$ unit cell is four times the LiC_{12} unit cell, i.e. Li_4C_{48} with one Li atom removed. The $Li_{0.25}C_6$ unit cell is obtained by repeating the LiC_{12} unit cell in the *a* or *b* direction and then removing one Li.

measured enthalpies of formation for LiC_6 and LiC_{12} at 455 K referenced to liquid Li are -0.144 and -0.257 eV/Li, respectively.[186] Converting to solid Li as a reference state,[187] the measured enthalpies of formation for LiC_6 and LiC_{12} become -0.175 and -0.288 eV/Li, respectively. Our calculated values are -0.217 and -0.270 eV/Li for LiC_6 and LiC_{12}, respectively, i.e. we have good agreement with experiment.

4.3.4 $(\mathbf{Li})_n$, $(\mathbf{LiH})_n$, $(\mathbf{LiB})_n$, $(\mathbf{B})_n$, $(\mathbf{LiBH_4})_n$ and $\mathbf{Li_2B_nH_n}$ nanoclusters at the graphene surface

In this section we study the interaction of the reactant clusters $(LiBH_4)_n$ and several likely product clusters with the graphene surface. In order to avoid unwanted interactions between the periodic images, we repeat the graphene unit cell eight times in both *a* and *b* directions, i.e. an 8×8 hexagonal unit cell with an edge length of 19.74 Å and composition C_{128}. In the perpendicular *c* direction, the graphene layers are kept up to 20 Å apart from each other. The binding energy of the nano-cluster to the graphene surface is defined as

$$E_{\mathrm{b}}^{\mathrm{nc}} = E_{\mathrm{ncgr}} - E_{\mathrm{gr}} - E_{\mathrm{nc}} \tag{4.6}$$

where E_{ncgr} and E_{gr} are the total energies of the graphene supercell with and without the nanocluster at the surface, respectively. E_{nc} is the total energy of an isolated nanocluster. We will be mostly concerned with clusters with $n = 4$ and $n = 12$ f.u. as those will be used to calculate reaction enthalpies in Sec. 4.3.5. We use plain PBE (PBE-PBE).

For a single $LiBH_4$ unit, i.e. $n = 1$, on the graphene surface, the most stable configuration has Li above the center of the hexagon (see Fig. 4.1). The binding energy of -0.246 eV is rather small. The Li-B bond length increases by 0.04 Å in the presence of graphene. The calculated binding energy (using PW91 functional) of a single $NaAlH_4$ unit to graphene is even smaller, -0.093 eV.[188] For a single $LiBH_4$ on C_{60} the calculated binding energy (using PW91 functional) is -0.50 eV, where Li is centered above a C-C bridge.[189] So, a curvature of the graphene surface might lead to somewhat higher binding energies.

Larger $(LiBH_4)_n$ clusters, $(LiBH_4)_4$ and $(LiBH_4)_{12}$, hardly bind to the graphene surface, see Fig. 4.1. They have negligible binding energies of -0.033 and -0.005 eV, respectively.

The next step is to look at the interaction of the possible reaction products with a single graphene layer. We first consider $(LiH)_n$ nanoclusters with $n = 2$, 4, 10 and 12 (these are the possible decomposition products of $(LiBH_4)_4$ and $(LiBH_4)_{12}$ clusters). The calculated decomposition energies ΔE per Li atom of these small clusters are listed in Table 4.4. In Table 4.2 we showed that the adsorption energies

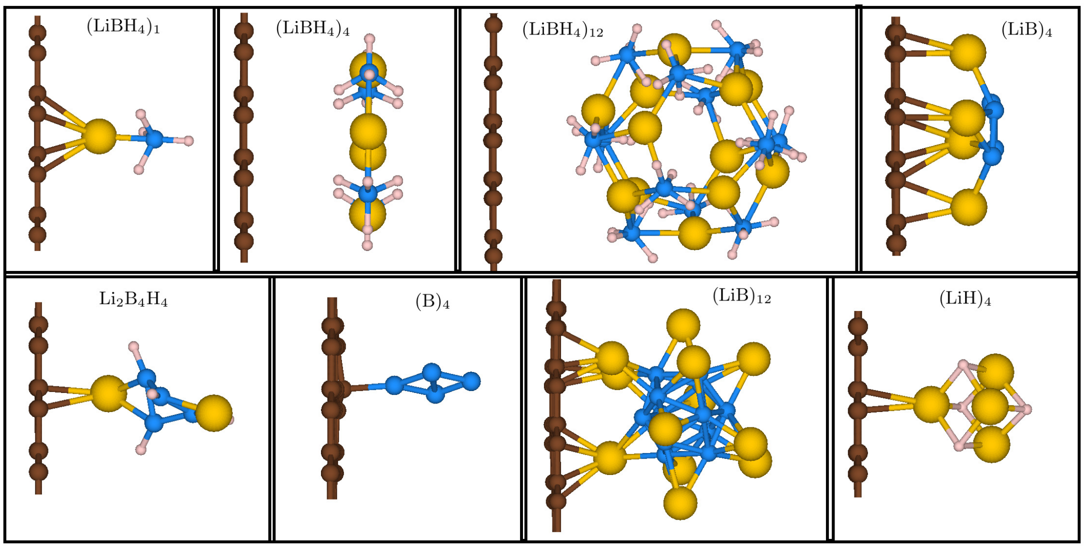

Figure 4.1: Optimized geometries of nanoclusters at the surface of a single graphene layer. Li: large yellow spheres, B: blue spheres, H small pink spheres, C brown spheres on left-hand-side.

Table 4.4: Calculated decomposition energies of $(LiH)_n$ nanoclusters (in vacuum) with n= 2, 4, 10 and 12.

Reaction			ΔE (eV/Li)
$(LiH)_2$	→	$2Li + H_2$	1.109
$(LiH)_4$	→	$4Li + 2H_2$	1.659
$(LiH)_{10}$	→	$10Li + 5H_2$	1.915
$(LiH)_{12}$	→	$12Li + 6H_2$	1.977

of Li adatom, relative to isolated atom, at the graphene and graphite surfaces are −1.338 and −1.616 eV, respectively. Comparing decomposition energies in Table 4.4 to the adsorption energies of Li adatom, we see that amongst the $(LiH)_n$ clusters in Table 4.4, the $(LiH)_2$ cluster is the only one that is not stable at the graphene surface. It decomposes into $2Li + H_2$. At the graphite surface $(LiH)_4$ is also unstable if the Li atoms that result from the decomposition into $4Li + 2H_2$ are allowed to intercalate into graphite.

The binding energies of the nanoclusters to a single graphene layer are summarized in Table 4.5. For the $(B)_4$ cluster, the most stable configuration has one boron on top of a carbon atom. The binding energy is −0.521 eV. The binding energy of $(B)_{12}$ is −0.058 eV, i.e. it hardly interacts with graphene. All of the Li atoms in $(LiB)_4$ and some of the Li atoms in $(LiB)_{12}$ clusters bind to graphene, see figure 4.1. The binding energies are −0.894 and −1.587 eV, respectively. Both the $Li_2B_4H_4$ and

Table 4.5: The binding energies E_b^{nc} of $(LiH)_n$, $(LiB)_n$, $(B)_n$, $(LiBH_4)_n$ and $Li_2B_nH_n$ nanoclusters to a single graphene layer: C_{128}. All data have been obtained with the PBE functional.

Nanocluster	E_b^{nc} (eV)	Nanocluster	E_b^{nc} (eV)
$(LiBH_4)_1$	−0.246	$(LiH)_4$	−0.089
$(LiBH_4)_4$	−0.033	$(LiH)_{10}$	−0.109
$(LiBH_4)_{12}$	−0.005	$(LiH)_{12}$	−0.110
$(B)_4$	−0.521	$(LiB)_4$	−0.894
$(B)_{12}$	−0.058	$(LiB)_{12}$	−1.587
$Li_2B_4H_4$	−0.248	$Li_2B_{12}H_{12}$	−0.220

the $Li_2B_{12}H_{12}$ clusters bind only *via* a Li atom to graphene, with binding energies of −0.248 and −0.220 eV, respectively. These energies are in the same range as the binding energy of the $(LiBH_4)_1$ cluster.

4.3.5 Decomposition of $(LiBH_4)_n$ clusters: interactions with graphite and graphene

The decomposition of bulk $LiBH_4$ takes place at a high temperature ($T > 400$ °C), and is proposed to proceed as[142,143]

$$\begin{aligned} LiBH_4 &\leftrightarrow \frac{1}{12}Li_2B_{12}H_{12} + \frac{5}{6}LiH + \frac{13}{12}H_2(g), && (4.7)\\ &\leftrightarrow LiH + B + \frac{3}{2}H_2(g). && (4.8) \end{aligned}$$

After the first step we have $Li_2B_{12}H_{12}$ as an intermediate. Recently it has been argued that the first step is actually different and gives diborane (B_2H_6) as intermediate according to:

$$LiBH_4 \leftrightarrow LiH + \frac{1}{2}B_2H_6(g). \tag{4.9}$$

Then, in a second step at $T > 250$ °C, the diborane decomposes to B and H_2.[147] It is proposed that $Li_2B_{12}H_{12}$, and an amorphous $Li_2B_{10}H_{10}$ phase, are formed only in a side-reaction between diborane and the un-reacted $LiBH_4$ at lower temperatures.

As discussed in the introduction, the improved (de)hydrogenation effects of nanoconfined $LiBH_4$ observed in experiment is unlikely to be caused by changes in the thermodynamics of $LiBH_4$ clusters themselves. Such effects could have a kinetic origin. Alternatively, they might result from a chemical interaction between the reaction products and the host (carbon) material. With the results from the previous sections, here we study how the host material affects the thermodynamics of the decomposition reactions. We start with a few small clusters, and extend the model to larger clusters later.

Small clusters

We select two clusters $(LiBH_4)_n$, $n = 4$ and $n = 12$. The latter can, among others, decompose into $Li_2B_{12}H_{12}$, which is the smallest cluster that contains a $(B_{12}H_{12})^{2-}$ ion. Such ions are the building blocks of bulk $Li_2B_{12}H_{12}$ [cf. (4.7) above]. Hence, $n = 12$ forms a natural demarcation between the small and the large clusters. We will treat the latter in the next subsection.

We consider the following possible decomposition reactions for $(LiBH_4)_n$ clusters

$$(LiBH_4)_n \leftrightarrow Li_2B_nH_n + (LiH)_{n-2} + (n+1)H_2(g), \tag{4.10}$$

$$(LiBH_4)_n \leftrightarrow Li_2B_nH_n + (Li)_{n-2} + \frac{3n}{2}H_2(g), \tag{4.11}$$

$$(LiBH_4)_n \leftrightarrow (LiH)_n + \frac{n}{2}B_2H_6(g), \tag{4.12}$$

$$(LiBH_4)_n \leftrightarrow (Li)_n + \frac{n}{2}B_2H_6(g) + \frac{n}{2}H_2(g), \tag{4.13}$$

$$(LiBH_4)_n \leftrightarrow (LiH)_n + (B)_n + \frac{3n}{2}H_2(g), \tag{4.14}$$

$$(LiBH_4)_n \leftrightarrow (LiB)_n + 2n\,H_2(g), \tag{4.15}$$

$$(LiBH_4)_n \leftrightarrow (Li)_n + (B)_n + 2n\,H_2(g). \tag{4.16}$$

Note that (4.10) and (4.11) are specific for $n \leq 12$, where a $(B_{12}H_{12})^{2-}$ cannot occur. Reaction (4.10) is the small-cluster replacement of (4.7).

Reversible Li intercalation into the graphitic carbon support during dehydrogenation of nano-confined $LiBH_4$ has been observed in experiment.[46,190] In section 4.3.3, we calculated the atomic Li intercalation energies to be of the order of −1.8 eV/Li. This means that intercalation of Li metal has an enormous potential to stabilize the dehydrogenated state in reactions (4.11), (4.13) and (4.16). This stabilization is partially offset, however, by the energy cost to dissociate the $(Li)_n$ cluster. The net stabilization mechanism is:

$$(Li)_n \rightarrow n\,Li(^2S_{1/2}) \rightarrow n\,Li@C_\infty \tag{4.17}$$

The symbol at the right hand side denotes Li intercalated into graphite. The energy resulting from intercalation is substantial. With respect to bulk Li metal the energy gain is up to 0.3 eV/Li atom, see Table 4.3. With respect to a Li cluster the energy gain per Li atom is larger, and the total energy gain for a $(Li)_n$ cluster scales roughly linear with n. We model this effect by adding the $(Li)_n$ dissociation energy and n

times the optimal intercalation energy (−1.86 eV/Li, see Table 4.3) to the vacuum reaction enthalpies.

We also have to account for the possible binding of the various clusters to the graphite surface. We approximate the binding of the clusters $(LiBH_4)_n$, $(LiH)_n$, $(LiB)_n$, $(B)_n$ and $Li_2B_nH_n$ to graphite by the binding to a single graphene layer, and use the numbers from Sec. 4.3. We believe this to be a reasonable approximation. The binding energies of the larger clusters to graphene are actually quite moderate, and they will partly cancel when considering a decomposition reaction, (4.10)-(4.16). The binding energies of $(LiBH_4)_n$, $(LiH)_n$ and $Li_2B_nH_n$ clusters either are roughly independent of the size n, or even decrease with increasing n, so any error made per $LiBH_4$ unit will decrease with increasing n. As for the size of the error, for a single Li atom we found a maximal difference of 0.2 eV between binding to a single graphene sheet and to a graphite surface. This difference is caused mainly by a difference in (electrostatic) screening of the charge transferred between the Li atoms and the substrate. For $(LiBH_4)_n$, $(LiH)_n$ and $Li_2B_nH_n$ clusters we do not have such a charge transfer, but even if the difference between binding to graphene and graphite would be as large as 0.2 eV, per $Li(BH)_4$ unit it would roughly scale as $0.2/n$ eV, and thus become rapidly negligible for larger clusters. The binding of $(B)_n$ clusters is dictated by local covalent bonding to the (top) graphene layer, where screening effects are of minor importance.

$(LiB)_n$ clusters might be a case where one should be more careful as they bind to graphene with a substantial energy. However, decomposition of $(LiBH_4)_n$ to $(LiB)_n$, reaction (4.15), turns out to be unfavorable with respect to other reaction paths. In order to have reaction (4.15) become competitive with other reactions, an increase of the binding of $(LiB)_n$ to the substrate of more than ~ 1 eV per LiB is required. It is extremely unlikely to get such a large stabilization by adding graphite layers.

$\underline{n = 4}$ Figure 4.2 shows the change in free energy ΔG per formula unit of $LiBH_4$ as a function of temperature for the possible decomposition reactions (4.10-4.16). The figure compares the reactions in vacuum to the reactions in contact with the carbon host. Note that the reactions without Li metal as product are hardly affected. Evidently the binding energy to the surface does not matter much. The effects for the other three reactions are dramatic: The intercalation of Li into the carbon host shifts the curves pertaining to reactions (4.11), (4.13) and (4.16) down with 0.78, 1.22 and 1.35 eV, respectively. The reaction equilibrium is achieved at a temperature T_d at which $\Delta G(T_d) = 0$. Without graphite, the small $(LiBH_4)_4$ cluster decomposes only at a very high temperature $T_d \gtrsim 1300$ K. The dehydrogenation reaction to $(LiB)_4$ is then most favorable. With graphite, all reactions leading to (intercalated) Li have a lower ΔG. Indeed reaction (4.13), leading to Li, B_2H_6 and H_2, has now become most favorable, with a decomposition temperature $T_d \approx 800$ K.

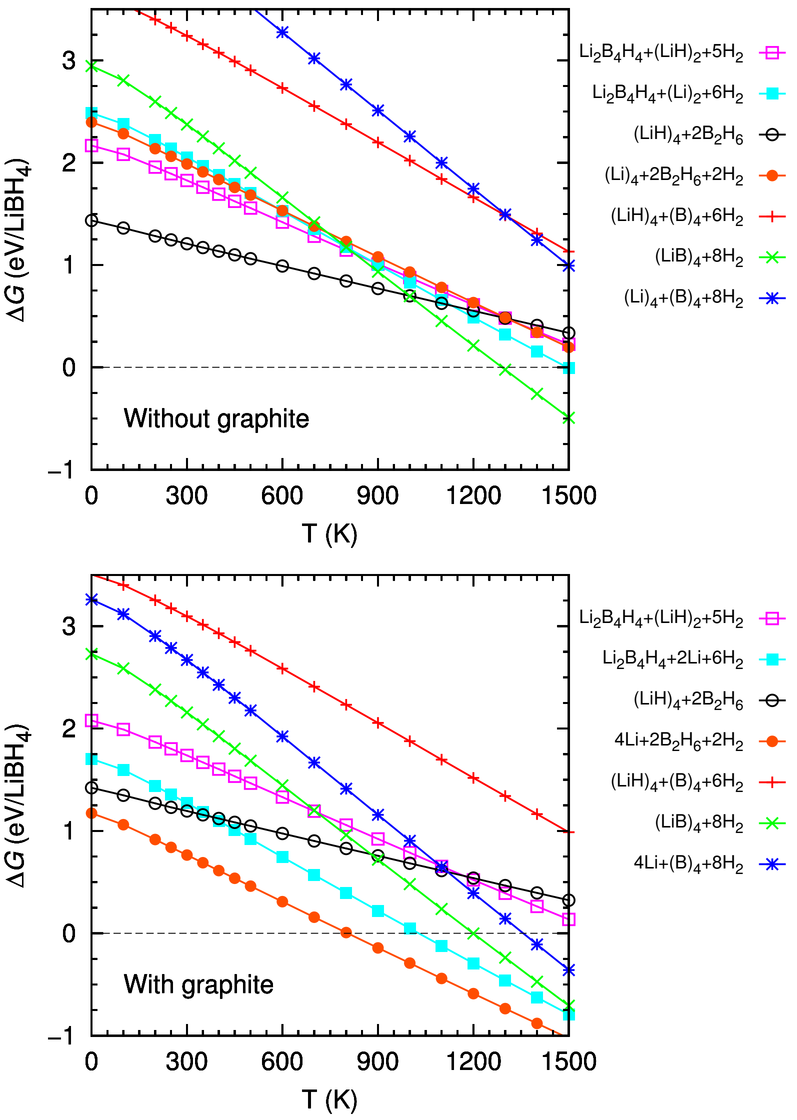

Figure 4.2: ΔG/$LiBH_4$ f.u. of $(LiBH_4)_4$ cluster as a function of temperature for different possible decomposition reactions without and with the presence of graphite.

$\underline{n = 12}$ For the larger cluster (see figure 4.3), we observe a similar behavior. The reactions leading to intercalated Li are stabilized, whereas other reactions are hardly affected. Without graphite, the $(LiBH_4)_{12}$ cluster decomposes at $T_d \approx 800$ K. The most favorable reaction path is reaction (4.10), where $Li_2B_{12}H_{12}$ and $(LiH)_{10}$ clusters are formed, and hydrogen is desorbed. Decomposition of the $(LiH)_{10}$ clusters takes place at much higher temperatures, $T_d \approx 1200$ K. Compared to the smaller cluster of Fig. 4.2, reaction (4.15) to $(LiB)_n$ and hydrogen has become unimportant, as it outperforms the others only for temperatures $T > 1200$ K. With graphite, the $(LiBH_4)_{12}$ cluster decomposes at a much lower temperature $T_d = 500$ K, according to reaction (4.11), where besides $Li_2B_{12}H_{12}$ clusters, (intercalated) Li and hydrogen

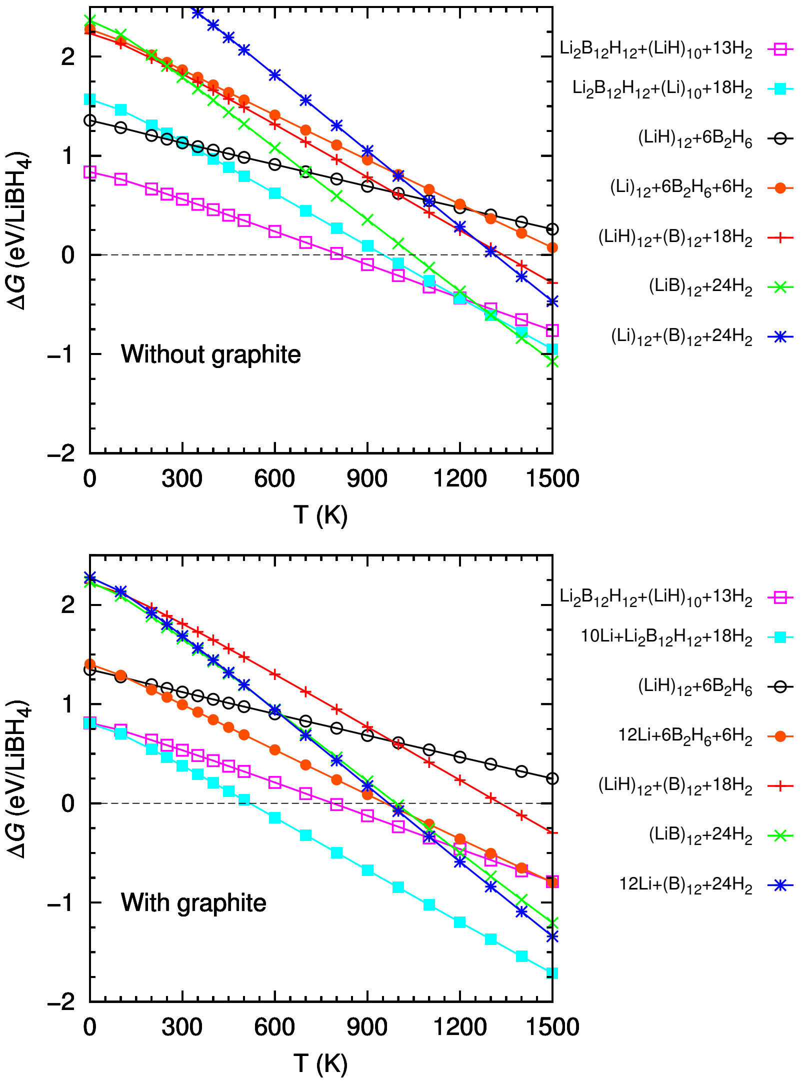

Figure 4.3: ΔG/$LiBH_4$ f.u. of $(LiBH_4)_{12}$ cluster as a function of temperature for different possible decomposition reactions without and with the presence of graphite.

is formed. Compared to the graphite-free case, the presence of graphite thus promotes the immediate decomposition of LiH clusters, thus releasing more hydrogen. Compared to the smaller cluster of Fig. 4.2, reaction (4.13), which releases B_2H_6 besides H_2, is not favorable. This means that from a thermodynamic point of view it is unlikely that B_2H_6 gas is formed in the decomposition of larger clusters.

Larger clusters

So far, we have considered the decomposition of $(LiBH_4)_n$ clusters with $n = 4$ and 12 by explicit calculations on these small clusters. Here we want to model the stabilizing effect of Li intercalation for clusters of larger size.

In a previous work,[157] we modeled the equilibrium shape of large nanoclusters by using calculated surface energies and the Wulff theorem.[115] Once the shape of a nanocluster is determined, we calculate its total energy by,

$$E_{\text{cluster}}(n) = nE_{\text{bulk}} + \sum_i \gamma_i A_i \tag{4.18}$$

where γ_i is the surface energy of the ith nanocluster face, and A_i is the area of the corresponding face. E_{bulk} is the bulk total energy per f.u..[e] With this simple model one can study the H_2 desorption energy as a function of n (figure 8(a) of Ref. 157) and as a function of pore size (figure 9(a) of Ref. 157). For the latter we assume that the pores are spherical and of a fixed size and that each pore is filled with the largest possible crystallite of optimal shape of a single compound.

Here we use the same model, but also model the effect of the stabilisation mechanism of (4.17) above. So we assume each $(Li)_n$ to be dissociated (adding the $(Li)_n$ dissociation energy) and the Li atoms to have intercalated into graphite (adding $n\times-1.80$ eV). As $Li_2B_{12}H_{12}$ is a stable phase, we switch from reactions (4.10) and (4.11) to (4.19) and (4.20) for larger clusters,

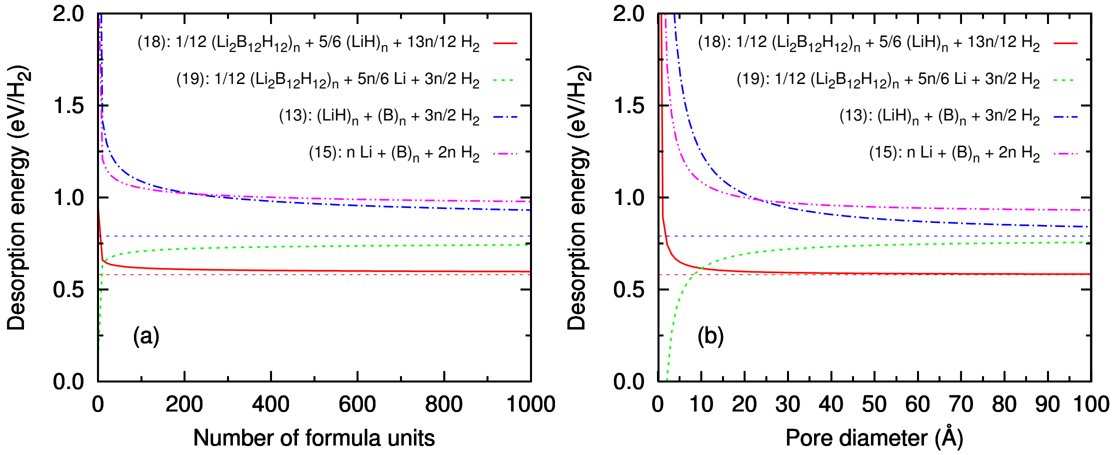

Figure 4.4: Calculated desorption energies as a function of (a) the number of f.u., (b) and pore diameter. For reactions (4.16) and (4.20), the dehydrogenated state with Li intercalated into graphite is plotted.

$$(LiBH_4)_n \leftrightarrow \frac{1}{12}(Li_2B_{12}H_{12})_n + \frac{5}{6}(LiH)_n + \frac{13n}{12}H_2(g), \tag{4.19}$$

$$(LiBH_4)_n \leftrightarrow \frac{1}{12}(Li_2B_{12}H_{12})_n + \frac{5}{6}(Li)_n + \frac{3n}{2}H_2(g). \tag{4.20}$$

---

[e] A test calculation on a $(LiBH_4)_{56}$ cluster showed that the Wulff construction is sufficiently accurate for larger clusters.[157]

Figure 4.4 shows the desorption energies per H_2 released, as a function of (a) the number of f.u. n, and (b) pore diameter, for the desorption pathways of reactions (4.14), (4.16), (4.19) and (4.20).

For large clusters, the stabilization mechanism of (4.17) is unable to push the desorption temperatures of the reaction in the proximity of graphite below those of the reactions in absence of graphite, i.e. reaction (4.14) occurs at lower temperature than reaction (4.16), and (4.19) occurs at lower temperature than (4.20). Indeed, except for very small clusters, the desorption energy of (4.14) drops faster with size than (4.16), and the desorption energy of (4.20) even increases where that of (4.19) drops. So there is no apparent beneficial effect of Li intercalation and nano-structuring, except at a very high temperature, where decomposition of $LiBH_4$ into the elements, reaction (4.16), would be favored.

For small pore and cluster size, the situation is different. In case of very small pore size (diameter $\lesssim$ 1.0 nm), Li intercalation leads to lower hydrogen desorption temperatures *via* reaction (4.20). For larger pore sizes the beneficial effect on this particular reaction is lost. If we consider higher temperatures where other reactions become important, the effect of Li intercalation is operative for larger clusters/pores. For pore sizes $\lesssim$25 Å, reaction (4.16) is more favorable than (4.14). Indeed, the effect on the hydrogen desorption energy is 0.2 eV/H_2 for a 10 Å pore diameter.

4.4 Conclusions

In a previous work,[157] we showed that the improved (de)hydrogenation properties of nano-confined $LiBH_4$ particles observed in experiment cannot be caused by changes in the thermodynamics of the unsupported $LiBH_4$ nanoclusters. In summary, we found that the reaction energies of nanoclusters with a diameter $\gtrsim$ 2 nm are very close to that of bulk $LiBH_4$. Only very small clusters with a diameter $<$ 1 nm are significantly destabilized relative to the bulk. The thermodynamics of such small clusters is unfavorable, however, and leads to dehydrogenation temperatures that are higher than that of the bulk. We concluded that such experimentally observed improvements could have a kinetic origin. Alternatively, the thermodynamics of the reactions might be altered by the chemical interactions between the reactant/products and the nanoporous host material.

In this work we have addressed key aspects of the latter issue, by (i) studying the interaction of the reactant/products clusters with a single graphene layer, and (ii) by evaluating the effect of reversible intercalation of Li, as one of the reaction products, into the graphite. Reversible Li intercalation into the graphitic carbon support during dehydrogenation of nano-confined $LiBH_4$ has been observed in experiment.[46,190]

DFT calculations on small $(LiBH_4)_n$, $n = 4$ and 12, clusters at the surface of a single graphene layer show that reaction energies are less sensitive to the interaction of these nanoclusters and the carbon template. Our findings show that intercalation of Li metal plays a more important role and has an enormous potential to stabilize the dehydrogenated state of reactions with $(Li)_n$ clusters as product, i.e. reactions (4.11), (4.13) and (4.16). We calculated the atomic Li intercalation energies to be of the order of -1.8 eV/Li. By adding the $(Li)_n$ dissociation energy to the intercation energy and considering small interactions between nanoclusters and the carbon template, we obtained much lower decomposition temperatures for small $(LiBH_4)_n$, $n = 4$ and 12, clusters.

For larger $(LiBH_4)_n$ clusters, the Li intercalation effect in stabilizing the dehydrogenated state becomes small. This is partly due to the fact that the stabilization mechanism (4.17) becomes less active and reaches the limiting value of E_{interc}, i.e. approximately 0.20 eV/Li. In addition, as the stability of the $(LiH)_n$ clusters increases with size, the dehydrogenated state with $(LiH)_n$ [and not $(Li)_n$] clusters becomes more favorable for larger $(LiBH_4)_n$ clusters.

In conclusion: Li intercalation into graphitic structures is important in stabilising the dehydrogenated state in nano-clusters. It allows for H that is trapped in LiH to be released. Only for small clusters it can tip the thermodynamic balance between competing desorption pathways, and only for very small clusters it can reduce the desorption temperature.

ACKNOWLEDGMENTS

The authors thank Petra de Jongh and Peter Ngene for useful discussions. The work of EH is part of the “Sustainable Hydrogen” program of Advanced Chemical Technologies for Sustainability (ACTS), project no. 053.61.019. The work of GAW is part of the “Stichting voor Fundamenteel Onderzoek der Materie (FOM)” with financial support from the “Nederlandse Organisatie voor Wetenschappelijk Onderzoek (NWO)”.

Chapter 5

Orbital magnetic susceptibility from chemical shielding calculations

Abstract

A simple method is presented to obtain the macroscopic orbital magnetic susceptibility χ_{ij} by means of chemical shielding calculations in a repeated slab geometry. This allows for a GIPAW (Gauge-Including Projector-Augmented Wave) determination of χ_{ij} without any additional approximation. It is an alternative to bulk linear response calculations of χ_{ij}. Therefore it opens a route to the determination of χ_{ij} using the novel "converse" approach to NMR shielding by Thonhauser *et al.* (and thus enables a complete modelling of chemical shielding, including susceptibility effects, on the basis of the converse approach only).

5.1 Introduction

The magnetic susceptibility is a bulk quantity that is defined as

$$\chi_{ij} = -\frac{d^2E}{dB_i dB_j} \quad . \tag{5.1}$$

Here E is the total energy per unit volume, and B_i are the cartesian components of the magnetic field. The magnetic susceptibility is important in macroscopic magnetostatics. It relates the magnetic induction **B** and magnetization **M** in a material to the magnetic field strength **H** according to:

$$\begin{gathered} B_i = (\delta_{ij} + 4\pi\chi_{ij})H_j = H_i + M_i \Rightarrow \\ M_i = 4\pi\chi_{ij}H_j \overset{\chi\ll 1}{\approx} 4\pi\chi_{ij}B_j \quad . \end{gathered}$$

Here we have used that for small susceptibilities $\chi \ll 1$ we can simplify and set $B_i = H_i$. If one brings a system into an external field, a magnetization **M** develops that, in turn, gives rise to induced surface currents. These surface currents are the source of an induced macroscopic field. A formalism to calculate χ for infinite systems from first-principles density functional theory was developed by Mauri and co-workers.[62,64] It is exact for an all-electron (AE) Hamiltonian. In practice, $1/r$-potentials are often removed for solid state calculations, e.g., *via* Blöchl's Projector-Augmented Wave (PAW) method.[69] In their Gauge-Including PAW (GIPAW) method Pickard and co-workers have extended the PAW method to remove numerical gauge problems arising from uniform magnetic fields.[63,67] This resulted in an approximated GIPAW expression for the susceptibility (their specific aim was a GIPAW formalism for chemical shielding), which is often used and generally works quite well.

The bulk susceptibility plays an important role in modelling chemical shielding. The NMR shielding tensor is defined as

$$\sigma_{\mathrm{R},\alpha\beta} = -\frac{\partial B^{\mathrm{ind}}_{\mathrm{R},\alpha}}{\partial B^{\mathrm{ext}}_{\beta}} \quad . \tag{5.2}$$

Here $B^{\mathrm{ind}}_{\mathrm{R},\alpha}$ is the induced field at the nuclear position **R** that arises in response to the uniform, external magnetic field B^{ext}_{β}. This induced field is naturally separated into two components. One component, $\mathbf{B}^{\mathrm{ind}}(\mathbf{G} \neq 0)$ (**G** are the reciprocal lattice vectors), is the consequence of the microscopic currents that flow in the material. These currents often flow in the immediate vicinity of the nucleus **R** but that is not necessarily so. They are an intrinsic property of the infinite crystal. The other component, $\mathbf{B}^{\mathrm{ind}}(\mathbf{G} = 0)$, is the consequence of currents induced on the surface of the sample. These are macroscopic currents, so they should be modeled *via* the macroscopic susceptibility χ. This component of the induced field is not a bulk property and it depends on the shape of the sample. Typically a spherical shape is assumed, so the induced field is uniform throughout the sample. For a cubic material (χ is just a scalar) one has:

$$\mathbf{B}^{\text{ind}}(\mathbf{G}=0) = \frac{8\pi}{3}\chi\mathbf{B}^{\text{ext}} \quad . \tag{5.3}$$

In linear response GIPAW NMR shielding calculations the already mentioned approximate expression for χ_{ij} is available.[62,64] Recently, however, an alternative approach to calculate GIPAW shieldings has been developed on the basis of the novel "converse" approach to NMR shieldings.[71,74] Here the shielding is calculated as:

$$\sigma_{\text{R}\alpha\beta} = -\Omega\frac{\partial M_\beta^{\text{ind}}}{\partial m_{\text{R}\alpha}^{\text{ext}}} \quad . \tag{5.4}$$

Here Ω is the super cell volume and $\mathbf{M}$ is the magnetization that is induced in response to an external magnetic moment $m_{\text{R}\alpha}^{\text{ext}}$ placed at nuclear position $\mathbf{R}$. The response is calculated in *finite field*, using the "modern theory of orbital magnetization" that provides a closed expression for an all-electron Hamiltonian of non-interacting particles:[72]

$$\mathbf{M}^{\text{ind}} = \frac{1}{16c\pi^3}\text{Im}\sum_n^{\text{occ}}\int_{\text{BZ}}\langle\partial_{\text{k}}u_{n\text{k}}|\times(H_k+\epsilon_{nk})|\partial_{\text{k}}u_{n\text{k}}\rangle\, d\mathbf{k} \quad . \tag{5.5}$$

This expression solves the position operator problem (the position operator is not bound in an infinite system) and is the basis for a GIPAW theory of chemical shielding.[74] It gives $\mathbf{B}^{\text{ind}}(\mathbf{G}\neq 0)$. It accounts for kind of surface currents, but these are shape-independent, microscopic currents. To model $\mathbf{B}^{\text{ind}}(\mathbf{G}=0)$, shape-dependent, macroscopic surface currents are needed. However, how can we calculate χ with this new method?

In this chapter we explore an alternative way to calculate χ. We use a supercell, and calculate shieldings for a slab of material. The surfaces of the slab carry the macroscopic currents, so inversion of the route outlined above from χ to surface currents to $\mathbf{B}^{\text{ind}}(\mathbf{G}=0)$, will give us χ. This method allows to (a) obtain susceptibilities in the GIPAW formalism without additional approximations, (b) provides a way to calculate χ using the converse approach. The price to pay is having to deal with the surface currents explicitly. We will explore how independent it is on surface termination.

This chapter is organized as follows: Section 5.2 outlines the various methods. Section 5.3 present results, ranging from model systems (inert gas solids) to ionic and covalently bound crystals. Section 5.4 finishes with a brief conclusion.

5.2 theory

5.2.1 Linear response on infinite systems

In the 1990s a method to calculate χ was developed by Ohno, Mauri and Louie.[62,64] They calculate χ from Eq. 5.1 using second-order perturbation theory for a perturbing field with finite wavelength (characterized by a wavenumber $\mathbf{q}$) and take the long-wavelength limit ($\mathbf{q} \to 0$). Application of the f-sum rule insures a numerically well-behaved expression. In practice their approach boils down to the numerical calculation of a second derivative in $\mathbf{q}$ for sufficiently small $\mathbf{q}$. It is an all-electron method, but pseudopotential calculations are feasible for light elements.[62]

In Refs. 63 and 67, Mauri and co-workers adapted this method for χ to the GIPAW formalism in order to be able to treat efficiently also solids with heavier nuclei. (This enabled them to model $\mathbf{B}^{\text{ind}}(\mathbf{G}=0)$: the surface-current contribution to the chemical shielding *via* Eq. 5.3.) Summarizing their expressions:

$$\chi_{ij} = \lim_{q\to 0}(2-\delta_{ij})\frac{[Q_{ij}(q) - 2Q_{ij}(0) + Q_{ij}(-q)]}{q^2} \quad . \tag{5.6}$$

This expression is calculated for small $\mathbf{q}$. The tensor Q is constructed as:

$$Q(q) = \frac{-1}{c^2 N_{\text{k}} V_c} \sum_{i=x,y,z} \sum_{o,\text{k}} \text{Re}\left[\langle \bar{u}^{(0)}_{o,\text{k}} | \hat{\mathbf{u}}_i \times (-i\nabla + \mathbf{k}) \mathcal{G}_{\text{k}+\text{q}_i}(\epsilon_{o,\text{k}}) \hat{\mathbf{u}}_i \times \mathbf{v}_{\text{k}+\text{q}_i,\text{k}}(\epsilon_{o,\text{k}}) | \bar{u}^{(0)}_{o,\text{k}} \rangle \right] \quad . \tag{5.7}$$

For an explanation of all symbols we refer to Ref. 67. Here we note that the two vector products give the cartesian direction of Q. Around each $\mathbf{k}$-point in the BZ summation a cartesian star of points ($\mathbf{k} + \mathbf{q}_i$) is constructed. The above expression discards one-center corrections, and in the AE limit (i.e. the PAW transform becomes the identity) becomes the exact AE expression of Refs. 62 and 64.

5.2.2 Supercell method

When a material is put into a uniform external magnetic field, the induced field is shape dependent. Using the so-called depolarization coefficients, one can write for the macroscopic fields:[191]

$$\begin{aligned} B_\alpha = B_\alpha^{\text{ext}} + 4\pi(1-n_\alpha)M_\alpha = \\ B_\alpha^{\text{ext}} + 4\pi(1-n_\alpha)\chi B_\alpha^{\text{ext}} \end{aligned} \tag{5.8}$$

Here we assume an isotropic χ for simplicity. For an infinite slab we have $n_x = n_y = 0$ and $n_z = 1$, where we have chosen z as surface normal. So $B_z = B_z^{\text{ext}}$. For the other two components we get an additional field, proportional to χ. This is the shape dependent field $\mathbf{B}^{\text{ind}}(\mathbf{G} = 0)$, that is a consequence of the induced surface current density $\mathbf{K} = c\chi\mathbf{B}^{\text{ext}}\times\hat{\mathbf{z}}$. Using Eq. 5.8 in the linear regime, we rephrase it in terms of shieldings:

$$\begin{aligned} \sigma_{\text{R},\perp} &= \sigma^{\text{bulk}}_{\text{R},\perp} = \sigma^{\text{bulk}}_{\text{R,iso}} \\ \sigma_{\text{R},\parallel} &= \sigma^{\text{bulk}}_{\text{R},\parallel} - 4\pi\chi = \sigma^{\text{bulk}}_{\text{R,iso}} - 4\pi\chi \end{aligned} \tag{5.9}$$

where $\perp$ denotes the surface normal (z) and $\parallel$ any direction parallel to the surface. Here $\sigma^{\text{bulk}}_{\text{R}}$ is the shielding for the infinite crystal. In an isotropic material, it is just the isotropic shielding $\sigma^{\text{bulk}}_{\text{R,iso}}$. It is immediately evident that χ can be obtained from the slab shielding tensor, for any $\mathbf{R}$ that is sufficiently "far" from the surface, i.e. the atom at $\mathbf{R}$ should not carry any contribution to the surface current $\mathbf{K}$ that, at the microscopic level, extends over a finite width near the surface.

We now have a recipe to obtain χ from a chemical shielding calculation. We build a supercell, infinitely repeated in all 3 directions, containing a slab of the material for which we want to know χ. We calculate the chemical shielding tensor for an atom deep inside the material and obtain the χ from the difference between the normal and parallel components (alternatively we can use $\sigma^{\text{bulk}}_{\text{R,iso}}$ from a calculation on the infinite crystal). The key point is that we have included the macroscopic surface current in our microscopic system.

The surface has to be non-metallic, otherwise the chemical shielding calculation fails. An additional complication is caused by the periodic nature of the system. Would there be only one slab, the macroscopic field in the vacuum would vanish and the field inside the material would just be given by Eq. 5.8. However, with periodic boundary conditions a finite field exists in the vacuum region. This field is parallel to the surface, as it is caused by the (periodically repeated) surface current density $\mathbf{K}$ only. Parallel components of the fields inside the slab are also affected. The surface current density $\mathbf{K}$ is not affected by the periodic boundary conditions and neither is the jump across the surface in the parallel components of the macroscopic field. Calculating the nucleus independent chemical shielding (NICS) in the vacuum region then solves the problem:

$$\sigma_{\text{R},\parallel} - \sigma^{\text{NICS}}_{\text{vacuum},\parallel} = \sigma_{\text{R},\perp} - 4\pi\chi \quad . \tag{5.10}$$

This equation defines the recipe to calculate χ for a cubic material.[a] Fig. 5.1 summarizes the method.

An illustration of the method for bulk Ne is given in Figure and Table 5.1. In the infinite bulk, the Ne shielding is isotropic. Here we consider a slab of fcc Ne. The

---

[a] The general recipe is: $\sigma^{\text{slab}}_{ij} - \sigma^{\text{NICS}}_{ij,\text{vacuum}} = \sigma^{\text{bulk}}_{ij} - 4\pi\chi_{ij}$, where the cartesian directions i and j are perpendicular to the surface normal.

	layer	σ_{xx} (ppm)	σ_{yy} (ppm)	σ_{zz} (ppm)
Ne	1	203.94	203.94	200.69
Ne	2	200.55	200.55	197.72
Ne	3	200.52	200.52	197.73
Ne	4	200.52	200.52	197.73
Ne	5	200.52	200.52	197.73
Ne	6	200.52	200.52	197.73
Ne	7	200.55	200.55	197.72
Ne	8	203.94	203.94	200.69
Vac	9	−3.46	−3.46	−0.51
Vac	10	−3.73	−3.73	0.01
Vac	11	−3.72	−3.72	0.00
Vac	12	−3.72	−3.72	0.00
Vac	13	−3.73	−3.73	0.01
Vac	14	−3.46	−3.46	−0.51

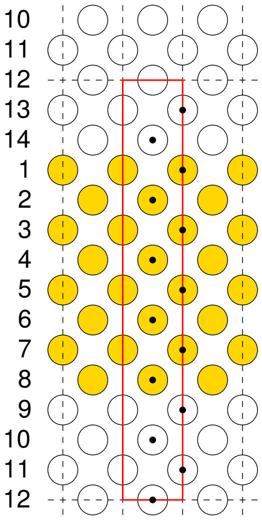

Table 5.1: Left: Table with Ne shielding as a function of layer number. Right: Schematic view of fcc Ne slab. Yellow spheres: Ne atoms, empty spheres: Ne lattice continued with empty spheres. Dots: NICS and Ne nuclear positions. Red box: unit cell. Three complete cells are shown. The periodic layer numbering is indicated on the left.

atomic layers are consecutively numbered, as are the NICS positions that are chosen to be on empty “lattice” sites in the vacuum. With the field oriented normal to the surface (the z-direction), the Ne nuclei inside the material all have the same shielding $\sigma_{zz} = 197.73$ ppm. This is the bulk isotropic Ne shielding.[b] Moving away from the surface, into the vacuum region, the NICS becomes 0. Indeed, a magnetic field applied perpendicular to the surface cannot induce surface currents in this system. With the field parallel to the surface, the surface current densities give rise to induced uniform fields in the vacuum and inside the slab. The latter field is $197.73 - 200.52 = -2.79$ ppm. In the vacuum the field is 3.73 ppm. We observe that both fields are uniform, provided we keep away from the sites near the surface, i.e. from the regions carrying the surface currents. The susceptibility χ is proportional to the difference: $4\pi\chi = -2.79 - 3.73 = -6.52$ ppm. See section 5.3.1 below for numerical results.

It is possible to avoid calculation of $\sigma^{\mathrm{NICS}}_{\mathrm{vacuum},\|}$ in the vacuum, using that the vector potential of the field arising from $\mathbf{K}$ has to be cell-periodic:

$$(\sigma_{\mathrm{R},\|} - \sigma_{\mathrm{R},\perp})L_{\mathrm{slab}} + \sigma^{\mathrm{NICS}}_{\mathrm{vacuum},\|}L_{\mathrm{vac}} = 0 \quad .$$

Here L_{slab} is the distance separating the current densities $\mathbf{K}$ on either side of the slab, and L_{vac} is the distance separating the current densities on either side of the vacuum.

---

[b] Excluding the shielding due to core electrons.

Inserting this into Eq. 5.10 yields:

$$\sigma_{\mathrm{R},\parallel} - \sigma_{\mathrm{R},\perp} = -4\pi\chi \frac{L_{\mathrm{vac}}}{L_{\mathrm{vac}} + L_{\mathrm{slab}}} = -4\pi\chi \frac{L_{\mathrm{vac}}}{L_{\mathrm{cell}}} \quad . \tag{5.11}$$

So one just has to calculate $(\sigma_{\mathrm{R},\parallel} - \sigma_{\mathrm{R},\perp})$ for several values of the fraction $L_{\mathrm{vac}}/L_{\mathrm{cell}}$, and extrapolate the straight line to $L_{\mathrm{vac}}/L_{\mathrm{cell}} = 1$. Note that we only roughly know L_{vac} and *a priori*. The requirement of linear scaling can be used to fix it in practice.

There are two ways to calculate the shieldings $\sigma_{\mathrm{R},\parallel}$ and $\sigma_{\mathrm{R},\perp}$ in the slab: (i) using GIPAW linear response (LR) and (ii) using the converse method.[71,74] In (i) the linear response formalism of Ref. 67 is employed for the slab (retaining only the $\mathbf{G} \neq 0$ components). In (ii) a magnetic moment is applied to the nucleus (or, for the NICS, a vacuum position) of interest, and the induced moment is calculated in GIPAW.[74] Contrary to (i) the converse approach is a supercell method by construction and the cell has to be chosen sufficiently large so that the response to the periodic images of the applied moments does not interfere.

5.2.3 Technical details

Calculations were done with the Vienna *ab initio* simulation program (VASP),[53,54] using various flavors of density functional theory (DFT).

Applications of the converse method (Ref. 74) are restricted to norm-conserving (NC) PAW data sets, i.e. the partial waves $|\phi_n\rangle$ and pseudo partial waves $|\tilde{\phi}_n\rangle$ have identical norm (cf. Refs 69 and 52):

$$\langle\tilde{\phi}_n|\tilde{\phi}_m\rangle - \langle\phi_n|\phi_m\rangle = 0 \quad .$$

NC data sets had to be constructed. Details will be reported below.

5.3 results

We discuss three systems, ranging from a solidified noble gas (Ne), *via* an ionic solid ($LiBH_4$), to a covalently bonded crystal (diamond C). All systems are insulators, but exhibit vastly different electron localisation.

5.3.1 fcc Ne

Noble gas atoms have closed electronic shells that exhibit little interaction with each other in the solid state. Thus they are closest to the classical textbook limit of individual, polarizable units.[192] Here we calculate χ for fcc Ne with a lattice constant $a = 4.429$ Å.

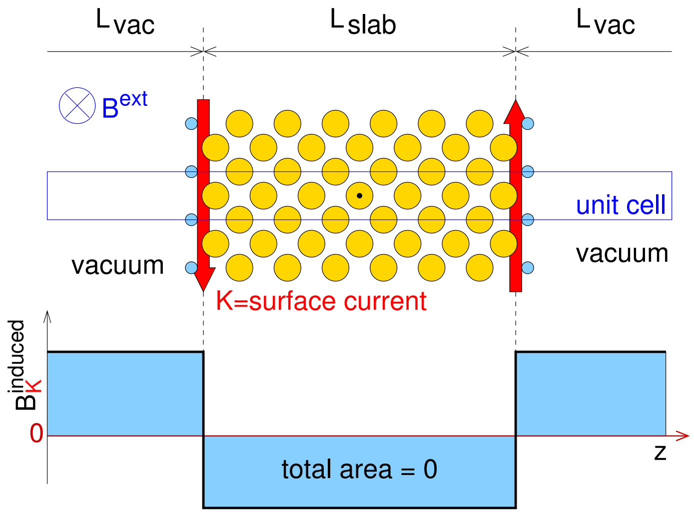

Figure 5.1: Schematic overview of the unit cell and macroscopic induced fields. A field $\mathbf{B}^{\mathrm{ext}}$ is applied perpendicular the paper and parallel to the surface. Macroscopic surface currents $\mathbf{K}$ and an induced field $\mathbf{B}^{\mathrm{ind}}$ result. The induced field is also perpendicular to the paper. The integral of $\mathbf{B}^{\mathrm{ind}}$ along z should vanish, because periodic boundary conditions prevent its vector potential from having a component with $\mathbf{G} = 0$.

We use several PAW data sets: (1) The standard Ne data set as supplied with the VASP distribution. It has a d-reference, two augmentation channels for $\ell = 0$, two augmentation channels for $\ell = 1$, and a frozen [He] core. (2) A hard, accurate all-electron data set. It is "all-electron", but still a PAW reconstruction is done in the vicinity of the nucleus. It is not a "true" all-electron data set with only a $1/r$-potential. (3) A simple NC data set that was needed for the test calculations using the converse method. It has a d-reference, and only one s and one p augmentation channel ($r_c = 1.4$ and $r_c = 1.7$ Bohr radii, respectively). Again, it has a frozen [He] core. For all Ne calculations we use LDA.[193,194]

Table 5.2 lists χ obtained with the bulk GIPAW linear response method. The result with the standard data set (3.95×10^{-6} cm^3/mole) is almost a factor 2 too small, compared to the AE number (7.81×10^{-6} cm^3/mole). The AE and NC PAW data sets yield much better agreement with the true AE number of Ref. 64. Evidently, both data sets mimic AE behaviour much better, but it appears that the lack of one-centre corrections in Eq. 5.7 still has a small effect.

The susceptibilities calculated with the supercell method are summarized in Table 5.3. They are obtained using GIPAW linear response (all data sets) and the converse approach (the NC data set only). A dramatic improvement is observed. The standard data set now gives a much better χ. It is ~ 15 % below the AE number. The NC data set yields a χ that is approximately 5 % too large. This is very reasonable, in view of the modest quality of the data set. The converse and LR give

Table 5.2: Magnetic susceptibility of fcc and atomic Neon calculated using linear response. All VASP PAW calculations were carried out with the *pGv* expression given by Eq. 5.7.

		χ (10^{-6} cm^3/mole)
fcc bulk	VASP PAW: standard (US)	−3.95
fcc bulk	VASP PAW: AE (US)	−7.27
fcc bulk	VASP PAW: NC	−7.46
fcc bulk	AE (no PAW)[a]	−7.81
atom	VASP PAW: AE (US)	−7.27
atom	AE (no PAW)[a]	−7.80
atom	experiment [b]	−7.20

[a] from Ref. 64.

[b] from Ref. 62.

Table 5.3: Magnetic susceptibility χ of fcc Ne calculated using the supercell method. All (100) slabs have $\sqrt{2} \times \sqrt{2}$ surface unit cells, unless stated otherwise.

			χ (10^{-6} cm^3/mole)	
PAW data set	surface		converse	LR
STD (US)	(100)			−6.79
STD (US)	(111)			−6.80
STD (US)	(100)	H_2 terminated		−6.79
AE (US)	(100)			−7.69
NC	(100)		−8.13	−8.21
NC	(100)	$2\sqrt{2} \times 2\sqrt{2}$	−8.13	
bulk AE[a]				−7.81

[a] AE bulk linear response from Ref. 64.

practically the same χ. The AE data set, being the most accurate data set, yields a very good result (~ 2 % difference with “true” AE).[c]

The results from Table. 5.3 show that our obtained χ are independent of the surface orientation [we obtain virtually identical shieldings for (100) and (111) oriented slabs] and that the surface termination does not matter (putting an insulating layer of H_2 molecules on the surface gives the same results as without). Indeed, these examples are consistent with the fact that χ is a bulk property, i.e. should not depend on any details of the surface.

For the (100) surface we have tried several thicknesses of the slab and vacuum regions, ranging from 6 to 10 and from 4 to 8 atomic layers, respectively. We observe hardly any dependence of χ (not shown in Table. 5.3). The results are also independent of the size of the surface unit cell. For the LR method, that is by construction. For the converse method, we observe no change going from a $\sqrt{2} \times \sqrt{2}$ to a $2\sqrt{2} \times 2\sqrt{2}$ surface unit cell. So already with a very small surface unit cell the response from periodic images is efficiently decoupled.

5.3.2 $LiBH_4$

$LiBH_4$ is an important prospective hydrogen storage material.[6,7,20–23] The bonding can be considered mixed ionic/covalent. The $[BH_4]^-$ anion has 4 hydrogen atoms surrounding the central boron atom in a nearly tetrahedral arrangement. The hydrogens are connected to the central boron with (polar) covalent bonds. The anions and the Li^+ cations arrange in a lattice held together by ionic forces. Such a lattice might again be considered as the textbook limit of individually polarizable units. However, significant band broadening occurs. Moreover, in a parallel study on the chemical shifts of $LiBH_4$ nano-clusters we found that the shift could *not* be modeled as the current response of the individual units. So indeed this system is already beyond the textbook limit. We are not aware of any experimental determination of χ for this system.

$LiBH_4$ has an orthorhombic structure belonging to the *Pnma* space group (No. 62). We use optimized lattice constants $a = 7.30$ Å, $b = 4.41$ Å and $c = 6.60$ Å from a previous calculation in Ref. 157. These values are close to the experimental values $a = 7.178$ Å, $b = 4.436$ Å and $c = 6.803$ Å.[134] Slabs were constructed as cuts from the bulk. In-plane lattice parameters were fixed to the optimized bulk parameters and all atoms in the slab were allowed to relax.[d] We used slabs with identical surfaces on either side and a vacuum region of more than 12 Å.

For H and Li AE PAW data sets were used. For B the 1s core state was kept in

---

[c] We neglect the very small difference between the valence-only and AE χ of Ne (cf. Ref. 64).

[d] Optimization carried out with standard PAW data sets as also used in Ref. 157.

the frozen core. All PAW data sets were norm-conserving, with two augmentation channels for $\ell = 0$ and two for $\ell = 1$. For this material we employed the Perdew-Burke-Ernzerhof generalized gradient approximation (PBE-GGA) to the exchange-correlation functional.[50] We checked **k**-point and kinetic energy cutoff convergence for the bulk system. Because we have norm-conserving data sets, the cutoff is quite large: $E_{\text{cut}} = 1100$ eV. The system is a wide band gap insulator ($E_{\text{gap}} > 4$ eV in GGA). We need only modest **k**-point meshes: $2 \times 4 \times 2$ is sufficient for the bulk. For the slabs we use meshes of similar quality. Using the converse method, we obtain identical chemical shifts in the primitive and a $1 \times 2 \times 1$ cell, where we have doubled the shortest cell dimension b. Evidently the response to periodic images of the external moment is small. We use only primitive surface unit cells in the slab calculations.

Table 5.4 shows the main results obtained with both slab methods and bulk linear response. The system is orthorhombic, so χ_{ij} is a tensor. We used (100), (010), (001) and (011) slabs to obtain χ_{xx}, χ_{yy} and χ_{zz} (the cartesian axes are aligned with the crystal axes).[e] This allows for several independent determinations of the χ_{ii}, e.g. χ_{xx} could be obtained from the (010), (001) and (011) slabs (as all have $\hat{\mathbf{x}}$ parallel to the surface). This gave very small differences, e.g., for χ_{xx} variations are of the order of 1 %. The slabs were thick enough (at least 28 Å), so that χ has become independent of the slab thickness.

For all i the χ_{ii} calculated with both slab approaches are in excellent agreement. Moreover, the bulk GIPAW LR result is very close to the slab results. For the yy and zz components the difference is negligible. For the xx there is small discrepancy of just 3 %. We conclude that the slab method works very well for this system, but that the improvement over the bulk LR approximation is small.

5.3.3 Diamond C

Diamond consists of an infinitely extended network of covalent bonds. It cannot be considered to be build out of independently polarizable units.

We used a lattice parameter $a = 3.573$ Å. Again we took norm-conserving PAW data sets. The C data set is very simple with just one augmentation channel for $\ell = 0$ and $\ell = 1$. To enable comparison with the AE susceptibility from Ref. 64 we used LDA.[193,194] A kinetic energy cutoff $E_{\text{cut}} = 1000$ eV was employed. The **k**-point convergence was carefully checked for both bulk and slab geometries. For, e.g., a 1×1 surface unit cell [primitive bulk terminated (001) square surface unit cell], we used a 12×12 **k**-point mesh. The susceptibility is converged in slab thickness [20 to 30 atomic layers for (001)]. Slabs were constructed as cuts from the bulk. The

---

[e] With this choice of axes the off-diagonal elements of χ_{ij} are 0. This follows from the crystal symmetry.

Table 5.4: Magnetic susceptibility χ of $LiBH_4$ and diamond C (10^{-6} cm^3/mole). Bulk LR results are calculated for the infinite crystal.

		Converse	Direct-LR	
	slab	χ(slab)	χ(slab)	χ(bulk-LR)
		$LiBH_4$		
χ_{xx}	(010)	−22.02	−22.10	−21.40
χ_{yy}	(011)	−21.66	−21.75	−21.66
χ_{zz}	(100)	−20.89	−21.02	−21.11
		cubic C		
(1×1)-1H	(111)	−10.70	−9.71	−9.78
($\sqrt{2}\times\sqrt{2}$)-2H	(001)	−10.63	−9.76	−9.78
(2×1)-1H	(001)	−10.62	−9.67	−9.78
(2×1)-Cl/H	(111)	−10.59	−10.18, −9.94	−9.78
bulk AE[a]				−10.4

[a] Valence only AE bulk linear response from Ref. 64.

in-plane lattice parameter was fixed to the bulk parameter and a few layers of carbon atoms near the surface and the Cl/H at the surface were allowed to relax.[f]

The main results are summarized in Table 5.4. The bulk GIPAW LR value underestimates the AE results of Ref. 64 by ∼ 6 %. For the slab approach we considered (111) and (001) surfaces and in both cases the dependence of χ on surface unit cell size and surface termination was studied. For the converse method, we observe only a very weak dependence on the surface unit cell size: for a cell with bulk termination and the dangling bonds saturated with hydrogens, the 1×1, 2×2, and 3×3 cells give practically identical results (variations of ∼ 0.1 ppm in the chemical shift tensor).

Table 5.4 shows our results for (a) the bulk terminated (111) surface, with a single hydrogen saturating the dangling bond, calculated in a 1×1 primitive, hexagonal surface unit cell, (b) the bulk terminated (001) surface, now with 2 hydrogens saturating the dangling bonds on each surface carbon, calculated in a non-primitive $\sqrt{2} \times \sqrt{2}$ surface unit cell, (c) the reconstructed (001) surface, with a dimer bond and one hydrogen per surface carbon atom, calculated in the 2×1 (primitive) surface unit cell, and (d) a 2×1 (111) cell, where one C has a hydrogen on top and the other has a Cl on top. In all these systems the band gap is determined by the surface: bulk

---

[f] Relaxation carried out using standard PAW data sets from the VASP distribution.

diamond has an LDA gap of ~ 3.1 eV. The system with the mixed Cl/H termination has a gap as small as 0.45 eV.

The converse method consistently yields a $\chi = 10.6 \times 10^{-6}$ cm^3/mole, with a maximal deviation of 0.1×10^{-6} cm^3/mole. This is very close to the bulk AE number of 10.4×10^{-6} cm^3/mole. The direct LR method yields somewhat smaller numbers, closer to the bulk LR result, and also showing a larger spread. For the Cl/H system, the result weakly depends on the orientation of the field applied parallel to the surface. This anisotropy suggests that surface states may affect the results, i.e. we do not calculate a pure bulk property. Indeed, the bulky Cl - that cause the small surface gap - form rows on the surface, and alternate with rows of H. The converse method is insensitive to these surface features. Further we note that the slab LR method, in most cases, yields results quite close to the bulk LR method. Both are in reasonable agreement with the AE number. Nevertheless, we consider this very close agreement “accidental” (in neither of the other systems the agreement was that close). Indeed, the slab LR results probably deviate from the true bulk number, because of additional surface currents.

5.4 Conclusion

Summarizing, we have studied an alternative route for the calculation of the orbital magnetic susceptibility by calculating the chemical shift tensors for a slab of material. For Ne this method yields a dramatic improvement over the approximate bulk GIPAW expression for χ. For LiBH$_4$ all methods perform (nearly) equally well, in that they yield very similar numbers. For diamond, the bulk GIPAW somewhat underestimates the AE χ. Interestingly, the slab method, when used with the converse approach for the shift tensor, yields very good results, where with the LR, there is some weak dependence on details of the surface (termination). A few remarks are in order:

(a) Surprisingly, the converse method works very well already with a small surface unit cell. The array of periodically repeated moments has to be applied far from the surface, in a genuinely bulk-like environment. The presence of the surface is crucial, as it breaks the symmetry and is solely responsible for the anisotropy in σ that is directly proportional to χ. Evidently the periodic images of the applied moment can be very close to the nucleus of interest, whereas its shielding still senses the presence of the surface at any (large) distance from the surface. (b) Another surprise is that the LR slab method still seems to be weakly sensitive to details of the surface termination, whereas the converse approach appears to be independent of those surface details (indeed, it gives even better numbers). In a formal sense, the shift calculated with the converse and the direct method have to be identical (it is just an interchange of energy derivatives).[71] The reason for the difference might be hidden in the boundary conditions, however. In the slab geometry, the surface states extending over the infinite surface, feel the uniform external field everywhere. In the converse, the applied perturbation is, in principle, local. It is reasonable to assume that the response also has to be. So in a sufficiently large unit cell, sustained surface currents over macroscopic distances should be impossible.

Some tension between (a) and (b) cannot be denied. Unfortunately the formalism used to calculate the shifts for periodic systems with the converse method does not provide direct access to the induced surface currents. So exploring (b) remains very hard. The LR response allows for a calculation of the currents. It remains to figure out how to separate the excess surface current from the bulk currents.

Summarizing, we have studied various methods for a wide range of chemical bonds. The slab methods provide an improvement over bulk GIPAW LR for localized systems. For more itinerant electron systems, but bulk GIPAW LR and the slab methods perform equally well. Both methods appear prone to some errors, but they are of a different nature. The different behaviour of the converse and LR slab methods opens up an interesting perspective. The LR slab method accounts for effects of surface termination. It probably gives numbers that are more meaningful when surface details do matter, e.g., in nano-structured materials. The converse slab methods appears more appropriate if the thermodynamic, bulk property is required. More research on the intricacies of these methods is desirable.

acknowledgements

The work of FV and GAW is part of the research programme of the “Stichting voor Fundamenteel Onderzoek der Materie (FOM)”, which is financially supported by the “Nederlandse Organisatie voor Wetenschappelijk Onderzoek (NWO)”.

Summary

Storage of hydrogen is one the most technically challenging barriers to the widespread commercialization of hydrogen-fueled light-duty vehicles. Compressed hydrogen gas tanks and cryogenic liquid hydrogen tanks are impractical due to safety concerns and small volumetric densities. Metal hydrides such as $MgNiH_4$ and $LaNi_5H_6$ are unfavorable due to their low gravimetric hydrogen density. Before 1997, complex hydrides were not considered as candidates for solid hydrogen storage systems for vehicular application. The pioneering work of Bogdanović and Schwickardi drastically changed this situation. They showed that, upon doping with selected titanium compounds, the dehydriding of $NaAlH_4$ could be kinetically enhanced.This breakthrough has led to a worldwide effort to develop alanates, amides and borohydrides (group I and II salts of $[AlH_4]^-$, $[NH_2]^-$ and $[BH_4]^-$ respectively) as practical hydrogen storage materials. This thesis is a study into such complex hydrogen storage materials using first-principles computations within the framework of density functional theory (DFT).

Complex metal hydrides such as lithium amide ($LiNH_2$) and lithium borohydride ($LiBH_4$) have the potential for higher gravimetric hydrogen capacities[g] than simple metal hydrides. In both $LiNH_2$ and $LiBH_4$, hydrogen is covalently bonded to central atoms (N and B) forming complex anions ($[NH_2]^-$ and $[BH_4]^-$) with Li ionized as Li^+.

For $LiNH_2$, the reversible reaction

$$\mathrm{LiNH_2 + LiH \leftrightarrow Li_2NH + H_2\,(g)}$$

releases more than 5 wt% of hydrogen in the temperature range 150 to 350 °C. It has a reaction enthalpy of $67\ \mathrm{kJmol^{-1}H_2}$. On-board applications of the $LiNH_2$ + LiH mixture as a solid state reversible hydrogen storage system face problems such as a high operating temperature and slow release kinetics. To solve such problems it is important to understand the mechanism of the $LiNH_2$ + LiH reaction. Dehydrogenation of $LiNH_2$ involves mass transport in the bulk crystal through lattice defects. The most elementary defects are Li and H point defects. **Chapter 2** of this thesis presents a first-principles study of native point defects and dopants in $LiNH_2$. The Li-related

---

[g] $LiNH_2$ and $LiBH_4$ consist completely of light-weigth elements from the top row of the periodic table.

defects Li_i^+ and V_{Li}^- are most abundant and determine the charge balance. Of the H-related defects, V_H^- is much more abundant than H_i^+. V_H^- in fact corresponds to a NH^{2-} ion in the amide lattice, whereas H_i^+ corresponds to a NH_3 molecule. Dopants such as Ti and Sc do not affect the concentration of intrinsic defects, whereas Mg and Ca can alter it by a moderate amount. Ti and Mg are easily incorporated into the $LiNH_2$ lattice, which may affect the crystal morphology on the nano-scale.

$LiBH_4$, with a gravimetric capacity of 18.5 wt%, is one of the most interesting complex hydrides for hydrogen storage. However, $LiBH_4$ is a relatively stable material that decomposes at a high temperature $\gtrsim$ 400 °C. Furthermore, rehydrogenation is only possible at extreme conditions with typical values for temperature and pressure of 600 °C and 350 bar H_2. In addition, de/rehydrogenation kinetics is slow, which is a common problem for the bulk complex hydrides. A recently adopted approach that helps to address such problems, is nanoconfinement in porous materials. Faster dehydrogenation kinetics is reported for $LiBH_4$ infiltrated in carbon aerogels, nanoporous carbon, or nanoporous silica, accompanied by a decrease of the dehydrogenation temperature by at least 100 °C. In addition, confinement of $LiBH_4$ in nanoporous carbon leads to a marked improvement of the reversibility of the hydrogen desorption.

These findings can be the result of changed kinetics, as obviously nanoconfinement puts a limit on the particle size, which will reduce the diffusion distance required for mass transport. Moreover, both the size of the clusters and their interactions with the host may modify the thermodynamics of the reactions. In **chapter 3** of this thesis the stability of $(LiBH_4)_n$ nanoclusters, as a function of their size, as well as the stability of a range of possible nanocluster decomposition products are investigated. From a thermodynamic point of view, the desorption reactions of unsupported $LiBH_4$ nanoclusters with a diameter larger than $\sim$ 2 nm are indistinguishable from those of bulk $LiBH_4$ [i.e. decomposition to $Li_2B_{12}H_{12}$, followed by a second decomposition step to LiH and B]. Only for clusters that have a diameter less than $\sim$ 1 nm, i.e. $(LiBH_4)_n$, $n < 12$, is the thermodynamics of the decomposition reaction significantly different. The thermodynamics of small clusters is, however, unfavorable, and leads to *higher* hydrogen desorption temperatures compared to the bulk. The reason is that, although $(LiBH_4)_n$ clusters are destabilized with respect to bulk, clusters of possible reaction products are even more destabilized.

As mentioned above, in addition to the size effects, the chemical interaction between the reactant/products and the template material can change the thermodynamics of hydrogen sorption reactions. Indeed, recent in situ X-ray Raman spectroscopy of $LiBH_4$ in porous carbon shows that part of the Li intercalates into the porous carbon during dehydrogenation. These effects are studied in **chapter 4** of this thesis. DFT calculations on small $(LiBH_4)_n$, $n = 4$ and 12, clusters at the surface of a single graphene layer show that reaction energies are less sensitive to the interaction of these nanoclusters and the carbon template. Our findings show that intercalation of Li metal plays a more important role and has an enormous potential to stabilize the dehydrogenated state of reactions with $(\mathrm{Li})_n$ clusters as product. We obtained much lower decomposition temperatures for small $(\mathrm{LiBH_4})_n$, $n = 4$ and 12, clusters. This route becomes unfavorable for larger $(\mathrm{LiBH_4})_n$ clusters, where dehydrogenation leads to the formation of $(\mathrm{LiH})_n$ clusters.

Understanding of NMR spectra of nano-particle assemblies requires accurate calculation of the orbital magnetic susceptibility χ to account for surface currents. In **chapter 5** of this thesis an alternative route for the determination of χ *via* a calculation of the chemical shift tensors for a slab of material is presented. Three examples ranging from a model system (inert gas solid) to ionic and covalently bound crystals are considered. For Ne model system this method yields a dramatic improvement over the approximate bulk GIPAW (Gauge-Including Projector-Augmented Wave) expression for χ. For $\mathrm{LiBH_4}$ all methods perform (nearly) equally well, in that they yield very similar numbers. For diamond, the bulk GIPAW somewhat underestimates the all-electron χ. Interestingly, for diamond the slab method yields very good results when used in combination with the converse approach[h] for the shift tensor. When used in combination with the GIPAW linear response for chemical shifts, there is a weak dependence on details of the surface (termination).

---

[h] In contrast to the "direct" approach of Mauri, Pfrommer and Louie, the "converse" approach by Thonhauser *et al.* allows the calculation of the NMR chemical shifts from the magnetization that is induced in response to an external magnetic moment $m^{\mathrm{ext}}_{\mathrm{R}\alpha}$ placed at nuclear position $\mathbf{R}$.

Samenvatting

De opslag van waterstof is een van de meest veeleisende hindernissen voor grootschalig gebruik (op commerciële basis) van voertuigen met waterstof als brandstof. Tanks voor gecomprimeerd waterstof gas en voor cryogeen vloeibaar waterstof zijn onpraktisch vanwege de veiligheid en de kleine waterstof volume dichtheden. Metaalhydrides, zoals $MgNiH_4$ en $LaNi_5H_6$ zijn geen goede optie vanwege een lage gravimetrische dichtheid. Voor 1997 werden ook complexe hydrides niet als kandidaten voor waterstof opslagsystemen toegepast in voertuigen beschouwd. Het pionierswerk van Bogdanović en Schwickardi heeft dit drastisch veranderd. Zij hebben laten zien dat de kinetiek van de dehydrogenatie van $NaAlH_4$ aanzienlijk kan worden verbeterd door doping met bepaalde Ti verbindingen. Deze doorbraak heeft ertoe geleid dat heden ten dage wereldwijd een grote inspanning wordt geleverd om alanaten, amides en boorhydrides (groep I en II zouten van respectievelijk $[AlH_4]^-$, $[NH_2]^-$ and $[BH_4]^-$) als waterstofopslag materialen te ontwikkelen. Dit proefschrift onderzoekt dergelijke complexe waterstofopslagmaterialen middels *first-principles* berekeningen op de computer, gebruik makend van de dichtheidsfunctionaal theorie (DFT).

De complexe metaal hydrides lithium amide ($LiNH_2$) en lithium boorhydride ($LiBH_4$) hebben potentieel een veel hogere gravimetrische waterstof capaciteit dan conventionele metaalhydrides.[i] Beiden zijn ionaire materialen, met Li^+ kationen en het waterstof covalent gebonden in een complex anionen ($[NH_2]^-$ en $[BH_4]^-$).

In de (reversibele) reactie

$$LiNH_2 + LiH \leftrightarrow Li_2NH + H_2\,(g)$$

komt meer dan 5 gewichtsprocent waterstof vrij, over het temperatuur traject van 150 to 350 °C. De reactie enthalpie is 67 $kJmol^{-1}H_2$. Toepassing van het $LiNH_2$ + LiH mengsel als vaste stof reversibel waterstof opslag systeem gaat gepaard met grote problemen, met name de (te) hoge temperatuur waarbij de reactie plaatsvindt en de trage kinetiek. Om deze problemen aan te pakken, is het van belang het mechanisme van bovenstaande reactie te doorgronden. Het vrijkomen van H_2 vanuit $LiNH_2$ gaat gepaard met massa transport door het kristal door rooster-defecten. De

---

[i] Zowel $LiNH_2$ als $LiBH_4$ bestaan geheel uit lichtgewicht elementen uit de bovenste rij van het periodiek systeem.

meest elementaire zijn Li en H punt defecten. **Hoofdstuk 2** van dit proefschrift bevat een *first-principles* studie van intrinsieke defecten en van *dopants* in $LiNH_2$. De Li-gerelateerde defecten Li_i^+ (Li kation op een interstitiële positie) en V_{Li}^- (een negatief geladen Li vacature) komen het meest voor en bepalen de ladingsbalans. Van de H-gerelateerde defecten komt V_H^- veel meer voor dan H_i^+. De vacature V_H^- is in wezen een NH^{2-} ion, geïncorporeerd in het amide rooster. De interstitieel H_i^+ en een $[NH_2]^-$ van het rooster vormen samen een NH_3 molecuul. *Dopants* als Ti and Sc hebben geen invloed op de concentratie van intrinsieke defecten, Mg and Ca kunnen deze concentratie een beetje beïnvloeden. Ti and Mg worden gemakkelijk in het $LiNH_2$ kristalrooster opgenomen, hetgeen de kristal morfologie op de nano-schaal kan veranderen.

Met een gravimetrische waterstofopslag capaciteit van 18.5 gewichtsprocent, is $LiBH_4$ een van de meeste interessante complexe hydrides. $LiBH_4$ is echter een relatief stabiel materiaal dat slechts bij hoge temperatuur ($\gtrsim$ 400 °C) uit elkaar valt. Bovendien is rehydrogenatie slechts mogelijk onder extreme omstandigheden. Typische waarden voor temperatuur en druk zijn 600 °C en 350 bar H_2. Daarenboven is de kinetiek van de waterstof opname en afgave langzaam. Dit is een algemeen probleem voor bulk complexe hydrides. Een recent voorgestelde aanpak van dergelijke problemen is door *nanoconfinement* in poreuze materialen (letterlijk vertaald: *confinement* = beperking. De deeltjes van het waterstofopslag materiaal worden dus in omvang beperkt tot een grootte van de orde van nano-meters). Voor $LiBH_4$ dat is geïnfiltreerd in koolstof *aerogels*, in nano-poreus koolstof, en in nano-poreus silica wordt een snellere dehydrogenatie kinetiek gerapporteerd, vergezeld van een reductie van de dehydrogenatie temperatuur met minstens 100 °C. Ook wordt door *confinement* een belangrijke verbetering van de reversibiliteit van de reactie gerealiseerd.

Deze feiten kunnen samenhangen met een verbeterde kinetiek: *confinement* houdt een beperking van de deeltjesgrootte in, hetgeen de afstand waarover deeltjes moeten diffunderen reduceert. Het is ook mogelijk dat de interactie met het *host* ("gastheer") materiaal de thermodynamica, d.i. de evenwichtscondities, van de reacties verandert. In **hoofdstuk 3** van dit proefschrift wordt de stabiliteit van $(LiBH_4)_n$ nano-clusters onderzocht, als functie van hun grootte. Ook wordt de stabiliteit bestudeerd van verscheidene clusters die na decompositie over kunnen blijven. Thermodynamisch zijn de reacties van vrije $LiBH_4$ nano-clusters met een diameter groter dan $\sim$ 2 nm niet te onderscheiden van de reacties voor bulk materiaal [d.i. eerst decompositie naar $Li_2B_{12}H_{12}$, gevolgd door een tweede decompositie stap resulterend in LiH en B]. Slechts clusters met een diameter kleiner dan $\sim$ 1 nm [$(LiBH_4)_n$, $n < 12$] hebben een merkbaar afwijkende thermodynamica. Deze is echter minder gunstig, m.a.w. het waterstof komt bij hogere temperaturen vrij dan in de bulk. Weliswaar zijn de $(LiBH_4)_n$ clusters minder stabiel dan bulk $LiBH_4$, maar dit geldt in nog meerdere mate voor de reactie producten.

Zoals reeds opgemerkt kan - naast effecten van de deeltjes grootte - de chemische interactie van reactanten/producten met het *host template* materiaal de thermodynamica van de waterstof (de)sorptie aanpassen. Inderdaad toont een recente *in situ* Röntgen Raman spectroscopie studie dat tijdens dehydrogenatie Li in het poreuze koolstof intercaleert. Dergelijke effecten worden in **hoofdstuk 4** bestudeerd. DFT berekeningen aan kleine $(LiBH_4)_n$ clusters ($n = 4$ en $n = 12$) op het oppervlak van een grafeen laag laten zien dat het effect van de interactie tussen de clusters en het koolstof substraat beperkt is. De intercalatie van Li (in grafiet) speelt een veel belangrijkere rol en heeft een groot potentieel om reacties met $(Li)_n$ clusters als eindproduct te stabiliseren. Wij vinden significant lagere decompositie temperaturen voor kleine $(LiBH_4)_n$ clusters ($n = 4$ en $n = 12$). Voor grotere clusters, waar dehydrognatie leidt tot de vorming van $(LiH)_n$ clusters, werkt dit mechanisme niet.

Voor een goed begrip van NMR spectra van nano-gestructureerde materialen is een accurate bepaling van de magnetische susceptibiliteit χ van belang, om oppervlaktestromen over het oppervlak van de nano-deeltjes goed te kunnen beschrijven. **Hoofdstuk 5** gaat over een alternatieve manier om χ vanuit *first-principles* te bepalen uit de berekende *chemical shift* tensoren van een model systeem bestaand uit een slab van kristallijn materiaal. Drie voorbeelden, welke een verscheidenheid aan materialen met verschillende chemische binding representeren, worden beschouwd: een echt model-systeem (rooster van inert gas atomen), een ionair en een covalent gebonden kristal. Voor Ne model systeem geeft de nieuwe methode aanzienlijke verbetering in vergelijk met de benaderde, bulk GIPAW (*Gauge-Including Projector-Augmented Wave*) lineaire respons uitdrukking voor χ. Alle methodes doen het voor $LiBH_4$ (ongeveer) even goed. Voor diamant wordt χ door de bulk GIPAW methode enigszins onderschat in vergelijk met de *all-electron* χ. De nieuwe slab-gebaseerde methode geeft, in combinatie met de *"converse"* methode[j] voor de berekening van *chemical shift* tensoren, opmerkelijke goede resultaten. In combinatie met de lineaire responsе GIPAW methode voor *chemical shifts* is er een zwakke afhankelijkheid van details van de oppervlakte terminatie.

---

[j] I.t.t. de "directe" methode van Mauri, Pfrommer and Louie, wordt in de "converse" methode van Thonhauser *et al.* de NMR chemical shift bepaald vanuit de magnetisatie die optreedt als reactie op een externe magnetische dipool $m^{ext}_{R\alpha}$ die op atoomkern **R** wordt geplaatst.

References

1. *Key World Energy Statistics* (International Energy Agency, 2012), 2012th ed.
2. *Fourth Assessment Report of the Intergovernmental Panel on Climate Change* (Cambridge University Press, 2007).
3. D. J. Hofmann, J. H. Butler, E. J. Dlugokencky, J. W. Elkings, K. Masarie, S. A. Montzka, and P. Tans, Tellus **58B**, 614 (2006).
4. P. P. Edwards, V. L. Kuznetsov, W. I. F. David, and N. P. Brandon, Energy Policy **36**, 4356 (2008).
5. L. Schlapbach and A. Züttel, Nature (London) **414**, 353 (2001).
6. S.-I. Orimo, Y. Nakamori, J. Eliseo, A. Züttel, and C. Jensen, Chem. Rev. **107**, 4111 (2007).
7. B. Sakintuna, F. Lamaridarkrim, and M. Hirscher, Int. J. Hydrogen Energy **32**, 1121 (2007).
8. W. Grochala and P. P. Edwards, ChemInform **35**, no (2004).
9. H. Imamura, K. Masanari, M. Kusuhara, H. Katsumoto, T. Sumi, and Y. Sakata, Journal of Alloys and Compounds **386**, 211 (2005).
10. A. Zaluska, L. Zaluski, and J. Strom-Olsen, Journal of Alloys and Compounds **288**, 217 (1999).
11. D. Lu, W. Li, S. Hu, F. Xiao, and R. Tang, International Journal of Hydrogen Energy **31**, 678 (2006).
12. Y. Chen, C. A. Sequeira, C. Chen, X. Wang, and Q. Wang, International Journal of Hydrogen Energy **28**, 329 (2003).
13. B. Bogdanović and M. Schwickardi, Journal of Alloys and Compounds **253**-**254**, 1 (1997).
14. P. Chen, Z. Xiong, J. Luo, J. Lin, and K. L. Tan, Nature **420**, 302 (2002).
15. P. Chen, Z. Xiong, J. Luo, J. Lin, and K. L. Tan, J. Phys. Chem. B **107**, 10967 (2003).
16. T. Ichikawa, S. Isobe, N. Hanada, and H. Fujii, J. Alloys Compd. **365**, 271 (2004).
17. W. Luo, J. Alloys Compd. **381**, 284 (2004).
18. J. H. Yao, C. Shang, K. F. Aguey-Zinsou, and Z. X. Guo, J. Alloys Compd.

432, 277 (2007).

19. S. Isobe, T. Ichikawa, K. Tokoyoda, N. Hanada, H. Leng, H. Fujii, and Y. Kojima, Thermochimica Acta **468**, 35 (2008).
20. A. Züttel, P. Wenger, S. Rentsch, P. Sudan, P. Mauron, and C. Emmenegger, J. Power Sources **118**, 1 (2003).
21. A. Züttel, A. Borgschulte, and S.-I. Orimo, Scr. Mater. **56**, 823 (2007).
22. L. George and S. Saxena, Int. J. Hydrogen Energy **35**, 5454 (2010).
23. I. Jain and P. Jain, J. Alloy. Compd. **503**, 303 (2010).
24. J. Yang and S. Hirano, Adv. Mater. **21**, 3023 (2009).
25. P. E. de Jongh and P. Adelhelm, ChemSusChem **3**, 1 (2010).
26. M. Au and R. T. Walters, Int. J. Hydrogen Energy **35**, 10311 (2010).
27. A. Gutowska, L. Li, Y. Shin, C. M. Wang, X. S. Li, J. C. Linehan, R. S. Smith, B. D. Kay, B. Schmid, W. Shaw,, Angew. Chem. Int. Ed. **44**, 3578 (2005).
28. P. E. de Jongh and P. Adelhelm, ChemSusChem **3**, 1332 (2010).
29. P. Adelhelm and P. E. de Jongh, J. Mater. Chem. **21**, 2417 (2011).
30. J. Gao, P. Adelhelm, M. H. W. Verkuijlen, C. Rongeat, M. Herrich, P. J. M. van Bentum, O. Gutfleisch, A. P. M. Kentgens, K. P. de Jong, and P. E. de Jongh, J. Phys. Chem. C **114**, 4675 (2010).
31. W. Lohstroh, A. Roth, H. Hahn, and M. Fichtner, ChemPhysChem **11**, 789 (2010).
32. T. Mueller and G. Ceder, ACS Nano **4**, 5647 (2010).
33. E. H. Majzoub, F. Zhou, and V. Ozoliņš, J. Phys. Chem. C **115**, 2636 (2011).
34. J. Vajo, T. Salguero, a. Gross, S. Skeith, and G. Olson, J. Alloy. Compd. **446-447**, 409 (2007).
35. A. F. Gross, J. J. Vajo, S. L. Van Atta, and G. L. Olson, J. Phys. Chem. C **112**, 5651 (2008).
36. Z. Fang, P. Wang, T. Rufford, X. Kang, G. Lu, and H. Cheng, Acta Mater. **56**, 6257 (2008).
37. S. Cahen, J.-B. Eymery, R. Janot, and J.-M. Tarascon, J. Power Sources **189**, 902 (2009).
38. P. Ngene, P. Adelhelm, A. M. Beale, K. P. de Jong, and P. E. de Jongh, J. Phys. Chem. C **114**, 6163 (2010).
39. P. Ngene, R. van Zwienen, and P. E. de Jongh, Chem. Comm. **46**, 8201 (2010).
40. D. T. Shane, R. L. Corey, C. McIntosh, L. H. Rayhel, R. C. Bowman, J. J. Vajo, A. F. Gross, and M. S. Conradi, J. Phys. Chem. C **114**, 4008 (2010).
41. X. Liu, D. Peaslee, C. Z. Jost, and E. H. Majzoub, J. Phys. Chem. C **114**, 14036 (2010).
42. X. Liu, D. Peaslee, C. Z. Jost, T. F. Baumann, and E. H. Majzoub, Chem.

Mater. **23**, 1331 (2011).

43. W. Sun, S. Li, J. Mao, Z. Guo, H. Liu, S. Dou, and X. Yu, Dalton Trans. **40**, 5673 (2011).
44. P. Ngene, M. H. W. Verkuijlen, Q. Zheng, J. Kragten, P. J. M. van Bentum, J. H. Bitter, and P. E. de Jongh, Faraday Discuss. **151**, 47 (2011).
45. P. Ngene, *Thesis: nanoconfined alkali-metal borohydrides for reversible hydrogen storage* (Utrecht University, Utrecht, 2012).
46. P. S. Miedema, P. Ngene, A. M. J. van der Eerden, T.-C. Weng, D. Nordlund, D. Sokaras, R. Alonso-Mori, A. Juhin, P. E. de Jongh, and F. M. F. de Groot, Phys. Chem. Chem. Phys. **14**, 5581 (2012).
47. T. Thonhauser, D. Ceresoli, A. a. Mostofi, N. Marzari, R. Resta, and D. Vanderbilt, The Journal of Chemical Physics **131**, 101101 (2009).
48. P. Hohenberg and W. Kohn, Phys. Rev. **136**, B864 (1964).
49. W. Kohn and L. J. Sham, Phys. Rev. **140**, A1133 (1965).
50. J. P. Perdew, K. Burke, and M. Ernzerhof, Phys. Rev. Lett. **77**, 3865 (1996).
51. P. Blöchl, Phys. Rev. B **44**, 13063 (1994).
52. G. Kresse and D. Joubert, Phys. Rev. B **59**, 1758 (1999).
53. G. Kresse and J. Furthmüller, Phys. Rev. B **54**, 11169 (1996).
54. G. Kresse and J. Furthmüller, Computational Materials Science **6**, 15 (1996).
55. R. O. Jones and O. Gunnarsson, Rev. Mod. Phys. **61**, 689 (1989).
56. C. Rostgaard, arXiv:0910.1921 [cond-mat.mtrl-sci] (2009).
57. M. Dion, H. Rydberg, E. Schröder, D. C. Langreth, and B. I. Lundqvist, Phys. Rev. Lett. **92**, 246401 (2004).
58. J. Klimeš, D. R. Bowler, and A. Michaelides, Phys. Rev. B **83**, 195131 (2011).
59. G. Román-Pérez and J. M. Soler, Phys. Rev. Lett. **103**, 096102 (2009).
60. F. Mauri, B. G. Pfrommer, and S. G. Louie, Phys. Rev. Lett. **77**, 5300 (1996).
61. T. Helgaker, M. Jaszuński, and K. Ruud, Chem. Rev. **99**, 293 (1999).
62. F. Mauri and S. G. Louie, Phys. Rev. Lett. **76**, 4246 (1996).
63. C. Pickard and F. Mauri, Phys. Rev. B **63**, 245101 (2001).
64. K. Ohno, F. Mauri, and S. G. Louie, Phys. Rev. B **56**, 1009 (1997).
65. D. Sebastiani and M. Parrinello, J. Phys. Chem. A **105**, 1951 (2001).
66. T. Gregor, F. Mauri, and R. Car, J. Chem. Phys. **111**, 1815 (1999).
67. J. R. Yates, C. J. Pickard, and F. Mauri, Phys. Rev. B **76**, 024401 (2007).
68. J. R. Yates, C. J. Pickard, M. C. Payne, and F. Mauri, The Journal of Chemical Physics **118**, 5746 (2003).
69. P. E. Blöchl, Phys. Rev. B **50**, 17953 (1994).
70. R. Laskowski and P. Blaha, Phys. Rev. B **85**, 035132 (2012).

71. T. Thonhauser, D. Ceresoli, A. Mostofi, N. Marzari, R. Resta, and D. Vanderbilt, J. Chem. Phys. **131**, 101101 (2009).
72. D. Ceresoli, T. Thonhauser, D. Vanderbilt, and R. Resta, Phys. Rev. B **74**, 024408 (2006).
73. R. D. King-Smith and D. Vanderbilt, Phys. Rev. B **47**, 1651 (1993).
74. D. Ceresoli, N. Marzari, M. Lopez, and T. Thonhauser, Phys. Rev. B **81**, 184424 (2010).
75. Y. H. Hu and E. Ruckenstein, J. Phys. Chem. A **107**, 9737 (2003).
76. T. Ichikawa, N. Hanada, S. Isobe, H. Leng, and H. Fujii, J. Phys. Chem. B **108**, 7887 (2004).
77. L. Shaw, W. Osborn, T. Markmaitree, and X. Wan, J. Power Sources **177**, 500 (2008).
78. S. Hino, T. Ichikawa, N. Ogita, M. Udagawa, and H. Fujii, Chem. Commun. pp. 3038–3040 (2005).
79. S. Isobe, T. Ichikawa, S. Hino, and H. Fujii, J. Phys. Chem. B **109**, 14855 (2005).
80. W. I. F. David, M. Jones, D. Gregory, C. Jewell, S. Johnson, A. Walton, and P. Edwards, J. Am. Chem. Soc. **129**, 1594 (2007).
81. K. F. Aguey-Zinsou, J. Yao, and Z. X. Guo, J. Phys. Chem. B **111**, 12531 (2007).
82. J.-C. Crivello, M. Gupta, R. Černý, M. Latroche, and D. Chandra, Phys. Rev. B **81**, 104113 (2010).
83. K. Ohoyama, Y. Nakamori, S. Orimo, and K. Yamada, J. Phys. Soc. Jpn. **74**, 483 (2005).
84. T. Noritake, H. Nozaki, M. Aoki, S. Towata, G. Kitahara, Y. Nakamori, and S. Orimo, J. Alloys. Comp. **393**, 264 (2005).
85. J. F. Herbst and L. G. Hector Jr., Phys. Rev. B **72**, 125120 (2005).
86. C. J. Zhang, M. Dyer, and A. Alavi, J. Phys. Chem. B **109**, 22089 (2005).
87. M. P. Balogh, C. Y. Jones, J. Herbst, L. G. Hector Jr., and M. Kundrat, J. Alloys Comp. **420**, 326 (2006).
88. B. Magyari-Köpe, V. Ozoliņš, and C. Wolverton, Phys. Rev. B **73**, 220101 (2006).
89. T. Mueller and G. Ceder, Phys. Rev. B **74**, 134104 (2006).
90. G. A. Ludueña, M. Wegner, L. Bjålie, and D. Sebastiani, ChemPhysChem. **11**, 2353 (2010).
91. M. Matsumoto, T. Haga, Y. Kawai, and Y. Kojima, J. Alloys Compd. **439**, 358 (2007).
92. Y. Nakamori and S. Orimo, J. Alloys Compd. **370**, 271 (2004).

93. S. Orimo, Y. Nakamori, G. Kitahara, K. Miwa, N. Ohba, T. Noritake, and S. Towata, Appl. Phys. A **79**, 1765 (2004).
94. C. Zhang and A. Alavi, J. Phys. Chem. B **110**, 7139 (2006).
95. H. M. Jin and P. Wu, Appl. Phys. Lett. **87**, 181917 (2005).
96. H. Zhang, K.-Z. Qi, G. Zhang, D. Wu, and S. Zhu, Acta Phys. Sin. **58**, 8077 (2009).
97. L. Li, B. Peng, Z. Tao, F. Cheng, and J. Chen, Adv. Funct. Mater. **20**, 1894 (2010).
98. J. Perdew, K. Burke, and M. Ernzerhof, Phys. Rev. Lett. **77**, 3865 (1996).
99. H. J. Monkhorst and J. D. Pack, Phys. Rev. B **13**, 5188 (1976).
100. G. Henkelman, B. P. Uberuaga, and H. Jónsson, J. Chem. Phys. **113**, 9901 (2000).
101. D. Sheppard, R. Terrell, and G. Henkelman, J. Chem. Phys. **128**, 134106 (2008).
102. J. B. Yang, X. D. Zhou, Q. Cai, W. J. James, and W. B. Yelon, Appl. Phys. Lett. **88**, 041914 (2006).
103. G. Kresse, J. Furthmüller, and J. Hafner, Europhys. Lett. **32**, 729 (1995).
104. C. G. Van de Walle and J. Neugebauer, J. Appl. Phys. **95**, 3851 (2004).
105. X. Ke and I. Tanaka, Phys. Rev. B **71**, 024117 (2005).
106. K. Miwa, N. Ohba, S. Towata, Y. Nakamori, and S. Orimo, Phys. Rev. B **71**, 195109 (2005).
107. T. Ichikawa, N. Hanada, S. Isobe, H. Leng, and H. Fujii, J. Alloys Compd. **404**, 435 (2005).
108. S. Isobe, T. Ichikawa, N. Hanada, H. Leng, M. Fichtner, O. Fuhr, and H. Fujii, J. Alloys Compd. **404**, 439 (2005).
109. S. Isobe, T. Ichikawa, Y. Kojima, and H. Fujii, J. Alloys Compd. **446**, 360 (2007).
110. T. Tsumuraya, T. Shishidou, and T. Oguchi, Phys. Rev. B **77**, 235114 (2008).
111. F. E. Pinkerton, J. Alloys Compd. **400**, 76 (2005).
112. L. Schlapbach and A. Züttel, Nature **414**, 353 (2001).
113. K. C. Kim, B. Dai, J. Karl Johnson, and D. S. Sholl, Nanotechnology **20**, 204001 (2009), ISSN 1361-6528.
114. R. W. P. Wagemans, J. H. van Lenthe, P. E. de Jongh, A. J. van Dillen, and K. P. de Jong, J. Am. Chem. Soc. **127**, 16675 (2005).
115. G. Wulff, Z. Kristallogr. **34**, 449 (1901).
116. S. Nosé, J. Chem. Phys. **81**, 511 (1984).
117. S. Nosé, Prog. Theor. Phys. Suppl. **103**, 1 (1991).
118. D. M. Bylander and L. Kleinman, Phys. Rev. B **46**, 13756 (1992).
119. G. Kresse, J. Furthmüller, and J. Hafner, Europhys. Lett. **32**, 729 (1995).

120. K. Momma and F. Izumi, J. Appl. Crystallogr. **44**, 1272 (2011).
121. Z. Łodziana and M. J. van Setten, Phys. Rev. B **81**, 024117 (2010).
122. M. J. van Setten, G. A. de Wijs, and G. Brocks, Phys. Rev. B **77**, 165115 (2008).
123. M. J. van Setten, G. A. de Wijs, M. Fichtner, and G. Brocks, Chem. Mater. **20**, 4952 (2008).
124. I. Boustani, Phys. Rev. B **55**, 16426 (1997).
125. K. C. Lau and R. Pandey, J. Phys. Chem C **111**, 2906 (2007).
126. H. Tang and S. Ismail-Beigi, Phys. Rev. Lett. **99**, 115501 (2007).
127. S. Er, G. A. de Wijs, and G. Brocks, J. Phys. Chem C **113**, 18962 (2009).
128. M. A. Fox and K. Wade, Pure Appl. Chem. **75**, 1315 (2003).
129. H. Perlitz and E. Aruja, Philosophical Magazine Serie **30**, 55 (1940).
130. E. Staritzky and D. I. Walker, Analytical Chemistry **28**, 1055 (1956).
131. Z. Liu, X. Qu, B. Huang, and Z. Li, Journal of Alloys and Compounds **311**, 256 (2000).
132. A. C. Switendick and B. Morosin, AIP Conf. Proc. **231**, 205 (1991).
133. J. Her, M. Yousufuddin, W. Zhou, S. S. Jalisatgi, J. G. Kulleck, J. A. Zan, S. Hwang, R. C. Bowman, Jr., and T. J. Udovic, Inorg. Chem. **47**, 9757 (2008).
134. J.-P. Soulie, G. Renaudin, R. Erny, and K. Yvon, J. Alloy. Compd. **346**, 200 (2002).
135. P. Vajeeston, P. Ravindran, and H. Fjellvåg, Nanotechnology **20**, 275704 (2009).
136. Q. Ge, J. Phys. Chem. A **108**, 8682 (2004).
137. P. W. Tasker, J. Phys. C: Solid State Phys. **12**, 4977 (1979).
138. M. J. van Setten, G. A. de Wijs, and G. Brocks, J. Phys. Chem. C **111**, 9592 (2007).
139. C. Herring, Phys. Rev. **82**, 282 (1951).
140. W. R. Tyson and R. A. Miller, Surf. Sci. **62**, 267 (2008).
141. M. Wörle and R. Nesper, Angew. Chem. Int. Ed. **39**, 2349 (2000).
142. S.-I. Orimo, Y. Nakamori, N. Ohba, K. Miwa, M. Aoki, S.-i. Towata, and A. Zuttel, Appl. Phys. Lett. **89**, 021920 (2006).
143. S.-J. Hwang, R. Bowman, J. Reiter, J. Rijssenbeek, G. Soloveichik, J.-C. Zhao, H. Kabbour, and C. Ahn, J. Phys. Chem. C **112**, 3164 (2008).
144. K. Miwa, N. Ohba, S.-I. Towata, Y. Nakamori, and S.-I. Orimo, Phys. Rev. B **69**, 245120 (2004).
145. D. J. Siegel, C. Wolverton, and V. Ozoliņš, Phys. Rev. B **76**, 134102 (2007).
146. V. Ozolins, E. H. Majzoub, and W. C., J. Am. Chem. Soc. **131**, 230 (2009).
147. O. Friedrichs, A. Remhof, S.-J. Hwang, and A. Züttel, Chem. Mater. **22**, 3265

(2010).

148. M. W. Chase, *NIST-JANAF Thermochemical Tables, 4th Edition* (American Institute of Physics, 1998).
149. T. Vegge, Phys. Chem. Chem. Phys. **8**, 4853 (2006), ISSN 1463-9076.
150. W. Hayami and S. Otani, J. Phys. Chem. C **111**, 10394 (2007).
151. A. N. Kolmogorov and S. Curtarolo, Phys. Rev. B **74**, 224507 (2006).
152. J. J. Vajo, Current Opinion in Solid State and Materials Science **15**, 52 (2011).
153. S. Er, G. A. de Wijs, and G. Brocks, J. Phys. Chem. C **113**, 8997 (2009).
154. D. Çakır, G. A. de Wijs, and G. Brocks, J. Phys. Chem. C **115**, 24429 (2011).
155. M. J. v. Setten, G. A. d. Wijs, M. Fichtner, and G. Brocks, Chemistry of Materials **20**, 4952 (2008).
156. E. Hazrati, G. Brocks, B. Buurman, R. A. de Groot, and G. A. de Wijs, Phys. Chem. Chem. Phys. **13**, 6043 (2011).
157. E. Hazrati, G. Brocks, and G. A. de Wijs, J. Phys. Chem. C **116**, 18038 (2012).
158. P. Adelhelm, K. P. de Jong, and P. E. de Jongh, Chem. Commun. pp. 6261–6263 (2009).
159. L. Joncourt, M. Mermoux, P. Touzain, L. Bonnetain, D. Dumas, and B. Allard, J. Phys. Chem. Solids **57**, 877 (1996).
160. J. R. Dahn, T. Zheng, Y. Liu, and J. S. Xue, Science **270**, 590 (1995).
161. M. Winter, J. O. Besenhard, M. E. Spahr, and P. Novák, Adv. Mater. **10**, 725 (1998).
162. S. Er, G. A. de Wijs, and G. Brocks, The Journal of Physical Chemistry C **113**, 8997 (2009).
163. Y. Zhang and W. Yang, Phys. Rev. Lett. **80**, 890 (1998).
164. K. Lee, E. D. Murray, L. Kong, B. I. Lundqvist, and D. C. Langreth, Phys. Rev. B **82**, 081101 (2010).
165. J. P. Perdew and W. Yue, Phys. Rev. B **33**, 8800 (1986).
166. J. Klimeš, D. R. Bowler, and A. Michaelides, J. Phys.: Condens. Matter **22**, 022201 (2010).
167. M. Methfessel and A. T. Paxton, Phys. Rev. B **40**, 3616 (1989).
168. L. Spanu, S. Sorella, and G. Galli, Phys. Rev. Lett. **103**, 196401 (2009).
169. Y. Baskin and L. Meyer, Phys. Rev. **100**, 544 (1955).
170. R. Zacharia, H. Ulbricht, and T. Hertel, Phys. Rev. B **69**, 155406 (2004).
171. I. Hamada and M. Otani, Phys. Rev. B **82**, 153412 (2010).
172. R. Mapasha, a. Ukpong, and N. Chetty, Phys. Rev. B **85**, 205402 (2012).
173. J. D. Bernal, Proc. R. Soc. Lond. A **106**, 749 (1924).
174. J.-C. Charlier, X. Gonze, and J.-P. Michenaud, Europhys. Lett. **28**, 403 (1994).

175. K. T. Chan, J. B. Neaton, and M. L. Cohen, Phys. Rev. B **77**, 235430 (2008).
176. A. M. Garay-Tapia, A. H. Romero, and V. Barone, J. Chem. Theory Comput. **8**, 1064 (2012).
177. F. Valencia, A. H. Romero, F. Ancilotto, and P. L. Silvestrelli, J. Phys. Chem. B **110**, 14832 (2006).
178. S. Er, G. A. de Wijs, and G. Brocks, The Journal of Physical Chemistry C **113**, 18962 (2009).
179. R. B. Pontes, A. Fazzio, and G. M. Dalpian, Phys. Rev. B **79**, 033412 (2009).
180. J. R. Dahn, Phys. Rev. B **44**, 9170 (1991).
181. K. C. Woo, W. A. Kamitakahara, D. P. DiVincenzo, D. S. Robinson, H. Mertwoy, J. W. Milliken, and J. E. Fischer, Phys. Rev. Lett. **50**, 182 (1983).
182. S. A. Safran and D. R. Hamann, Phys. Rev. B **22**, 606 (1980).
183. N. Takami, A. Satoh, M. Hara, and T. Ohsaki, J. Electrochem. Soc. **142**, 371 (1995).
184. D. Billaud, F. Henry, M. Lelaurain, and P. Willmann, J. Phys. Chem Solids **57**, 775 (1996).
185. K. Persson, Y. Hinuma, Y. S. Meng, A. Van der Ven, and G. Ceder, Phys. Rev. B **82**, 125416 (2010).
186. V. V. Avdeev, A. P. Savchenkova, L. A. Monyakina, I. V. Nikolskaya, and A. V. Khvostov, J. Phys. Chem Solids **57**, 947 (1996).
187. The experimental enthalpy of fusion for Li at its melting point (453.7 K) is 3 kJ/mol.
188. P. A. Berseth, A. G. Harter, R. Zidan, A. Blomqvist, C. M. Araujo, R. H. Scheicher, R. Ahuja, and P. Jena, Nano Lett. **9**, 1501 (2009).
189. R. H. Scheicher, S. Li, C. M. Araujo, A. Blomqvist, R. Ahuja, and P. Jena, Nanotechnology **22**, 335401 (2011).
190. P. Ngene, M. H. W. Verkuijlen, Q. Zheng, J. Kragten, P. J. M. van Bentum, J. H. Bitter, and P. E. de Jongh, Faraday Discuss. **151**, 47 (2011).
191. D. L. Landau and E. M. Lifshitz, *Electrodynamics of Continuous Media* (Wiley, New York, 1960).
192. J. D. Jackson, *Classical Electrodynamics, 2nd edition* (Wiley, New York, 1975).
193. D. M. Ceperley and B. J. Alder, Phys. Rev. Lett. **45**, 566 (1980).
194. J. P. Perdew and A. Zunger, Phys. Rev. B **23**, 5048 (1981).

Acknowledgments

I would like to thank Prof. Robert de Groot, my supervisor, for his guidance during my PhD. My special thanks go to Dr. Gilles de Wijs, my daily supervisor, for teaching me about VASP, having time for lots of discussions and giving me practical advices. A special thanks goes to Dr. Geert Brocks from university of Twente, my second copromotor. He has been a critical reader of all of the work in this thesis. His comments were always very helpful.

I would like to thank the past and present members of the Electronic Structure of Materials group in Nijmegen: Igor Shokaryev, Karol Jarolimek, Baomin Zhang, Engin Torun, Filipe Vasconcelos, Pegah Zolfaghari, and Prasenjit Roy for helpfull scientific disscusions and a lot of fun that we had together. I also would like to thank Mikhail Akhukov, from TCM group, for sharing his programing knowledge with me.

I also would like to thank the members of the UniVV3 soccer team: Arie, Totti, Paco, Berg, Gerie, Rob, Amin, Jonas, Hermsen, Philip, Wessel, Gerbe, Andres, Sam, Alex, Ralf, Huib, Sebastiaan, Minko, Denys, Marcel, Harry, Gio, Sjoerd, Jorick, Cees, Emiel, Jan, Brian. It was a lot of fun playing football with you guys on Tuesdays and Saturadays.

Last but not least my greatest thanks go to my beloved ones: my parents, and my wife Pegah.

Curriculum Vitae

Ebrahim Hazrati

Born on August 23^{rd}, 1983

in Gandoman, Iran

2008-2012 Junior Researcher (Ph.D. student) Electronic Structure of Materials
IMM, Radboud University Nijmegen, The Netherlands
Project: Complex Hydrides for Hydrogen Storage: A First-Principles Study

2005-2008 Master of Science (M.Sc.) in Physics
Isfahan University of Technology, Isfahan, Iran
Project: First principles study of bulk CrSe and CrSe/ZnSe (001) interface
Supervisors: Dr. S.J. Hashemifar and Prof. Dr. H. Akbarzadeh

2000-2004 Bachelor of Science (B.Sc.) in Physics
Isfahan University of Technology, Isfahan, Iran
Project: First-principles study of CrO_2
Supervisor: Prof. Dr. H. Akbarzadeh

List of publications

- **E. Hazrati**, G. Brocks, B. Buurman, R. A. de Groot and G. A. de Wijs; "*Intrinsic defects and dopants in $LiNH_2$: A first-principles study*", Phys. Chem. Chem. Phys., 2011, **13**, 6043-6052
- **E. Hazrati**, G. Brocks, and G. A. de Wijs; "*First-principles study of $LiBH_4$ nanoclusters and their hydrogen storage properties*", J. Phys. Chem. C 2012, **116**, 18038-18047
- **E. Hazrati**, G. Brocks, and G. A. de Wijs; "*Li adsorption on graphene and graphite surfaces and intercalation in graphite: A van der Waals density functional study*", submitted to Phys. Rev. B
- **E. Hazrati**, G. Brocks, and G. A. de Wijs; "*Carbon support effects on confined $LiBH_4$ nanoparticles: A first-principles study*", submitted to J. Phys. Chem. C.
- **E. Hazrati**, Filipe Vasconcelos, Georg Kresse, Martijn Marsman, and G. A. de Wijs; "*Orbital magnetic susceptibility from chemical shielding calculations*", in preparation
- E.H. Majzoub
  Center for Nanoscience and Department of Physics and Astronomy, University of Missouri-St. Louis, St. Louis, Missouri 63121, United States
  E. Hazrati and Gilles A. de Wijs;
  "*First-principles study of structural prototypes for NaAlH4: Elevated pressure polymorph in symmetry Fmm2 leads to a single-step decomposition pathway*", accepted in J. Phys. Chem. C 2013, **DOI**: 10.1021/jp401325y.

Other publications:

- **E. Hazrati**[†], S.J. Hashemifar[†], and H. Akbarzadeh[†]; "*First principles study of bulk CrSe and CrSe/ZnSe (001) interface*", J. Appl. Phys. 104, 113719 (2008)

[†] Department of Physics, Isfahan University of Technology, 84156-83111 Isfahan, Iran